

Light intensity dependence of the open-circuit voltage in organic bulk heterojunction solar cells

Gerrit Jan Jacob Lof

Dr. L. J. A. Koster



University of Groningen
**Zernike Institute
for Advanced Materials**

Photophysics and OptoElectronics
Zernike Institute for Advanced Materials
University of Groningen
January 2014

Abstract

To improve the efficiency of organic bulk heterojunction (BHJ) solar cells, accurate determination and understanding of all loss mechanisms is essential. By studying the light intensity dependence of the open-circuit voltage (V_{OC}), this research shows that in current organic BHJ solar cells the open-circuit voltage is strongly affected by losses. In literature it is usually assumed that the V_{OC} depends linearly on the natural logarithm of intensity, with the slope in units of the thermal voltage often denoted as S . By contrast, this research shows that this dependence is non-linear. More specific, S decreases for increasing intensity. Several methods have been used to confirm this finding. While usually values between 1 and 2 are reported for the S -value of organic solar cells, it has been determined that the value of S might become much smaller than unity for relatively large intensities. Moreover, this effect has been demonstrated for silicon solar cells as well. The origin of this finding is the improvement of accuracy with respect to conventional methods, by using a monochromatic laser instead of a spectrally broad lamp. Particularly accurate results have been obtained with the newly introduced steady-state differential voltage (SSDV) technique. This technique is based on measuring under open-circuit conditions the differential open-circuit voltage ΔV_{OC} induced by a laser beam with intensity ΔI superimposed on a laser beam with intensity I . The voltage ΔV_{OC} is picked up from a lock-in amplifier which is used in conjunction with a chopper.

Acknowledgements

First of all I would like to thank Jan Anton Koster for giving me the opportunity to do research under his commendable supervision. I admire your competence to perform both excellent experimental and theoretical research, and I enjoyed to learn from you. In particular, I would also like to express my appreciation to Jan Harkema for the provision in the lab. Furthermore, the assistance from Paul de Bruijn, Gert-Jan Wetzelaer, Martijn Kuik, Niels van der Kaap, Mark Speirs and Tondo van Rest has been particularly valuable as well. A special thanks to Martijn again and to Johan Trinks, for fabricating the T1 and MEH solar cells respectively, and for measuring the V_{oc} as a function of intensity with the Solar Simulator (Figure 41). Thanks to all other group members as well, for the great and instructive time in the group.

Contents

1	Introduction	7
2	Theory	10
2.1	The p - n junction solar cell.....	10
2.2	Organic bulk heterojunction solar cells.....	10
2.3	Performance characteristics.....	13
2.4	The p - n junction based model.....	14
2.5	The MIM model	15
2.6	The Shockley-Queisser limit	16
2.7	Other loss mechanisms in organic BHJ solar cells.....	17
2.7.1	Langevin recombination	17
2.7.2	Shockley-Read-Hall recombination.....	18
2.8	Koster's equation for the open-circuit voltage.....	18
3	Measuring methods.....	20
3.1	Intensity dependence of the open-circuit voltage.....	21
3.2	Methods for determination of S	22
3.2.1	Method I: S from linear fitting.....	22
3.2.2	Method II: S from differentiation.....	23
3.2.3	Determining S from the slope between $V_{oc}(I)$ and $V_{oc}(I+\Delta I)$	23
3.2.4	Method III: Selection via $1 < \Delta I/I < 2$	24
3.2.5	Method IV: Polynomial fits.....	24
3.2.6	Method V: Using a beam splitter.....	24
3.2.7	Method VI: The SSDV technique	25
3.3	Influence of leakage current.....	25
3.4	The p - n junction based model applied to BHJ solar cells	28
3.4.1	Modelling i - V curves	28
3.4.2	Modelling the intensity dependence of V_{oc}	31
3.4.3	Variation of R_{SH}	32
4	Device fabrication and characterization.....	34
4.1	Fabrication	34

4.1.1	P3HT	35
4.1.2	MEH	36
4.1.3	T1	36
4.2	Thicknesses.....	37
4.3	Characterization	37
5	Experiments.....	39
5.1	V_{OC} as a function of laser light intensity	39
5.2	Determination of S	41
5.2.1	Method I: S from linear fitting.....	41
5.2.2	Method II: S from differentiation.....	43
5.2.3	Method III: Selection via $\Delta I/I > 1$	44
5.2.4	Method IV: Polynomial fits.....	45
5.2.5	Method V: Using a beam splitter	46
5.3	The steady-state differential voltage technique	47
5.3.1	Experimental setup	47
5.3.2	SSDV measurement results	48
5.4	The modified p - n junction based model	49
5.4.1	Reproducing the experimental results	49
5.4.2	A criterion test for open circuit conditions	51
5.5	Measurement of V_{OC} with Solar Simulator	53
5.6	Silicon photodiode	54
5.6.1	Intensity dependence of V_{OC}	54
5.6.2	Dependence on beam overlap	55
5.7	Error analysis	57
6	Discussion	59
6.1	Comparison of methods to determine S	59
6.2	Influence of partial illumination	61
6.3	Suggestions for future research.....	61
6.3.1	Origin of $S < 1$	61
6.3.2	Alternative measuring methods.....	62

7	Conclusion	64
8	Appendices.....	66
8.1	External quantum efficiency.....	66
8.2	Intensity dependence of the short-circuit current.....	68
8.2.1	Introduction	68
8.2.2	Measuring J_{SC} as a function of intensity	68
8.2.3	Steady-state differential current technique	69
8.3	Manual for the Steady-State Differential Voltage (SSDV) technique.....	71
8.4	Variation of ratio $\Delta I/I$	72
8.5	Extent of overlap of laser beams behind the aperture.....	73
8.6	Temperature measurements	76
8.7	The $p-n$ junction based model in Matlab	76
8.7.1	Modified $p-n$ junction based model	76
8.7.2	The model as a criterion test for open circuit conditions.....	77
	References	81

1 Introduction

Due to the burning of carbon based fossil fuels on massive scale, mankind has caused the concentration of the greenhouse gas carbon dioxide in the Earth's atmosphere to rise tremendously. Although the greenhouse effect is of fundamental importance for life on Earth, disturbance of the environmental balance will induce long-term detrimental effects. The increase of greenhouse gases in the atmosphere causes the global mean surface temperature to increase which might induce chain reactions of severe consequences.^[1] The melting of the Earth's ice will not only induce the global water level to rise but also enhance the amount of absorbed sunlight due to the lower reflectivity of water compared to ice. Another predicted positive feedback mechanism is the release of methane – a much stronger greenhouse gas than carbon dioxide – due to the melting of the Arctic permafrost. The concentrations of carbon dioxide is found to increase in oceans as well causing acidification which poses a threat to the food chains connected with the oceans. Consequences of global warming are also believed to be experienced in the form of increased frequency and severity of natural disasters like hurricanes and droughts.^[2] The increase of population and welfare will cause the global energy demand to continue to grow.^[3] Although fossil fuels are becoming scarcer, it will take much more than a century to run out of these supplies. Hence, probably only economic benefits might be able to force mankind to prefer renewable energy sources. Renewable energy should thus be economically competitive with conventional energy.

Harvesting energy from sunlight using photovoltaic (PV) technology is being widely recognized as an essential component of future global energy production. The Earth is abundantly illuminated with an amount of energy that is almost ten thousand times as much as the global energy consumption.^{[4],[5]} Nowadays, the PV market is dominated by solar cells made of highly purified silicon crystal. The power conversion efficiency (*PCE*) reached for monocrystalline silicon wafers amounts 25% under standard testing conditions.^[6] The first generation of commercial solar cells exhibits *PCEs* of 16-18%. Disadvantages of monocrystalline silicon wafers are the large amount of energy required for production and the complexity, resulting in a long payback time, both economically and energetically. Alternatives such as polycrystalline and amorph silicon are cheaper to produce, but have significantly lower efficiencies.

Organic, or plastic solar cells bear the potential to develop a long-term technology being economically viable for large-scale power generation based on environmentally friendly materials with unlimited availability. The research of organic PV uses polymers, oligomers or small molecules as organic materials. Organic materials can have extremely high optical absorption coefficients which allows organic solar cells to be very thin, which is advantageous when considering production costs and makes them lightweight. Their flexibility allows them to be used even in areas where the more rigid and fragile silicon based PV cells are inconvenient. Because organic solar cells are generally soluble in organic solvents, they can be fabricated using high-throughput and low temperature approaches that employ well established printing techniques

in a roll-to-roll process.^{[7],[8]} This possibility of using flexible plastic substrates in an easily scalable high-speed printing process can reduce the production costs of organic PVs, resulting in a shorter energetic payback time.

Notwithstanding these advantages, organic PV has to overcome several technological and scientific challenges. Quite promising is the fact that several organic solar cells have been produced with *PCEs* exceeding 10%. However, these are lab scale devices with a typical area size of 1 cm². To reproduce such large efficiencies for large areas on massive scale with a roll-to-roll process is one of the main challenges of organic PV. Also important is to improve the stability to reach lifetimes in the order of twenty years which is a challenge because organic materials usually easily react with water and oxygen. To further increase the *PCEs* a thorough fundamental understanding is required of the physical processes in organic solar cells. One of the main loss mechanisms in the power conversion process in current organic solar cells is the recombination of photogenerated charges. Accurate experimental techniques are needed to study such fundamental processes.

This thesis reports an experimental research project which studies the light intensity dependence of the open-circuit voltage (V_{OC}) in organic solar cells. Chapter 2 describes the principles of solar cells together with the relevant theory. Chapter 3 introduces six measuring methods to study the light intensity dependence of the V_{OC} . Also a modified *p-n* junction model is introduced as a guide to interpret the measurements. Chapter 4 describes five organic bulk heterojunction (BHJ) solar cells on which measurements will be performed together with their performance characteristics. Chapter 5 describes the measurement setups and results. The intensity dependence of the V_{OC} of silicon solar cells is investigated as well. Chapter 6 critically assesses the measurement results and gives suggestions for future results. Chapter 7 gives the conclusions of this research. Finally, Chapter 8 consists of appendices. The script of the model is supplied at the end.

In literature it is usually assumed that the V_{OC} depends linearly on the logarithm of intensity. Conventional methods usually use a spectrally broad lamp. Instead, in this research a laser is used which will provide much more accurate results due to its monochromaticity. From these results it has been discovered that the dependence is non-linear. Several methods will be used to confirm this finding. A new measuring method is introduced, i.e. the steady-state differential voltage (SSDV) technique. This measuring technique is in many ways analogous to the SSDC technique which aims to study the light intensity dependence of the short-circuit current.^[9]

In research on organic solar cells, often P3HT:PCBM solar cells are used as a work horse. This type of solar cell usually produces a V_{OC} of about 0.6 V. The band gap of P3HT amounts about 1.9 eV, which could within the Shockley-Queisser limit contribute to a V_{OC} of 1.9 V.^[10] Obviously, the loss mechanisms in organic solar cells are responsible for a massive reduction of the efficiency. Therefore, investigating mechanisms that affect the V_{OC} , seems to be a promising route towards improving the efficiency of organic BHJ solar cells.

Chapter 1. Introduction

The organic BHJ solar cells used throughout this thesis are tabulated in Table 1. Although it is not clear from the abbreviation, one should keep in mind that all solar cells consist of PCBM as well.

Table 1: Abbreviations and structures of the organic BHJ solar cells used in this thesis. The last column refers to the chapters where the solar cells are introduced.

Abbreviation	Solar cell structure	Chapter
P3HT-L Ω	ITO / low ohmic PEDOT:PSS / P3HT:[60]PCBM / LiF / Al	2.3
P3HT	ITO / high ohmic PEDOT:PSS / P3HT:[60]PCBM / LiF / Al	4.1.1
MEH	ITO / high ohmic PEDOT:PSS / MEH:[60]PCBM / LiF / Al	4.1.2
T1H Ω	ITO / high ohmic PEDOT:PSS / T1:[70]PCBM / Ca / Al	4.1.3
T1L Ω	ITO / low ohmic PEDOT:PSS / T1:[70]PCBM / Ca / Al	4.1.3
T1SL Ω	ITO / super low ohmic PEDOT:PSS / T1:[70]PCBM / Ca / Al	4.1.3

2 Theory

2.1 The p - n junction solar cell

Inorganic solar cells usually consist of a semiconductor that is doped to form a p - n junction. The n -type semiconductor consists of an excess of negative charges (electrons), and the p -type consists of an excess of positive charge carriers (holes). Due to the diffusion of charge carriers a so-called depletion region is created close to the junction, which induces a built-in electric field. Eventually, enough charges will flow across the boundary to equalize the Fermi levels of the two materials, giving a state of thermal equilibrium. In an energy band diagram this process corresponds to a bending of the energy levels close to the junction, as illustrated in Figure 1. When the solar cell is illuminated with light, electrons from the valence band are excited to the conduction band by a process known as photoexcitation, where they are free to move through the material. For a photon to be absorbed, it should have an energy larger than the band gap E_g of the material. These charges are collected at the electrodes which are externally connected allowing a current to flow.

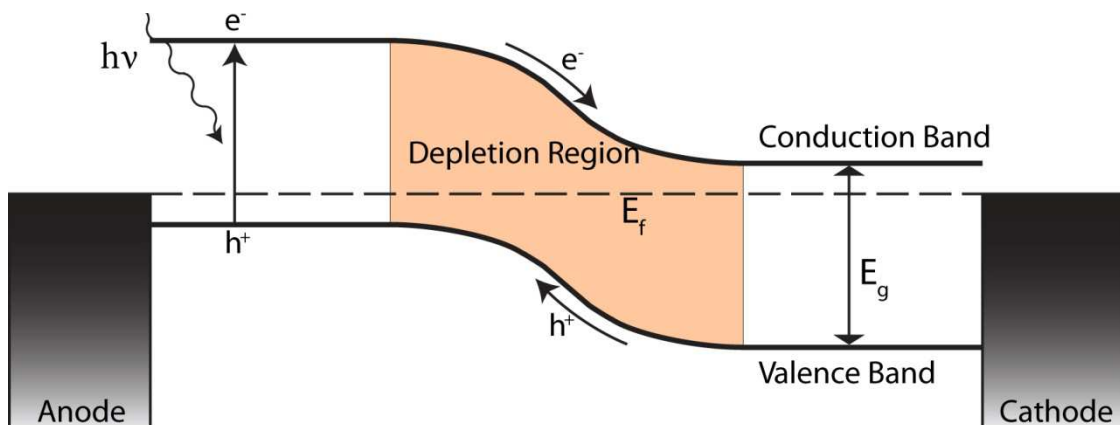


Figure 1: Energy band diagram of an inorganic p - n junction solar cell. Thermal equilibrium conditions are satisfied by the alignment of the Fermi levels.

2.2 Organic bulk heterojunction solar cells

An organic heterojunction solar cell consists of a photoactive layer sandwiched between two electrodes with asymmetric work functions, where the photoactive layer consists of two different organic materials, a donor (D) and an acceptor (A). The semiconducting property of these materials originates from conjugated π -electrons. A π -conjugated system consists of an alternation of single and double carbon bonds. Single bonds are also known as σ -bonds, which contain localized electrons. Double bonds consist of both a σ -bond and a π -bond. A π -bond originates from the overlap of neighboring p_z -orbitals, being present due to sp^2 -hybridization. The wave functions of the π -electrons become delocalized over the molecule due to the mutual overlap of π -bonds, allowing the π -electrons to move through the molecule. The filled π -band is called the Highest Occupied Molecular Orbital (HOMO), analogous to the valence band of inorganic semiconductors. The empty π^* -band is called the Lowest Unoccupied Molecular

Orbital (LUMO), analogous to the conduction band. The energetic difference between the HOMO and the LUMO is the band gap of the organic material.

Although charge can be moved via the π -orbitals, the charge mobility is typically several orders of magnitude lower than for inorganic semiconductors. Organic materials generally absorb light very well, due to high absorption coefficients. This allows the photoactive layer to be very thin – in the order of 100 nm – which partly compensates for the low charge mobility since charges do not have to travel very far. However, absorption of light in organic materials does not result in free charge carriers but in a tightly bound electron-hole pair, called a Frenkel exciton. This occurs because organic materials generally have very low dielectric constants, which induces the Coulomb forces to extend over a greater volume than in inorganic materials. Also, the non-covalent electron interactions between organic molecules are relatively weak, causing the wave functions of the electron to be localized in the potential well of the corresponding hole.^[11] The exciton should first be dissociated into free charges before charge extraction can take place.

The idea behind the D/A heterojunction is to use two materials with different electron affinities and ionization potentials. If the difference in potential energy is larger than the exciton binding energy, exciton dissociation is possible. The electron is then accepted by the material with the larger electron affinity, and the hole by the material with the lower ionization potential. In a planar heterojunction, or bilayer device, the donor and acceptor materials are two separated layers. Figure 2(a) shows a light photon being absorbed by the donor phase (1). Because the created exciton is electrically neutral, it has to diffuse to the D/A interface (3). After exciton dissociation (4) the metastable electron-hole pair might still be Coulombically bound. Further charge separation (5) is promoted by means of the internal electric field, caused by the use of electrodes with asymmetric work functions. The charges are collected by the electrodes (6) and driven into the external circuit, generating a photocurrent.

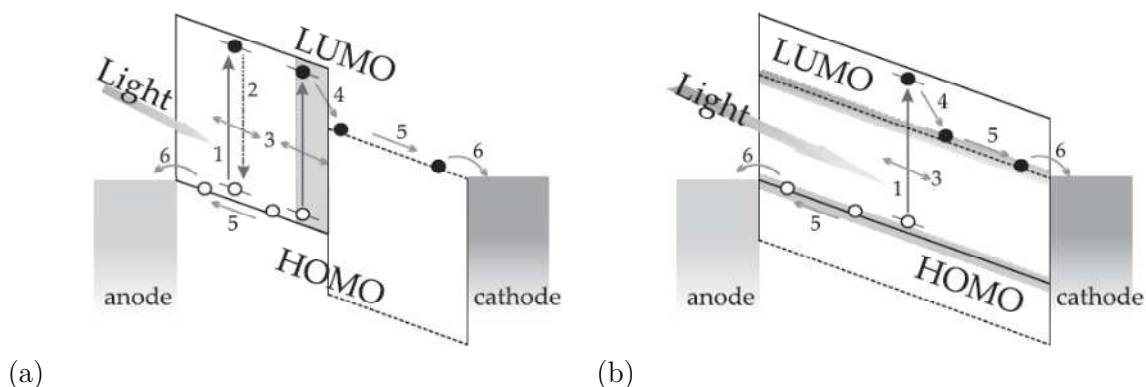


Figure 2: Energy band diagram of a bilayer (a) and a bulk heterojunction solar cell (b) in which the processes of exciton generation (1), recombination (2), exciton diffusion (3), dissociation (4), charge separation (5), and collection at the electrodes (6) are shown.

The exciton diffusion length in organic materials is much smaller than the absorption depth. In a bilayer device, many excitons are therefore created too far from the D/A interface and will recombine (2). A revolution in the development of organic solar cells arose with the introduction of the bulk heterojunction (BHJ), where the donor and acceptor materials are blended together. In a BHJ the probability is much larger that excitons are formed at a distance from a D/A interface smaller than the exciton diffusion length. Charge generation can thus take place everywhere in the photoactive layer.

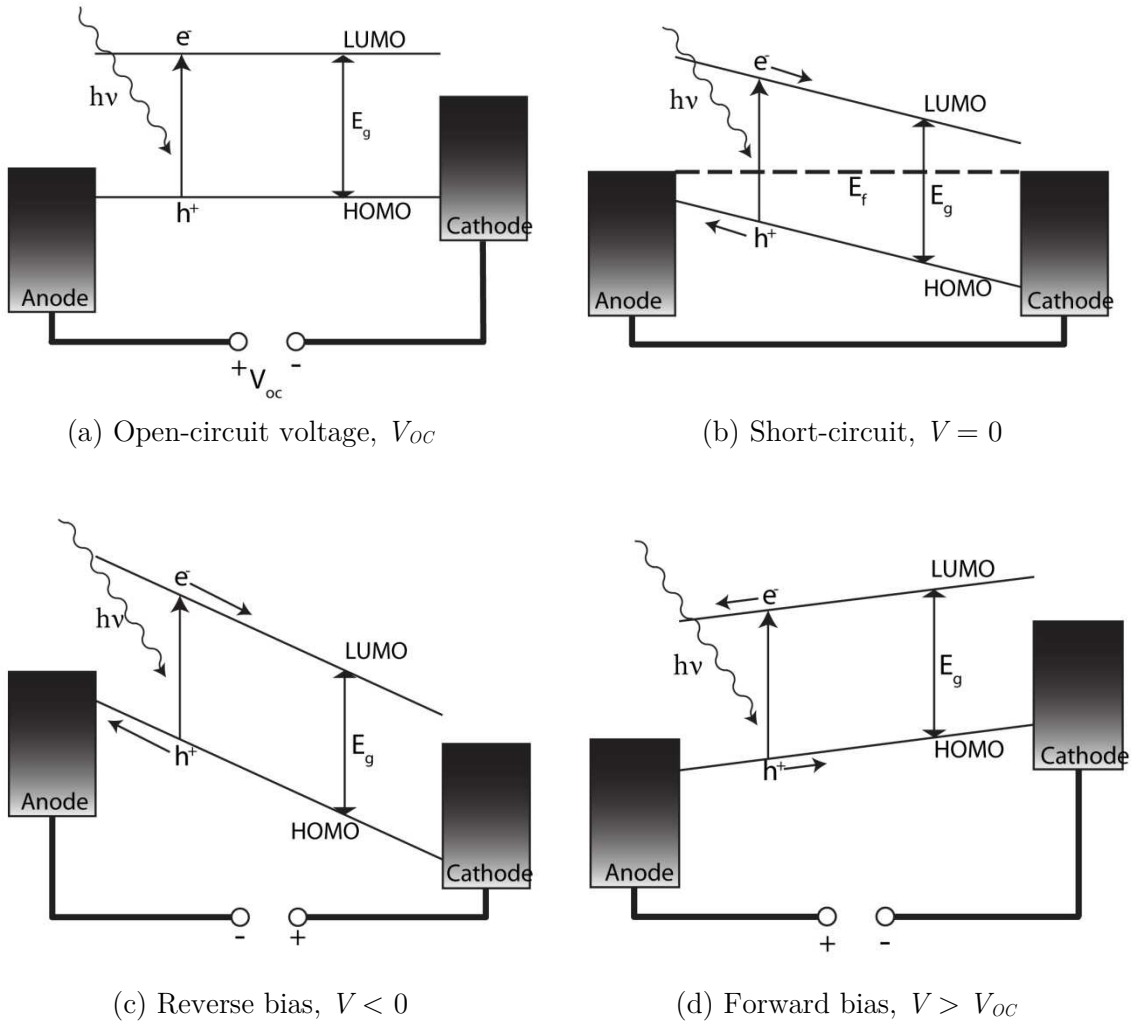


Figure 3: Energy band diagrams of an organic solar cell under various bias conditions.

The behavior of organic solar cells under illumination for various biasing conditions is illustrated in Figure 3. Under open-circuit conditions no current flows because all generated charges recombine. This corresponds to horizontal bands as illustrated in Figure 3(a). The voltage generated under illumination in these conditions is the open-circuit voltage V_{OC} . When the device is loaded via an external circuit, a current starts to flow which reduces the voltage. If the voltage is zero, the solar cell is under short-circuit conditions, which is depicted in Figure 3(b). No external voltage is created because the Fermi levels of the electrodes align. Because of the original difference between the work functions of the electrodes, the alignment induces an electric

field in the insulator. This electric field causes free holes in the HOMO to drift towards the anode, and the free electrons in the LUMO towards the cathode. In the region between the short-circuit current and the open-circuit voltage, i.e. $0 < V < V_{oc}$, the solar cell delivers power. In Figure 3(c) the reverse bias situation is illustrated where the solar cell effectively functions as a photodetector. All free charges flow towards the electrodes due to the strong electric field. Figure 3(d) shows the situation of forward bias where charges are injected from the electrodes because the barrier for electrons from the cathode to the LUMO – and for holes from the anode to the HOMO – is fairly low. If the photoactive layer contains a luminescent material, these charges might recombine under emission of light. The solar cell then functions as a light emitting diode (LED).

2.3 Performance characteristics

The main characterization of solar cells is carried out by current-voltage measurements, both under illumination and in the dark. As the light source a Steuernagel SolarConstant 1200 metal halide lamp is used, referred to as the Solar Simulator. A typical current-voltage characteristic is represented by Figure 4, which was obtained for a P3HT:PCBM solar cell with low ohmic PEDOT:PSS used as the hole transport layer. This type of solar cell is a typical work horse in the research of organic BHJ solar cells. Throughout this thesis this solar cell, which is being referred to as the P3HT-L Ω solar cell, will be used for some experiments in Chapter 2.4 and Chapter 3 to support the theory, and as an input for the model in Chapter 3.4 and Chapter 5.4.2. This solar cell should not be confused with the P3HT solar cell of Chapter 4 and 5, which instead consists of high ohmic PEDOT:PSS.

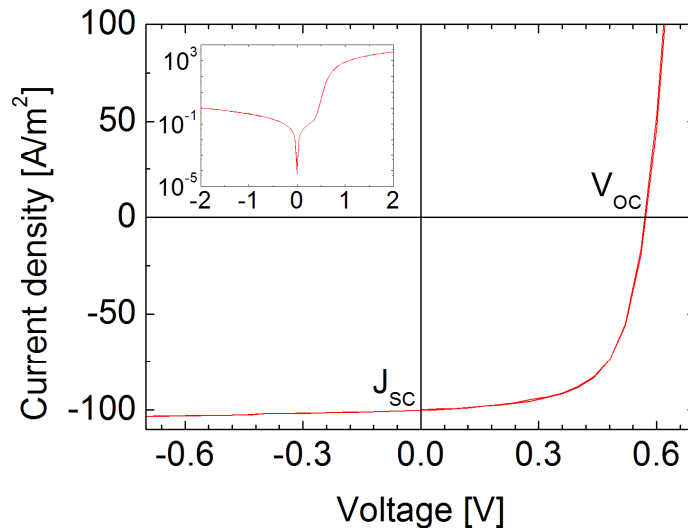


Figure 4: J - V characteristics for a P3HT:PCBM (low ohmic PEDOT:PSS) solar cell under illumination. The inset shows the characteristics in the dark.

A positive applied voltage (V_a) corresponds to positive biasing of the anode. Current density is defined as the current per unit illuminated area of the solar cell, with J_D and J_L the current density in the dark and under illumination respectively. The intersections of the axes correspond to the short-circuit current density

$$J_{SC} = |J_L(V_a = 0)|, \quad (2.1)$$

and the open-circuit voltage

$$V_{OC} = V_a(J_L = 0). \quad (2.2)$$

The fill factor is defined as

$$FF = \frac{|J_L V_a|_{\max}}{J_{SC} V_{OC}}. \quad (2.3)$$

From these quantities, the power conversion efficiency (*PCE*) is obtained according to

$$PCE = \frac{J_{SC} V_{OC} FF}{I}, \quad (2.4)$$

with I the incident light intensity in $W\ m^{-2}$. In order to compare solar cells, these quantities should refer to standard conditions. This includes a light intensity of $1000\ W\ m^{-2}$, a spectral distribution of AM1.5G – corresponding to the spectrum of light after passing 1.5 times the atmosphere – and a temperature of $25\ ^\circ C$. The V_{OC} and FF are usually not really affected by these parameters, while J_{SC} strongly depends on intensity. For this reason J_{SC} is usually more accurately determined by means of a so-called *EQE* (or *IPCE*) measurement (Chapter 8.1).

2.4 The *p-n* junction based model

The dark current density-voltage (J_D - V) characteristics of organic BHJ solar cells show three regimes (Figure 5). At low voltage, parasitical currents between the electrodes dominate the current, referred to as leakage current, usually described as

$$i_{leakage} = \frac{V_a}{R_{SH}}, \quad (2.5)$$

with R_{SH} the so-called shunt resistance and V_a the applied voltage. The second regime is called the diffusion regime, where the solar cell behaves like a diode as described by the Shockley diode equation:

$$J_D = J_s \left[\exp\left(\frac{V_a}{nV_T}\right) - 1 \right], \quad (2.6)$$

with J_s the saturation current density, V_a the applied voltage, n the ideality factor and V_T the thermal voltage, i.e.

$$V_T = \frac{k_B T}{q}, \quad (2.7)$$

where k_B is Boltzmann's constant, T the absolute temperature and q the elementary charge. The ideality factor n can be determined from measuring the slope in units of V_T , which equals unity in the absence of recombination. The third regime is the space-charge limited regime. This is the regime where the current is dominated by drift, which corresponds to the voltage being larger than the so-called built-in voltage.

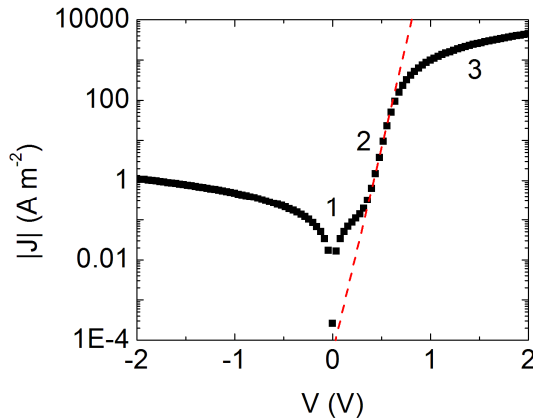


Figure 5: J - V characteristics in the dark for the P3HT:PCBM (low ohmic PEDOT:PSS) solar cell of Figure 4. The ideality factor n is a measure for the slope (dashed line) in the diffusion regime.

In case of illumination of a conventional p - n junction solar cell, the current density under illumination (J_L) is described by

$$J_L = J_s \left[\exp\left(\frac{V_a}{nV_T}\right) - 1 \right] - J_{PH}, \quad (2.8)$$

with J_{PH} the photogenerated current density. For an ideal solar cell $J_{PH} = J_{SC}$, regardless the applied voltage. Consequently, V_{OC} is then determined from

$$V_{OC} = nV_T \ln\left[\left(\frac{J_{SC}}{J_s}\right) + 1\right]. \quad (2.9)$$

From Eq. (2.9) it can be seen that V_{OC} as a function of the logarithm of intensity – provided that the intensity is linear to J_{SC} – must exhibit a slope of nV_T .

By contrast, organic solar cells do not behave accordingly. The origin of this disagreement lies in the fact that for organic solar cells J_{PH} strongly depends on the applied voltage. Therefore, the p - n junction model is not so well applicable to organic BHJ solar cells. Nevertheless, throughout this research the p - n junction model is used to obtain some useful predictions, although it had to be modified in order to apply it to organic solar cells (Chapter 3.4).

2.5 The MIM model

Koster et al. have developed a numerical device model that describes the current-voltage characteristics of BHJ solar cells better than the p - n junction based model.^[12] This model, also known as the metal-insulator-metal (MIM) or drift-diffusion model, is based on an effective

medium approach, treating the donor-acceptor blend as one intrinsic semiconductor. The model considers both drift and diffusion of free carriers in one dimension across the active layer, bimolecular recombination, and the effect of space charge on the electric field across the active layer. An effective band gap is assumed for the “fictive” intrinsic semiconductor chosen as the energy difference between the donor’s HOMO and the acceptor’s LUMO.

The equations used to describe the transport through the semiconductor are the Poisson equation and the current continuity equations. The Poisson equation relates the potential $\psi(x)$ to the electron and hole densities $n(x)$ and $p(x)$ according to

$$\nabla^2\psi(x) = \frac{q}{\varepsilon}[n(x) - p(x)], \quad (2.10)$$

with q the elementary charge, ε the dielectric constant, and the difference $n(x) - p(x)$ the net space charge.

The current continuity equations relates the electron (hole) current density $J_{n(p)}(x)$ to the net generation rate $U(x)$ according to

$$\nabla J_n(x) = -qU(x), \quad (2.11)$$

$$\nabla J_p(x) = qU(x), \quad (2.12)$$

with the net generation obtained from the difference between the generation and recombination rates of free carriers:

$$U = PG_{e-h} - (1 - P)R, \quad (2.13)$$

with P the dissociation probability, G_{e-h} the generation rate of bound electron-hole pairs, and R the recombination rate of charge carriers.

The local current density of electrons and holes in the active layer is the sum of the drift and diffusion currents, i.e.

$$J_n(x) = -q\mu_n[n(x)\nabla\psi(x) - V_T\nabla n(x)], \quad (2.14)$$

$$J_p(x) = -q\mu_p[p(x)\nabla\psi(x) + V_T\nabla p(x)], \quad (2.15)$$

where $\mu_{n(p)}$ is the electron (hole) mobility and V_T the thermal voltage defined by Eq. (2.7). The total current density across the solar cell is the sum of the electron and hole current densities.

To numerically simulate a J - V curve, the Poisson equation and continuity equation are solved iteratively. To obtain a unique solution for Eqs. (2.10)-(2.15), boundary conditions have to be set by the carrier densities and the potentials at the contacts.

2.6 The Shockley-Queisser limit

The most fundamental losses for a single p - n junction solar cell are described by the Shockley-Queisser limit or detailed balance limit.^[10] For a semiconductor with a band gap of 1.34 eV, the limit predicts a maximum power conversion efficiency of 33.7%. The calculation is based on three considerations. The first consideration is the blackbody radiation of the solar cell at room temperature, the baseline energy that is always emitted. Secondly, radiative recombination is

considered according to the principle of detailed balance. This implies that the time-reversed process of absorption also should be possible, i.e. recombination under emission of a photon. Thirdly, spectrum losses are taken into account corresponding to the vast majority of lost power. According to the ultimate efficiency hypothesis each photon with energy greater than $h\nu_g$ produces one electronic charge q at a voltage $V_g = h\nu_g / q$. The excess energy is converted into heat because the excited electron quickly relaxes to the band edge. These are so-called thermalization losses that limit the open-circuit voltage. Any photon with an energy smaller than $h\nu_g$ cannot be absorbed by the solar cell nor generate current. These are so-called transmission losses that limit the short-circuit current. Taking the AM1.5G solar spectrum into account, about half of the solar power is lost accordingly. This third consideration requires fine tuning of the band gap. If the band gap is too large, a large portion of the solar spectrum will not be absorbed causing a small current. If it is too small, a larger amount of energy will be converted into heat and a low voltage is generated. The Shockley-Queisser limit for silicon – having a band gap of 1.1 eV – is about 30%. Calculating the Shockley-Queisser limit for organic bulk heterojunction solar cells is somewhat more complicated.^{[13],[14],[15],[16]} The D/A interface introduces the possibility to form a charge transfer (CT) state with energy E_{CT} , being lower than the band gap of both semiconductors to ensure successful electron or hole transfer. This energetic offset $E_g - E_{CT}$ functions as the driving force for the photoinduced charge transfer but introduces a fundamental loss as well. In other words, the efficiency limit depends on both the band gap and the exciton binding energy.

2.7 Other loss mechanisms in organic BHJ solar cells

As discussed, exciton dissociation at the D/A interface does not directly yield free charge carriers, but rather bound electron-hole pairs. The generation of free charge carriers is implemented in the MIM model by Onsager’s theory on geminate recombination,^{[17],[18]} with an important refinement performed by Braun.^[19] Once free charges are generated, the charges might still recombine. The two main mechanisms to describe these recombination processes in the photoactive layer of organic solar cells are Langevin and Shockley-Read-Hall (SRH) recombination. Even when free charge carriers reach the metal, recombination might take place in the form of exciton quenching.^{[20],[21]}

2.7.1 Langevin recombination

Already in 1903, Langevin proposed a recombination law for ions,^[22] stating that the recombination rate is proportional to the density of the charge carriers that recombine, with the proportionality constant given by

$$k_r = \frac{q}{\epsilon}(\mu_n + \mu_p), \quad (2.16)$$

which is nowadays known as Langevin's recombination constant. Several authors have reported that the bimolecular recombination constant in organic bulk heterojunction solar cells can be orders of magnitude smaller. This recombination constant is therefore referred to as the reduced Langevin constant. The underlying physical processes for the reduced Langevin constant are still under discussion.^{[23],[24],[25],[26],[27]} Notwithstanding this enormous reduction, this Langevin-type bimolecular recombination still strongly affects the performance characteristics like the open-circuit voltage.^[28]

2.7.2 Shockley-Read-Hall recombination

When electron traps are present, also trap-assisted recombination contributes to the loss mechanisms in the solar cell.^{[29],[30]} The trap-assisted recombination rate is given by the Shockley-Read-Hall (SRH) equation

$$R_{SRH} = \frac{C_n C_p N_t (np - n_1 p_1)}{C_n (n + n_1) + C_p (p + p_1)}, \quad (2.17)$$

with C_n and C_p the capture coefficients for electrons and holes respectively, N_t the density of electron traps, n and p the electron and hole densities, and $n_1 p_1 = n_i^2$ their product under equilibrium conditions.

2.8 Koster's equation for the open-circuit voltage

Within the framework of the MIM model an equation for the V_{OC} is derived by Koster e.a. as an alternative for Eq. (2.9).^[31] First the quasi-Fermi potentials $\phi_{n,p}$ are defined as

$$n(p) = n_{\text{int}} \exp\left[(-) \frac{\psi - \phi_{n(p)}}{V_T}\right], \quad (2.18)$$

with the intrinsic concentration of both electrons and holes given by

$$n_{\text{int}} = N_{CV} \exp\left[-\frac{E_{\text{gap}}^{\text{eff}}}{2qV_t}\right], \quad (2.19)$$

where N_{CV} is the effective density of states of valence and conduction bands, and $E_{\text{gap}}^{\text{eff}}$ the effective band gap.

When the system is not in equilibrium, the product of the electron and hole densities is given by

$$np = n_{\text{int}}^2 \exp\left[\frac{\phi_p - \phi_n}{V_t}\right]. \quad (2.20)$$

The current densities, given in Eq. (2.13) and (2.14), can be rewritten in terms of the quasi-Fermi potentials according to

$$J_{n(p)} = -q\mu_{n(p)} n(p) \frac{\partial}{\partial x} \phi_{n(p)}. \quad (2.21)$$

Under open-circuit conditions the current densities are (virtually) zero, which makes the quasi-Fermi levels constant. Moreover, the quasi-Fermi levels have to be equal to the potential at the contacts, because the contacts are in thermal equilibrium. Hence, the difference $\varphi_p - \varphi_n$ is constant throughout the device and equal to the V_{OC} , which implies

$$np = n_{\text{int}}^2 \exp\left[\frac{V_{OC}}{V_T}\right]. \quad (2.22)$$

Since the current densities are zero at the V_{OC} , their derivatives vanish as well. Therefore, from Eq. (2.11) it follows that

$$G_{e-h} = \frac{(1-P)}{P} R. \quad (2.23)$$

When Langevin recombination is the only loss mechanism, the recombination rate of charge carriers R is described by

$$R_L = k_r (np - n_{\text{int}}^2), \quad (2.24)$$

with k_r the reduced Langevin constant. Eq. (2.24) can to a very good approximation be written as $R_L = k_r np$, which yields from Eq. (2.22)

$$V_{OC} = \frac{E_{\text{gap}}^{\text{eff}}}{q} - V_T \ln\left[\frac{(1-P)k_r N_{CV}^2}{PG_{e-h}}\right]. \quad (2.25)$$

Since P and k_r do not depend on intensity, one obtains by assuming $G_{e-h} \propto I$,¹

$$V_{OC} = C + V_T \ln(I), \quad (2.26)$$

with C a constant value. When V_{OC} is plotted as a function of the natural logarithm of intensity one should thus obtain a slope (S) equal to unity in units of V_T .

¹ Chapter 6.3 discusses the effect on the V_{OC} for a power law dependence of G on intensity.

3 Measuring methods

The open-circuit voltage (V_{OC}) is one of the key parameters in the power conversion efficiency (PCE) of solar cells, given by Eq. (2.4). In order to optimize the performance of organic photovoltaic devices, it is important to understand which parameters determine the V_{OC} . In literature the V_{OC} is often assumed to be linearly dependent on the logarithm of intensity according to

$$V_{OC} = C + SV_T \ln(I), \quad (3.1)$$

where S , the slope in units of the thermal voltage V_T , and C are constant values. For several organic solar cells an S -value of 1 has been reported in accordance with Koster's equation, i.e. Eq. (2.25).

Several authors reported that the main signature of SRH-recombination is the enhanced dependence of the V_{OC} on the light intensity corresponding to a value of S larger than unity.^{[32],[33],[34]} It was shown in 1957 by a theoretical analysis of Sah, Noyce and Shockley that the presence of SRH recombination results in an enhancement of the ideality factor, reaching a value of 2 for dominant trap-assisted recombination.^[35] Accordingly, it was stated by Wetzelaer e.a. that an S -value of 2 indicates pure SRH-recombination,^[32] while a value of 1 indicates Langevin recombination. For several solar cells values between 1 and 2 have been reported. For example, Wetzelaer e.a. report for P3HT:PCBM an S -value of 1.25. Such values were concluded to be a fingerprint of both two types of recombination.

It was predicted by Mandoc e.a. that a decreasing value of S would be obtained for increasing intensity.^[33] This prediction was based on the fact that an increasing light intensity leads to an enhanced carrier density in the device. With the Langevin recombination becoming quadratically stronger ($\sim np$) and eventually taking over the trap-assisted recombination ($\sim n(p)$), they expected to see a crossover point marking the intensity regime where Langevin recombination is dominant. However, this prediction was not experimentally verified.

Alternatively, one might reason that for increasing intensity more and more trap states become occupied. With the total amount of trap states being constant this would reduce the chance for SRH-recombination at large intensities thereby inducing a decrease of S .

The aim of this thesis is to accurately study the light intensity dependence of the open-circuit voltage. This Chapter introduces six experimental methods which will be applied in Chapter 5 to the organic solar cells introduced in Chapter 4. All methods show that the slope of V_{OC} as a function of the natural logarithm of intensity is not constant. In other words, S depends on the light intensity as well. More specific, the slope is found to decrease with increasing intensity for all investigated organic solar cells. For some solar cells even values smaller than unity are obtained for S . From these results it is concluded that it does not really make sense to report average values for S over a large intensity regime. The main reason that such accurate results are obtained is the use of a monochromatic laser instead of a spectrally broad lamp.

3.1 Intensity dependence of the open-circuit voltage

To investigate the intensity dependence of the open-circuit voltage, initially a Steuernagel SolarConstant 1200 metal halide lamp (Solar Simulator) is used as the light source, illuminating the P3HT:PCBM solar cell of Figure 4. The disadvantage of the Solar Simulator compared to a laser is that it emits a spectrum of light. When one uses neutral density filters to adjust the intensity, the spectral distribution changes because the transmission depends on the wavelength. Therefore it requires a lot of work to obtain accurate results with the Solar Simulator. The use of assumptions decreases the amount of work but induces substantial errors as well. Usually one puts the solar cell at such a distance from the lamp, that the intensity is about 1 kW m^{-2} (1 Sun-equivalent), which is determined by means of a silicon photodiode. Subsequently, calibrated neutral density filters are used to adjust the light intensity. One method often used to determine the intensity assumes that the filters are grey, meaning that they have a transmission coefficient T being independent of the wavelength of the incoming light.² With that assumption one concludes that the transmitted intensity is a fraction T of the original intensity.

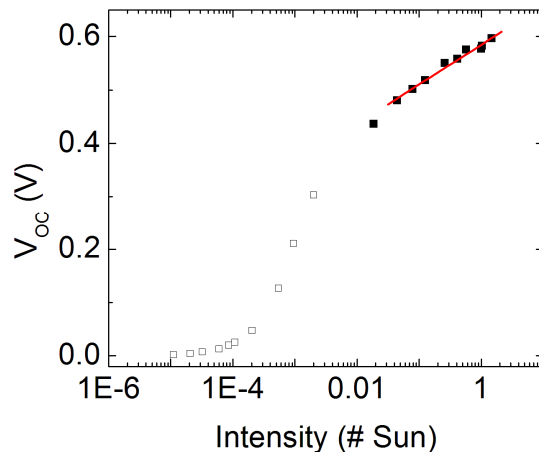


Figure 6: V_{OC} as a function of intensity in number of Sun-equivalents for the P3HT:PCBM (low ohmic PEDOT:PSS) solar cell of Figure 4, with a Steuernagel SolarConstant 1200 metal halide lamp (Solar Simulator) as light source. The slope of the red line is 1.3 in units of V_T . The measurement points where V_{OC} is found to be affected by leakage are marked with open symbols. These data are plotted on logarithmic scale in Figure 9.

Another method to estimate the intensity of the light passing different filters is by measuring the short-circuit current i_{SC} in the organic solar cell. Under the assumption that $i_{SC} \propto I$, the intensity is determined by calculating the fraction of i_{SC} with respect to the 1 Sun-equivalent case. This latter method was used to obtain Figure 6. The measured V_{OC} is plotted as a functi-

² The value of T is obtained by averaging the wavelength dependent transmission coefficient $T(\lambda)$. An improvement on determining the intensity would be to integrate the light spectrum after multiplication with $T(\lambda)$.

on of number of Sun-equivalents. The measurement points where V_{OC} is found to be affected by leakage are marked with open symbols.³

3.2 Methods for determination of S

The large amount of scatter obtained in the plot when measuring the light intensity with the Solar Simulator illustrates the need for an alternative method. Therefore from Chapter 5 a laser will be used as the light source and a silicon photodiode to determine the intensity. Six experimental methods will be performed to determine S , of which the approaches are discussed here. Method I is the only method which assumes a constant S . Methods I and II have also been performed with the Solar Simulator as the light source for which the results are discussed in Chapter 3.2.1 and 3.2.2 as applied to the P3HT-L Ω solar cell. The results of the six methods with the laser as light source are given in Chapter 5.

Throughout this thesis S is defined as ‘the slope in units of V_T for V_{OC} as a function of the natural logarithm of I over an intensity regime ΔI . In contrast to Eq. (3.1), this definition does not imply that S has to be constant as a function of intensity. The objective of this research is to accurately measure S as a function of intensity. In order to do so, Eq. (3.1) is assumed to be valid between two measurement points with intensity difference ΔI . This assumption is only valid if C and S can assumed to be constant between these two measurement points. Ideally, ΔI should thus be as small as possible.⁴

3.2.1 Method I: S from linear fitting

The usual way in literature to express the intensity dependence of the V_{OC} is performed by assuming a constant value for S , according to

$$S = \frac{\log(e)}{V_T} \frac{\Delta V_{OC}}{\Delta \log(I)}, \quad (3.2)$$

where the conversion factor $^{10}\log(e)$ comes from the fact that V_{OC} is plotted against the base ten logarithm instead of the natural logarithm. This change of base proceeds according to

$$\ln(I) = \frac{^{10}\log(I)}{^{10}\log(e)}. \quad (3.3)$$

As the measurement points of Figure 6 where V_{OC} is not affected by leakage do not lie on a smooth curve, no reliable quantitative conclusion can be drawn. If one would nevertheless determine one value for S for this regime, one obtains $S \approx 1.3$ from the slope of the red line in Figure 6. The use of a laser in Chapter 5 produces much more accurate results for the measurement of V_{OC} as a function of intensity. From these results it will be concluded that the dependence of V_{OC} on intensity in the regime that is not affected by leakage cannot be described

³ The measurements that are affected by leakage are determined experimentally by plotting V_{OC} as a function of intensity on logarithmic scale. The measurements with an intensity below the point of deflection are affected by leakage. In this regard, see also Chapter 3.3.

⁴ Note that error analysis (Chapter 5.7) gives a lower bound for ΔI .

by a constant slope. Consequently, producing a constant value for S seems to be rather useless. Therefore the objective of this thesis is to accurately measure the light intensity dependence of S .

3.2.2 Method II: S from differentiation

By assuming

$$\frac{dV_{oc}}{d \ln(I)} = \frac{\Delta V_{oc}}{\Delta \ln(I)}, \quad (3.4)$$

differentiation of a series of measurement values yields from Eq. (3.1)

$$S = V_T^{-1} \frac{dV_{oc}}{d \ln(I)} = \frac{\log(e)}{V_T} \frac{dV_{oc}}{d \log(I)}. \quad (3.5)$$

Applying this method to the measurement results of Figure 6 yields Figure 7. The scatter of the data points at large intensities is caused by the scatter in Figure 6. It will be found that the use of a laser produces somewhat more accurate results for this method (Chapter 5.2.2). However, error analysis (Chapter 5.7) will show that the error in S becomes large for a small ratio of $\Delta I/I$.

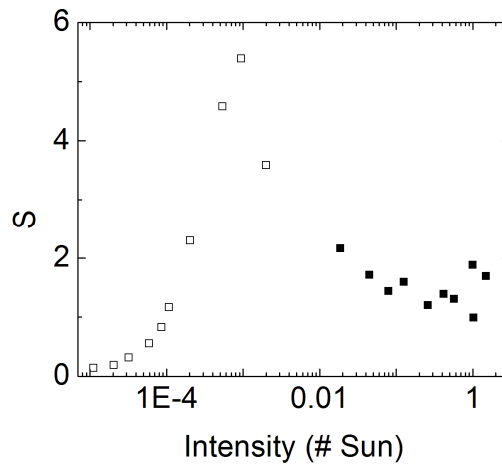


Figure 7: S determined from Figure 6 using Eq. (3.5). The measurement points where V_{oc} is found to be affected by leakage are marked with open symbols. These data are plotted on logarithmic scale in Figure 10.

3.2.3 Determining S from the slope between $V_{oc}(I)$ and $V_{oc}(I+\Delta I)$

From Eq. (3.1) the change in V_{oc} between two measurement points with difference ΔI can be determined from

$$\Delta V_{oc} = S V_T \Delta \ln(I), \quad (3.6)$$

where

$$\Delta \ln(I) = \ln(I + \Delta I) - \ln(I). \quad (3.7)$$

Consequently, S can be determined from the change in V_{oc} and I between the two values according to

$$S = \frac{\Delta V_{OC}}{V_T \ln\left(1 + \frac{\Delta I}{I}\right)}. \quad (3.8)$$

The two measurement points have V_{OC} induced by intensity I and $I+\Delta I$ respectively. Measuring S accordingly for a series of measurement points yields S as a function of intensity. Methods III, V and VI use Eq. (3.8) to determine S .

3.2.4 Method III: Selection via $1 < \Delta I/I < 2$

In this method S is determined according to Eq. (3.8) where several pairs of measurement points are selected from the plot of V_{OC} as a function of intensity. The difference in intensity between the two measurement points of such a pair is defined here as ΔI . Via error analysis it will be determined in Chapter 5.7 that σ_s , the standard deviation of S , might become very large for a small ratio of $\Delta I/I$. Therefore each pair of measurement points is selected to satisfy $\Delta I/I > 1$. Also, $\Delta I/I$ does not exceed the value of 2 in order to keep the ratio relatively small.

3.2.5 Method IV: Polynomial fits

If one could find a function that fits to the experimental results of V_{OC} as a function of the natural logarithm of intensity, one could easily determine S from applying Eq. (3.5) to this function. When an n^{th} order polynomial is used for this, the polynomial satisfies

$$V_{OC} = \sum_{i=0}^n C_i [\ln(I)]^i, \quad (3.9)$$

where each C_i is a constant value obtained from fitting. Taking the derivative of Eq. (3.9) with respect to $\ln(I)$ one obtains

$$\frac{dV_{OC}}{d \ln(I)} = \sum_{i=1}^n i C_i [\ln(I)]^{i-1}. \quad (3.10)$$

From Eq. (3.5) one obtains

$$\frac{dV_{OC}}{d \ln(I)} = S V_T. \quad (3.11)$$

Equalizing Eq. (3.10) and Eq. (3.11) yields

$$S = \sum_{i=1}^n \frac{i C_i}{V_T} [\ln(I)]^{i-1}. \quad (3.12)$$

3.2.6 Method V: Using a beam splitter

If the ratio $\Delta I/I$ is taken constant, the value of $\Delta \ln(I)$ becomes constant as well. Any I and its associated $I+\Delta I$ are then equidistant, when plotted on logarithmic scale. One way to obtain a more or less constant ratio of $\Delta I/I$ experimentally, is the use of a beam splitter. In method III, S is determined from selecting two measurement points of the measurement of V_{OC} as a func-

tion of intensity. Instead, each pair of intensities I and $I+\Delta I$ is in Method V obtained from a single laser beam passing the beam splitter. S is determined according to Eq. (3.8), with

$$\Delta V_{OC} = V_{OC}(I + \Delta I) - V_{OC}(I), \quad (3.13)$$

where $V_{OC}(I+\Delta I)$ is the V_{OC} induced by the light with intensity $I+\Delta I$, and $V_{OC}(I)$ the V_{OC} induced by the light with intensity I .

3.2.7 Method VI: The SSDV technique

The steady-state differential voltage (SSDV) technique is introduced in this thesis as a new technique to accurately measure the intensity dependence of the open-circuit voltage. The experimental setup is described in Chapter 5.3 and in detail in Chapter 8.3. This method to determine S is an extension of Method V, with the advantage that ΔV_{OC} (Eq. (3.13)) does not have to be determined manually but is obtained from the use of a chopper in conjunction with a lock-in amplifier. Again, S is obtained from Eq. (3.8).

The SSDV technique is quite similar to the transient photovoltage (TPV) technique.^[36] However, in case of a TPV measurement one is interested in the decay dynamics as a function of time, while during an SSDV measurement steady-state conditions are required, which means that these decay dynamics are not allowed to play a role. Steady-state is the equilibrium condition when the charge carrier density does not change as a function of time.^[37] For the SSDV measurement steady-state conditions are satisfied when the charge carrier lifetime τ , a measure for the decay dynamics, is much lower than the period of the voltage oscillation. Durrant e.a. have proposed a power law decrease for τ as a function of charge carrier density n according to

$$\tau(n) = \tau_0 n^{-\lambda}, \quad (3.14)$$

with n the charge carrier density and λ the magnitude of the slope.^[28] Because the charge carrier density is to a good approximation linearly dependent upon intensity, it is to be expected that τ increases similarly with decreasing intensity. This gives a lower limit for the light intensity to satisfy steady-state conditions, which is a disadvantage of the SSDV technique. This limitation does not play a role for Method V which thus might be the preferable method when one is interested in the behavior of S for low intensities.

3.3 Influence of leakage current

In order to understand the influence of leakage on the intensity dependence of V_{OC} , it is useful to consider the experimental relation

$$J_{Leakage} \propto V^\beta. \quad (3.15)$$

For the P3HT:PCBM solar cell of Figure 4 one obtains $\beta \approx 1.03$ from Figure 8.

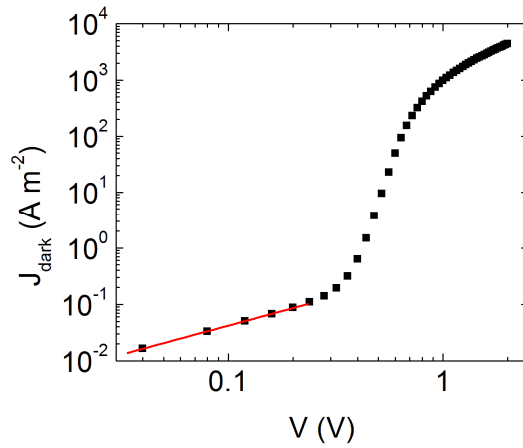


Figure 8: The dark current density as a function of applied voltage plotted on logarithmic scale as measured for the P3HT:PCBM (low ohmic PEDOT:PSS) solar cell of Figure 4. From the slope of the red line one would estimate $\beta \approx 1.03$.

Under illumination the current density can be described as

$$J_L = -J_{SC} + J_{Leakage}, \quad (3.16)$$

In V_{OC} the value of J_L is zero by definition, which implies

$$J_{SC} \propto V_{OC}^\beta. \quad (3.17)$$

For low intensities the relation $i_{sc} \propto I$ is valid, which transforms Eq. (3.17) into

$$V_{OC} \propto I^{\beta^{-1}}. \quad (3.18)$$

Note that Eq. (3.18) only holds for the intensity regime where V_{OC} is affected by leakage. It implies that measuring V_{OC} as a function of I yields on logarithmic scale a constant slope with value β^{-1} . The measurement results of Figure 6 are plotted on logarithmic scale in Figure 9.

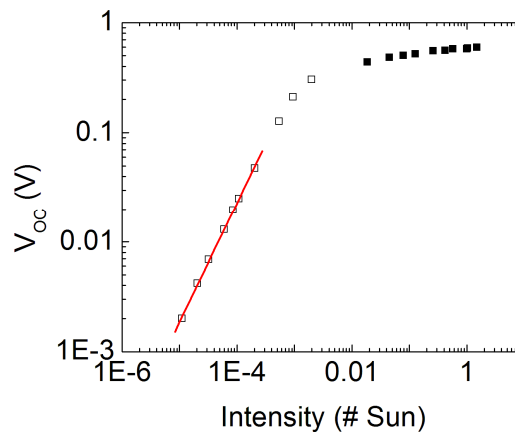


Figure 9: The data of Figure 6 are plotted here on logarithmic scale. The measurement points where V_{OC} is found to be affected by leakage are marked with open symbols. From the slope of the red line one would estimate $\beta^{-1} \approx 1.09$.

The value of the slope is 1.09, but the inverse is not equal to the β -value determined in Figure 8. This inconsistency might be due to the inability to determine the intensity of the Solar Simulator accurately.

Note that the point of deflection is a useful benchmark to distinguish experimentally whether leakage current affects the measurement at a specific intensity. The open symbols in the plots for V_{OC} and S originate from the measurement points to the left of it. The data points where V_{OC} is affected by leakage are in fact just measurement artefacts and should thus be neglected.

It is recommended to determine S according to either Eq. (3.8) or (3.5). Nonetheless, to predict the behavior of S in the regime where V_{OC} is affected by leakage, it is useful to take an alternative expression for S into account. Assuming

$$\frac{dV_{OC}}{dI} = \frac{\Delta V_{OC}}{\Delta I} ,$$

yields

$$\frac{dV_{OC}}{dI} = \frac{SV_T}{I} . \quad (3.19)$$

Like before, this is only valid when C and S do not differ much between two measurement points. One now estimates S from

$$S = \frac{I}{V_T} \frac{dV_{OC}}{dI} . \quad (3.20)$$

Note that this causes an additional error, with the size of the ratio of Eq. (3.8) and (3.20), i.e.

$$\frac{\ln(1 + \Delta I/I)}{\Delta I/I} .$$

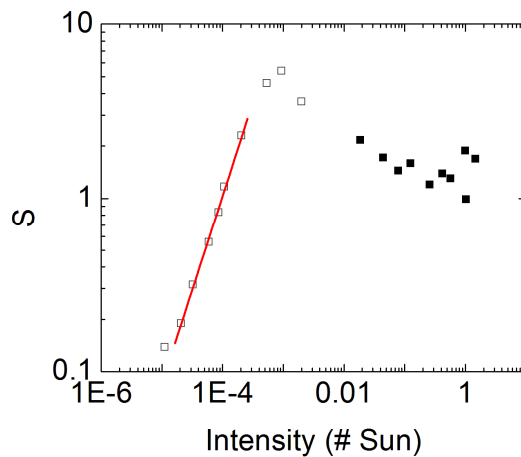


Figure 10: The data from Figure 7 are plotted here on logarithmic scale. The measurement points where V_{OC} is found to be affected by leakage are marked with open symbols. From the slope of the red line one would estimate $\beta^{-1} \approx 1.08$.

This error makes Eq. (3.20) only applicable if $\Delta I \ll I$. Substituting the derivative of Eq. (3.18) into Eq. (3.20) yields

$$S \propto I^{\beta^{-1}}. \quad (3.21)$$

Note that Eq. (3.21) only holds for the intensity regime where V_{OC} is affected by leakage. It implies that measuring S as a function of I yields on logarithmic scale a constant slope with value β^{-1} . The data from Figure 7 are plotted on logarithmic scale in Figure 10. From the slope of the red line one would estimate $\beta^{-1} \approx 1.08$, for which again the inverse is not equal to the β -value determined in Figure 8.

3.4 The p - n junction based model applied to BHJ solar cells

3.4.1 Modelling i - V curves

Besides trying to reproduce measurement results, it is useful to use a model to predict the results in case of different parameters. A model is a useful tool to judge measurement results and to tackle measurement artefacts. In order to describe non-ideal devices like organic BHJ solar cells with the p - n junction model, often parasitic resistances are included in order to improve the fitting to experiments, while the physical meaning of these parameters is usually disregarded. Figure 11 shows the inclusion of a series resistance (R_s) and a shunt resistance (R_{SH}). For convenience, this model will be referred to as ‘the modified p - n junction based model’. In Chapter 3.4 this model is applied to the solar cell of Figure 4, with the Solar Simulator used as light source. In Chapter 5.4 the solar cells introduced in Chapter 4 are used as input for the model. Simulations with this model were performed by implementing it into Matlab (version R2010a).

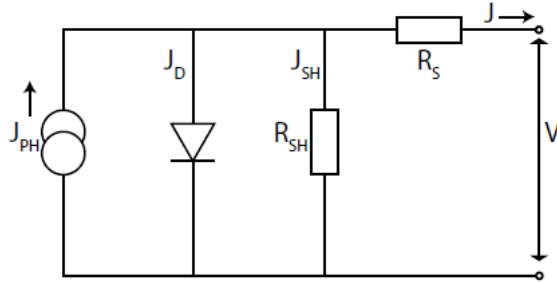


Figure 11: The modified p - n junction based model.

The modified p - n junction based model yields for the current density under illumination

$$J_L = J_s \left[\exp\left(\frac{V_a - J_L R_s}{nV_T}\right) - 1 \right] - J_{PH} + \frac{V_a - J_L R_s}{R_{SH}}. \quad (3.22)$$

Instead of focusing on current density the model was encoded to solve for current (i) according to

$$0 = -i_L - i_{PH} + i_s \left[\exp\left(\frac{V_a - i_L R_s}{nV_T}\right) - 1 \right] + \frac{V_a - i_L R_s}{R_{SH}}. \quad (3.23)$$

The current under illumination i_L can be solved numerically, which is performed in Chapter 8.7.1 where i_L is referred to as x . Varying V_a in the model (usually in steps of $h = 10^{-3}$ V) yields i_L as a function of V_a , which produces an i - V curve. The photogenerated current i_{PH} is assumed to be equal to the short-circuit current i_{SC} , measured with the solar simulator under (approximately) 1 Sun conditions. For n the value 1 is used. In the dark, $i_{PH} = 0$, which simplifies (3.23) to

$$i_D = i_s \left[\exp\left(\frac{V_a - i_D R_s}{nV_T}\right) - 1 \right] + \frac{V_a - i_D R_s}{R_{SH}}. \quad (3.24)$$

For small V_a and i_D , and using $R_{SH} \gg R_s$, this further simplifies to

$$i_D = \frac{V_a}{R_{SH}}, \quad (3.25)$$

which shows that around $i_D = 0$ the slope of the i - V curve in the dark is $1/R_{SH}$. Therefore fitting the dark current allows to determine R_{SH} , as performed in Figure 12 for the P3HT-L Ω solar cell of Figure 4, where R_{SH} is found to amount $0.25 \text{ M}\Omega$. As R_s determines the behavior of the i - V curve around V_{OC} , an estimate for R_s is obtained by varying it until the modelled i - V curve fits at V_{OC} to the measured i - V curve. Likewise, an estimate for the saturation current i_s is obtained by varying it until a good fit is achieved.

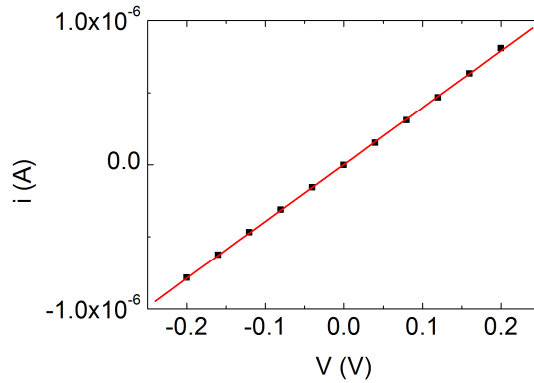


Figure 12: From the inset of Figure 4 the i - V curve in the dark for the P3HT-L Ω solar cell is shown on linear scale around $V_a = 0$. A value of $0.25 \text{ M}\Omega$ is obtained for R_{SH} , from the inverse value of the slope.

Fitting the model to the measured i - V curve of the P3HT-L Ω solar cell yields Figure 13. Although a better fit can be obtained by decreasing R_{SH} , it is still recommended to determine R_{SH} from the dark current, in order to be able to predict the behavior of V_{OC} at very low light intensity, as V_{OC} is then solely determined by leakage current.

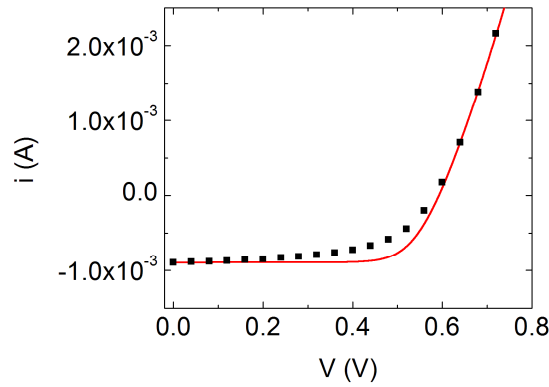


Figure 13: Solving Eq. (3.23) numerically results in i_L as a function of V_a as plotted here for the P3HT-L Ω solar cell of Figure 4. The script and parameters are given in Chapter 8.7.1.

The i - V characteristics at lower light intensities can be predicted by reducing i_{PH} in the model, under the assumptions that $i_{PH} = i_{SC}$ and $i_{SC} \propto I$, and substituting this new i_{PH} into Eq. (3.23). This is performed in Figure 14 where the other parameters are left the same as in Figure 13. Starting from an intensity of 16 Sun-equivalents, every next result has i_{PH} twice as low as the previous one. Figure 14(a) shows i_L as a function of V_a on linear scale, while Figure 14(b) shows the absolute value of i_L on semi-logarithmic scale. Because i_L changes sign at V_{OC} , it peaks there on the semi-logarithmic scale. The influence of leakage current on V_{OC} can already be recognized, because for decreasing i_{PH} V_{OC} suddenly decreases enormously.

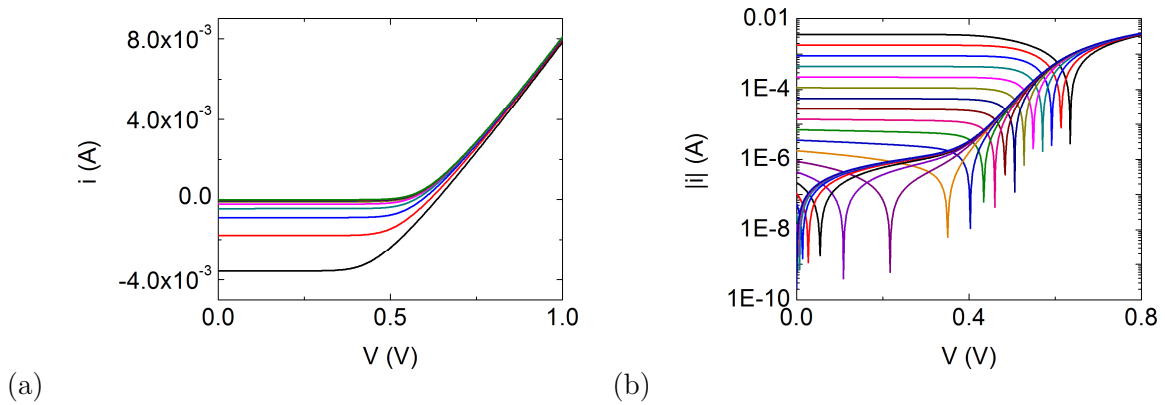


Figure 14: By using the parameters from Figure 13, these results are obtained by varying i_{PH} in Eq. (3.23) and solving for i_L . (a) The i - V curve with the largest intensity has the i_{PH} of Figure 13 being multiplied with 16. For every next result i_{PH} is halved. (b) Analogous to Figure 5, plotting the absolute value of i_L shows the leakage, diffusion and space-charge limited regimes respectively. The curves peak at V_{OC} , where i_L changes sign.

3.4.2 Modelling the intensity dependence of V_{OC}

The bisection method was used to find V_{OC} as a function of intensity for the i - V curves in Figure 14, as described in Chapter 8.7.2.⁵ Alternatively, one could solve V_{OC} numerically as a function of i_{PH} by substituting $i_L = 0$ into Eq. (3.23). Figure 15 shows the results on semi-logarithmic and logarithmic scale respectively. The intensity is plotted in number of Sun-equivalents, determined from the ratio of i_{PH} with respect to the 1 Sun-equivalent case of Figure 13. Similar to Figure 6, Figure 15(a) shows a sudden drop of V_{OC} for decreasing intensity. This drop induces similar to Figure 7 a large value of S , which is the slope in units of V_T . Figure 15(b) shows the same model results plotted on logarithmic scale. When determining the β^{-1} -value from Figure 15(b) similar to Figure 9 according to Eq. (3.18), the value 1 is obtained. This can be understood by considering that $i_L = 0$ at V_{OC} . By substituting this into Eq. (3.23) the last term dominates for i_{PH} in the intensity regime affected by leakage, giving

$$i_{PH} = \frac{V_{OC}}{R_{SH}}, \quad (3.26)$$

which means for the model that β becomes 1 in Eq. (3.17).

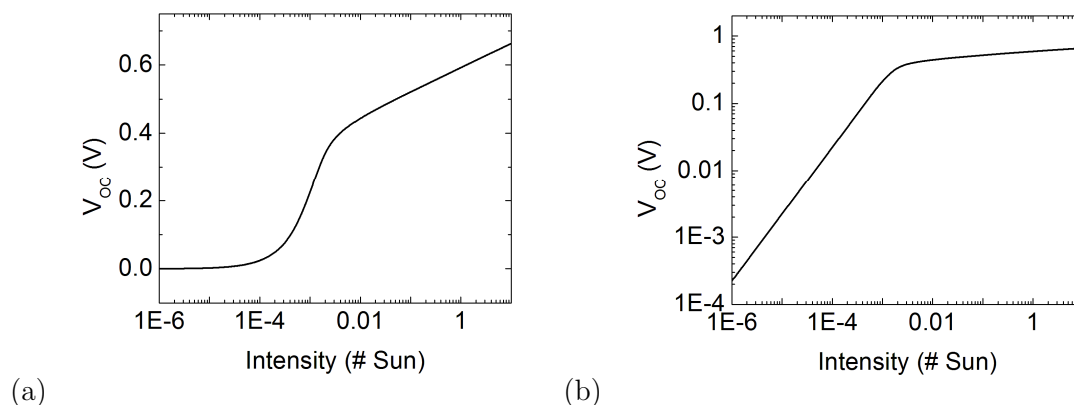


Figure 15: V_{OC} as a function of intensity in number of Sun-equivalents, obtained from Figure 14, plotted on semi-logarithmic (a) and logarithmic scale (b) respectively.

The value of S as a function of intensity has been determined by calculating the slope between two subsequent points in Figure 15 according to Eq. (3.8). Figure 16 shows S plotted on both semi-logarithmic scale and logarithmic scale. For the intensity regime where V_{OC} is not affected by leakage the model predicts the value of S to be constant, being equal to the predefined value of n in Eq. (3.23). Similar to Figure 10, one expects for Figure 16(b) a slope of β^{-1} for the intensity regime where V_{OC} is affected by leakage, according to Eq. (3.21). In line with Figure 15(b) the model yields a β^{-1} -value of 1 for this slope.

⁵ Once V_{OC} is found, it is used as the first right boundary of the bisection method for finding V_{OC} for the curve with the next lower intensity, using the fact that V_{OC} has to decrease as well. Zero voltage functions as the first left boundary.

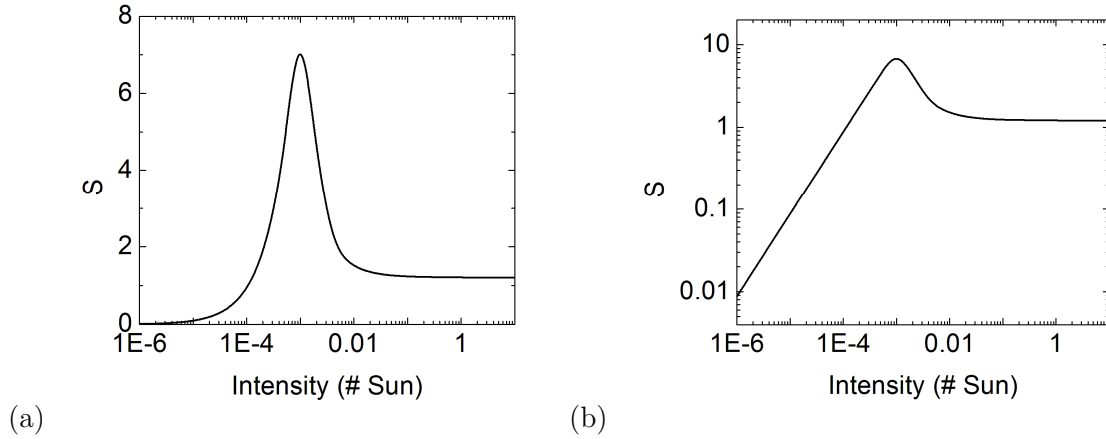


Figure 16: S as a function of intensity in number of Sun-equivalents, obtained from Figure 15, plotted on semi-logarithmic (a) and logarithmic scale (b) respectively.

Chapter 8.4 shows S as a function of intensity for several values of ΔI . From these results it can be seen that it is important to plot S as a function of $I + \Delta I/2$. Nevertheless, this will always be denoted as ‘Intensity’ in the axis labels.

3.4.3 Variation of R_{SH}

In order to predict the intensity dependence of V_{OC} for solar cells with a different value of R_{SH} , the value of R_{SH} is varied. A large value of R_{SH} corresponds to a low leakage current, according to Eq. (3.25). Figure 17 shows V_{OC} as a function of intensity on both semi-logarithmic and logarithmic scale. As to be expected, for increasing R_{SH} the intensity regime where V_{OC} is affected by leakage decreases.

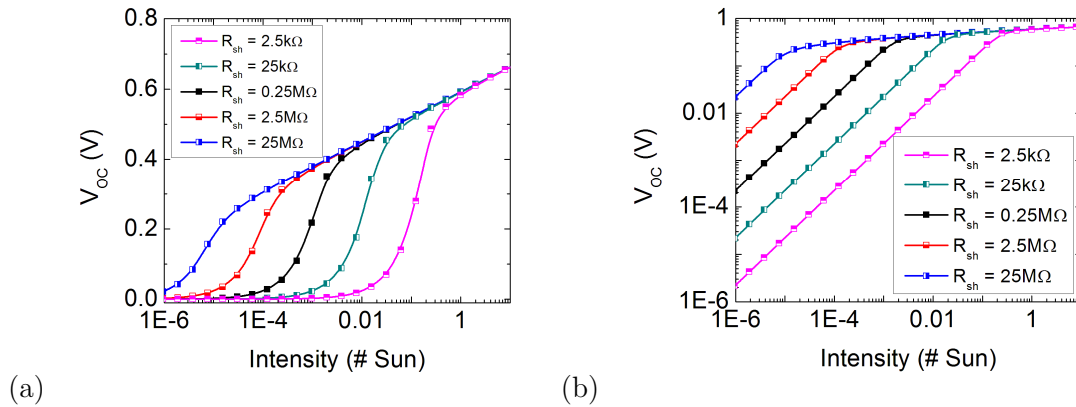


Figure 17: V_{OC} as a function of intensity on semi-logarithmic (a) and logarithmic scale (b) respectively for different values of R_{SH} , where the black line shows the original result of Figure 15.

Figure 18 shows S , the slope in units of V_T , plotted as a function of intensity for the model results of Figure 17(a). The behavior of S is affected less by leakage current for large values of R_{SH} .

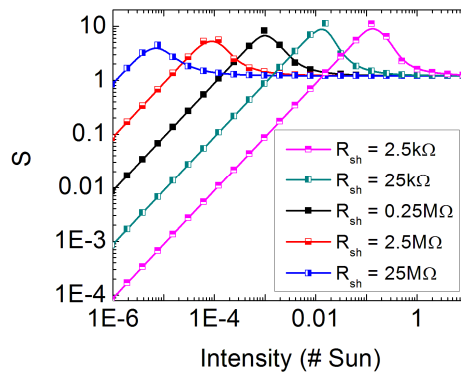


Figure 18: S as a function of intensity on logarithmic scale for different values of R_{sh} , where the black line shows the original result of Figure 15.

4 Device fabrication and characterization

4.1 Fabrication

Five different organic BHJ solar cells are used for the experiments in Chapter 5. Throughout this thesis, these solar cells are abbreviated as P3HT, MEH, T1H Ω , T1L Ω and T1SL Ω , for which the structures are denoted in Table 1 as well. The solar cells are fabricated on a glass substrate, supplied with a layer of indium tin oxide (ITO) which is a transparent conductive oxide (TCO). These substrates were first cleaned, dried, and treated with UV–ozone. A hole transport layer (HTL) consisting of poly(3,4-ethylenedioxythiophene) poly(styrenesulfonate) (PEDOT:PSS, Figure 19) is spin cast on top, which was subsequently dried at 140 °C for about 15 minutes. Together with the ITO this functions as the anode of the solar cell. Three types of PEDOT:PSS are used in order to vary the amount of leakage current in the devices as tabulated in Table 2. These were purchased from H.C. Starck Clevisio GmbH.

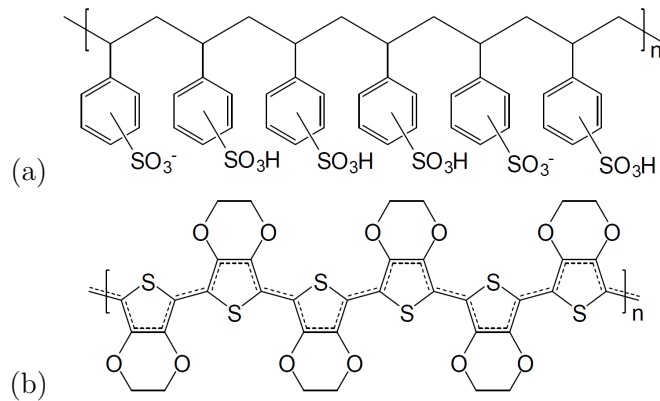


Figure 19: Chemical structure of (a) PEDOT and (b) PSS.

Table 2: Types of PEDOT:PSS.

Commercial name	Name in this thesis	Resistivity (Ω cm)	PEDOT:PSS ratio (by weight)
CH 8000	High Ohmic (H Ω)	$1 \cdot 10^5 - 3 \cdot 10^5$	1:20
AI 4083	Low Ohmic (L Ω)	500-5000	1:6
PH 500	Super Low Ohmic (SL Ω)	$3 \cdot 10^{-3}$	1:2.5

The photoactive layer is made from a donor-acceptor blend. As acceptor material PCBM is used, i.e. either [6,6]-phenyl-C61-butyric acid methyl ester ([60]PCBM, Figure 20) or [6,6]-phenyl-C71-butyric acid methyl ester ([70]PCBM). PCBM was purchased from Solenne BV. For the donor material either polymers or small molecules are used. After preparation of the donor-acceptor blend in solution it is stirred for a day on a magnetic hotplate, which should have a temperature below the boiling point of the solvent. From this step onwards everything takes place in a nitrogen filled glovebox. After spin casting the photoactive layer on top of the anode, annealing might be applied to promote phase segregation, thereby enhancing the per-

formance of the solar cell. The final layer is the cathode which is formed by depositing either a 1 nm layer of lithium fluoride or a 5 nm layer of calcium followed by 100 nm aluminium by means of thermal evaporation under vacuum ($< 10^{-6}$ mbar). This layer acts also as a mirror to reflect the light that has traversed the photoactive layer back into the device.

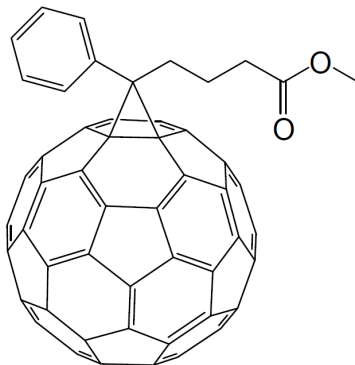


Figure 20: Chemical structure of [60]PCBM.

4.1.1 P3HT

The solar cell referred to as the P3HT solar cell has the polymer regioregular poly(3-hexylthiophene) (RR-P3HT, Figure 21) as donor material and [60]PCBM as acceptor material. The P3HT – purchased from Rieke Metals – has a molecular weight of 50-70K, and a regioregularity of 91-94%. In contrast to the P3HT:PCBM solar cell of Figure 4, this one has high ohmic PEDOT:PSS as the HTL.

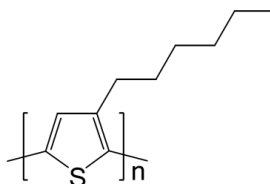


Figure 21: Chemical structure of RR-P3HT.

The spin casting program for PEDOT:PSS is tabulated in Table 3. The active layer is spin cast from a chloroform solution ($[P3HT]=15 \text{ mg mL}^{-1}$), with P3HT and [60]PCBM added as 1:0.8 by weight. The spin casting program is tabulated in Table 4. After spin casting the photoactive layer, the device is annealed for five minutes at $130 \text{ }^{\circ}\text{C}$. The cathode consists of 1 nm LiF and 100 nm Al.

Table 3: Spin casting program for PEDOT:PSS.

	Rotation speed (rpm)	Time (s)
Step 1	500	5
Step 2	4000	60

Table 4: Spin casting program for P3HT:[60]PCBM. This process takes place in a nitrogen filled glovebox.

	Lid position	Rotation speed (rpm)	Acceleration (rpm s ⁻¹)	Time (s)
Step 1	Closed	500	500	3
Step 2	Closed	1000	1000	60
Step 3	Open	1000	1000	30

4.1.2 MEH

The solar cell that is being referred to as the MEH solar cell, has the polymer poly(2-methoxy-5-(2'-ethyl-hexyloxy)-1,4-phenylene vinylene (MEH-PPV, Figure 22) as donor material and [60]PCBM as acceptor material. The MEH-PPV was synthesized by J. Wildeman according to the procedure of Neef and Ferraris.^[38] High ohmic PEDOT:PSS is used, which is spin cast in one step (60s, 2000rpm, 1000rpm s⁻¹) in air. The active layer is spin cast from a chlorobenzene solution, with MEH-PPV and [60]PCBM added as 1:4 by weight. The spin casting program is tabulated in Table 5. The device is not annealed. The cathode consists of 1 nm LiF and 100 nm Al.

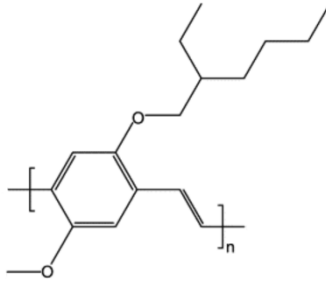


Figure 22: Chemical structure of MEH-PPV.

Table 5: Spin casting program for MEH-PPV:[60]PCBM. This process takes place in a nitrogen filled glovebox.

	Lid position	Rotation speed (rpm)	Acceleration (rpm s ⁻¹)	Time (s)
Step 1	Closed	400	200	4
Step 2	Closed	700	400	120
Step 3	Open	1000	500	70

4.1.3 T1

Three solar cells are referred to as T1, which have the small molecule 7,7'-(4,4-bis(2-ethylhexyl)-4H-silolo[3,2-b:4,5-b']dithiophene-2,6-diyl)bis(6-fluoro-4-(5'-hexyl-[2,2'-bithiophen]-5-yl)benzo[c][1,2,5]thiadiazole) as donor material (p-DTS(FBTTh₂)₂, Figure 23).^[39] As acceptor material [70]PCBM is used. The only difference between these three solar cells is the type of PEDOT:PSS. All three types of PEDOT:PSS in Table 2 are used, which is the reason that these solar cells are referred to as T1HΩ, T1LΩ and T1SLΩ respectively. The spin casting pro-

gram of Table 3 is used for making the PEDOT:PSS layer. The active layers are spin cast from solutions of (p-DTS(FBTTh₂)₂) and [70]PCBM at a weight ratio of 1.5:1 in chlorobenzene with 0.4 v/v% diiodooctane (DIO), at an overall concentration of 35 mg mL⁻¹. The cathodes consist of 5 nm Ca and 100 nm Al.

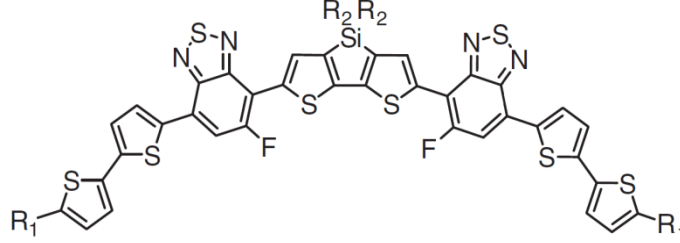


Figure 23: Chemical structure of DTS(FBTTh₂)₂ which is being referred to in this thesis as T1. R₁ = n-hexyl, R₂ = 2-ethylhexyl.

4.2 Thicknesses

Thicknesses are determined by making a scratch in the layer, such that only ITO remains on the glass substrate. The profile over this scratch is measured with a profilometer (Dektak 6M, Veeco) in air. The thickness of the PEDOT:PSS layer is determined before spin casting the photoactive layer. After spin casting the photoactive layer, the thickness is determined by subtracting the thickness of the PEDOT:PSS layer.

Table 6: Thicknesses of the PEDOT:PSS layer and photoactive layer in nm with an accuracy of ± 5 nm.

Solar cell	PEDOT:PSS Thickness (nm)	Active layer Thickness (nm)
P3HT	60	214
MEH	80	133
T1H Ω	60	98
T1L Ω	40	103
T1SL Ω	45	104

4.3 Characterization

Although each device consists of four solar cells, for each device only the one with a size of 16 mm² is characterized here and used in Chapter 5. The five different types of solar cells were characterized by using a computer controlled Keithley 2400 SourceMeter, which measures the current-voltage characteristics both under illumination and in the dark. Using a calibrated silicon diode, the devices were positioned at such a distance from a Steuernagel SolarConstant 1200 metal halide lamp (Solar Simulator) that the intensity was set to about 1000 W m⁻². The characterization is performed under a nitrogen atmosphere. The temperature of the solar cells is kept constant at room temperature by means of cooled nitrogen. In Figure 24 the current

density is plotted as a function of the applied voltage, both under illumination and in the dark (inset).

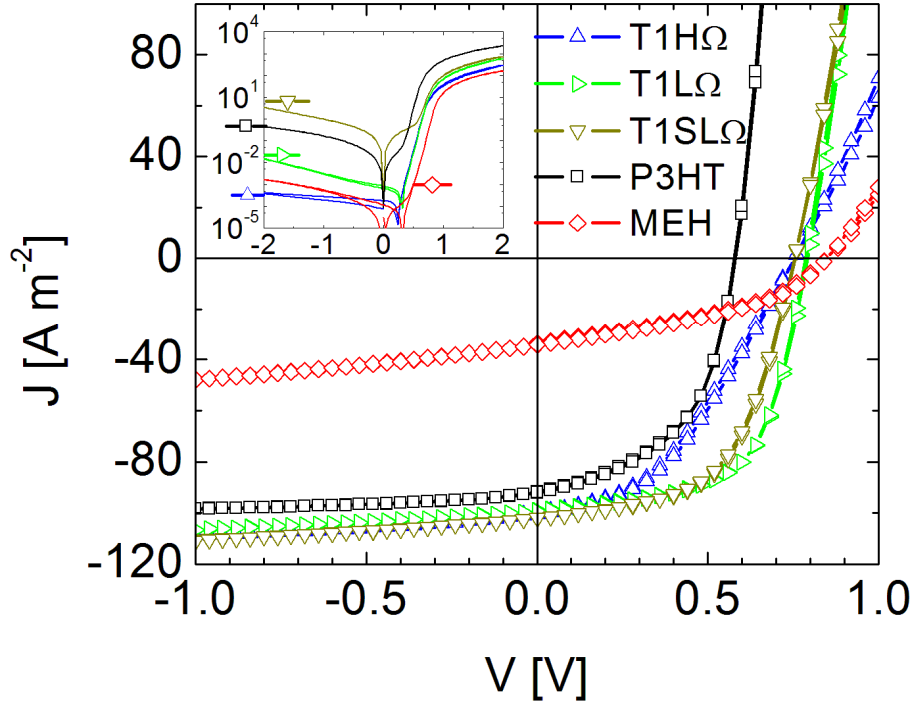


Figure 24: Characterization of the five solar cells introduced in Chapter 4.1. Current density is measured as a function of voltage, both under illumination and in the dark (inset). The solar cell structures are abbreviated according to Table 1 and Chapter 4.1.

From these J - V characteristics the parameters J_{sc} , V_{oc} and FF as defined in Chapter 13, can be determined. However, to ensure that the solar cell is characterized for the standard Air Mass 1.5 Global (AM1.5G) solar spectrum, an EQE -measurement is required, as performed in Chapter 8.1. The J_{sc} is now determined from Eq. (8.3). Assuming that the V_{oc} and FF do not change, one obtains the PCE from Eq. (2.4). These results are tabulated in Table 7.

Table 7: List of parameters showing the performance of the different solar cells for AM1.5G light conditions. The J_{sc} is obtained from Eq. (8.3), by performing an EQE -measurement. The V_{oc} and FF are determined from Figure 24. The power conversion efficiency (PCE) is determined from Eq. (2.4). The solar cell structures are abbreviated according to Table 1 and Chapter 4.1.

Solar cell	J_{sc} (A m ⁻²)	V_{oc} (V)	FF	PCE (%)
P3HT	73.8	0.578	0.52	2.22
MEH	20.4	0.848	0.41	0.71
T1HΩ	95.4	0.754	0.41	2.95
T1LΩ	104.1	0.787	0.62	5.08
T1SLΩ	103.2	0.754	0.57	4.44

5 Experiments

5.1 V_{OC} as a function of laser light intensity

As the source of illumination of the solar cells, a continuous wave laser is used (B&W TEK INC., Model BW1-532-50-E, Class IIIb) producing light with a wavelength of 532 nm and a maximum power of 80 mW. Using a laser has several advantages compared to using a spectrally broad lamp. Spatial coherence allows laser light to be focused onto a tight spot and to be collimated, which allows the target to be placed far apart from the source, thereby decreasing the influence of heating. Due to temporal coherence, a laser produces monochromatic light, which allows easy determination of the intensity by means of measuring the induced current upon illumination of a calibrated photodiode. Altogether, it is to be expected that when using a laser for measuring V_{OC} as a function of light intensity, more accurate results will be obtained compared to conventional measurements with a spectrally broad lamp (Figure 6). The use of a 5X Galilean Beam Expander (Thorlabs, BE05M-A) ensures illumination with a uniform intensity profile. Two wheels of both five neutral density filters are used to modify the light intensity.⁶

In order to determine the intensity of the laser beam, a Keithley 2410 SourceMeter measures the induced short-circuit current i_{SC} in a silicon photodiode (Newport 818-SL, Serial No: 15680). By means of interpolation of the tabulated responsivity values of the photodiode (Figure 48), it has been determined that the responsivity at 532 nm is 0.314 A W^{-1} . A circular aperture with a diameter of $1.77 \pm 0.03 \text{ mm}$ is placed directly in front, $1.8 \pm 0.2 \text{ cm}$ from the solar cell. Because the aperture size is smaller than the area of the solar cells, all light passing the aperture falls within the area of the solar cells. This ensures that both the reference cell (the silicon photodiode) and test cell (the organic solar cell) are illuminated with the same light intensities. Moreover, it was found that the current response of the silicon photodiode was only linearly dependent upon intensity in case of the use of an aperture. An aperture has also the advantage of shielding the solar cell from stray light, while for this reason the sample and aperture are also covered with a box provided with an opening for the incoming laser light.

A beam splitter is used to focus the light onto the solar cell.⁷ The alignment of the laser beam is performed by first adjusting the position of the silicon photodiode behind the aperture and afterwards adjusting the beam splitter, while in both cases maximizing the short-circuit current induced by the beam. To determine the intensity I of the laser beam in W m^{-2} and current density J_{SC} in A m^{-2} , the measured power and current have to be divided by the area of the aperture.

⁶ As both wheels also have an “open” position, 36 intensity combinations were available in a range of six orders of magnitude.

⁷ One could instead use a mirror, but using a beam splitter is more convenient for this setup in view of using it for an SSDV (Chapter 5.3) or SSDC (Chapter 8.2.3) measurement. Then also the transmitted light will be focused onto the solar cell.

The organic solar cells to be investigated are the P3HT, MEH, T1H Ω , T1L Ω and T1SL Ω solar cells introduced in Table 1 and Chapter 4. During their measurement these solar cells are kept in a nitrogen filled sample holder. To compare the intensity of the laser with AM1.5G light, one needs to consider that the amount of absorbed photons depends on the type of materials used in the solar cell. For all measurement results a vertical line will be shown at the laser intensity where the solar cell's induced J_{SC} was found to be equivalent to the J_{SC} at AM1.5G conditions. The values for J_{SC} are obtained from an *EQE* measurement (Chapter 8.1). The corresponding laser intensity has been obtained from interpolation of the measurement results where J_{SC} is measured as a function of intensity (Chapter 8.2). For T1L Ω and T1SL Ω only one line is plotted, because of the minimal difference in intensity.

Table 8: List of laser intensities inducing the same J_{SC} as obtained with AM1.5G light for the solar cells of Figure 24. The solar cell structures are abbreviated according to Table 1 and Chapter 4.1.

Solar cell	J_{SC} (A m ⁻²)	I (W m ⁻²)
P3HT	73.8	279
MEH	20.4	163
T1H Ω	95.4	401
T1L Ω	104.1	439
T1SL Ω	103.2	435

Finally, the V_{OC} is determined with the Keithley 2410 SourceMeter, which has an input impedance of more than 10 G Ω . As discussed before, at low light intensity the V_{OC} might be affected by leakage current. When plotting V_{OC} as a function of intensity on logarithmic scale, the intensity regime that is affected by leakage was predicted to have a slope β^{-1} according to Eq. (3.18), while the point of deflection can be used as a criterion to verify whether the V_{OC} is affected by leakage at a specific intensity.⁸ In Figure 25, the V_{OC} is plotted on logarithmic scale as a function of intensity. The measurements where V_{OC} is found to be affected by leakage are marked with open symbols. As to be expected, the higher the leakage current of a solar cell, the higher the intensity where the curve deflects. The P3HT and T1SL Ω solar cells were found to be strongly affected by leakage current. Their β^{-1} -values were estimated to be 0.96 and 1.02 respectively, from the slope of the red lines in Figure 25.

⁸ Moreover, by measuring the intensity dependence of the short-circuit current (as performed in Chapter 8.2), it can be estimated (by means of interpolation) which current corresponds to the mentioned intensity criterion. This is e.g. useful in case of another light source or another aperture, as one then only has to measure the induced short-circuit current to verify whether V_{OC} is affected by leakage. But throughout this thesis the same light source and aperture are used every time when the solar cells of Figure 24 are used, which makes a criterion for the current not more useful than an intensity criterion.

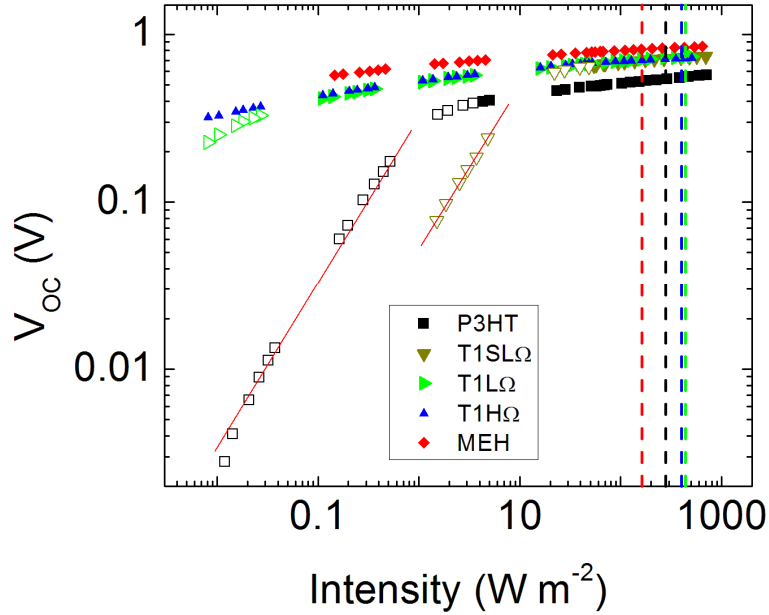


Figure 25: V_{oc} as a function of intensity on logarithmic scale. The open symbols represent the measurement results where V_{oc} is clearly affected by leakage current. The P3HT and T1SL Ω solar cells were found to be strongly affected by leakage current. Their β^{-1} -values were estimated to be 0.96 and 1.02 respectively, from the slope of the red lines. The dashed lines correspond to light conditions that yield similar photocurrent as AM1.5G light (Table 8). The solar cell structures are abbreviated according to Table 1 and Chapter 4.1.

5.2 Determination of S

According to Chapter 3.2, S is defined as ‘the slope in units of V_T for V_{oc} as a function of the natural logarithm of I in an intensity regime ΔI . Several methods are used to determine S , which are described in detail in Chapter 3.2. The methods take different values of ΔI , which is one of the reasons that the results for S differ. For each method S is determined for the five organic solar cells of Chapter 4. In Chapter 6 the best methods are compared to each other.

5.2.1 Method I: S from linear fitting

Similar to Figure 6 the results of Figure 25 can be plotted on a semi-logarithmic scale in order to estimate an average value for S from a linear fit according to Eq. (3.2). This results in Figure 26, where the measurement points where the leakage current affects V_{oc} are omitted.

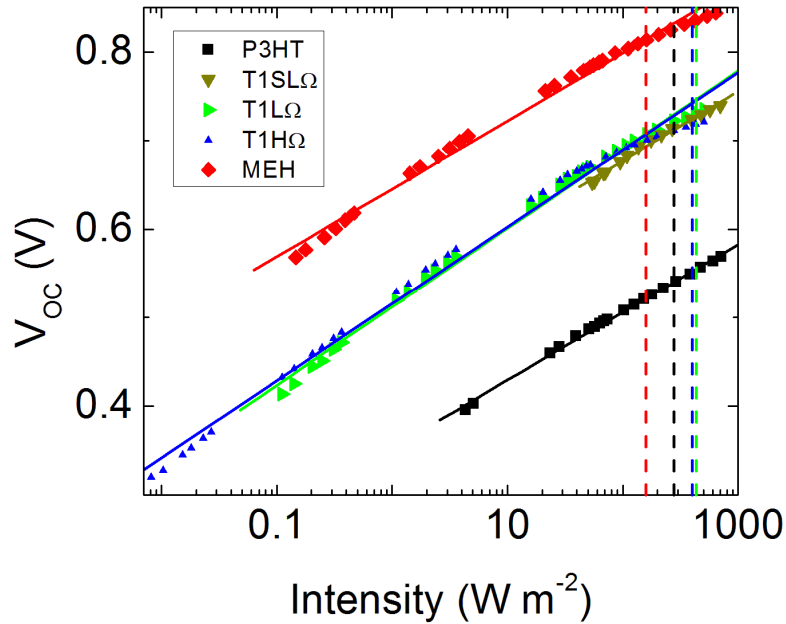


Figure 26: Intensity dependence of V_{OC} on semi-logarithmic scale. Assuming a linear dependence (fitted lines) yields the tabulated S -values in Table 9, which is the slope in units of V_T . The dashed lines correspond to light conditions that yield similar photocurrent as AM1.5G light (Table 8). The solar cell structures are abbreviated according to Table 1 and Chapter 4.1.

The values obtained for S are tabulated in Table 9. These values are much larger than unity, which would have been the slope in units of V_T when Köster's equation (2.25) would be applicable.

Table 9: Results for Method I. Values for S when assuming a constant slope. The solar cell structures are abbreviated according to Table 1 and Chapter 4.1.

Solar cell	S
P3HT	1.31
MEH	1.31
T1H Ω	1.49
T1L Ω	1.51
T1SL Ω	1.34

An even more notable fact is that all curves in Figure 26 seem to deflect with increasing intensity. That the values do not lie on a straight line becomes even more clear when considering the relative residue δ , which is the relative difference of an experimental value and the fit. For all solar cells quite smooth curves are obtained (Figure 27), which strongly illustrates that the deviation from the linear fit in Figure 26 is not due to measurement errors but has a physical origin. The remaining conclusion to be drawn is that S decreases with increasing intensity, which makes the values of Table 9 in fact useless.

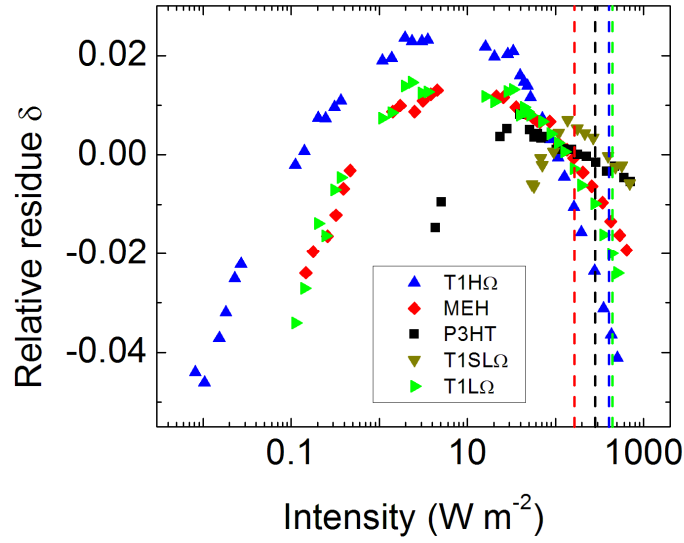


Figure 27: Relative residue δ as a function of intensity. The dashed lines correspond to light conditions that yield similar photocurrent as AM1.5G light (Table 8). The solar cell structures are abbreviated according to Table 1 and Chapter 4.1.

5.2.2 Method II: S from differentiation

Using Eq. (3.5), S can be determined from differentiation of the measurement results of Figure 26. This results in Figure 28, where S is plotted on semi-logarithmic scale as a function of intensity.

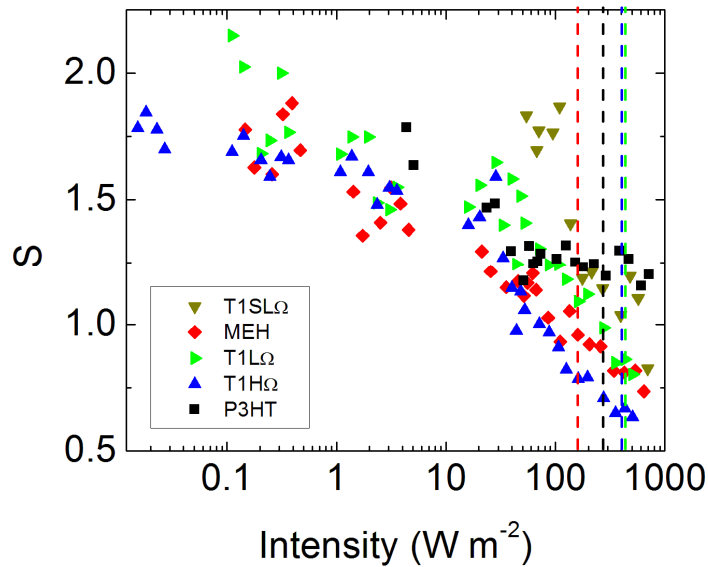


Figure 28: Results for Method II. S on semi-logarithmic scale determined from Eq. (3.5) applied to Figure 26. The measurement points where V_{oc} is clearly affected by leakage current are omitted from this plot. The dashed lines correspond to light conditions that yield similar photocurrent as AM1.5G light (Table 8). The solar cell structures are abbreviated according to Table 1 and Chapter 4.1.

The results for S in Figure 28 are not very accurate. However, for most solar cells it is clear that S decreases for increasing intensity, which is consistent with the trends of the relative residues in Figure 27. It will be determined in Chapter 5.7 that a small intensity difference between two measurement points induces a large error in S . Indeed, for method III the accuracy increases due to the use of a larger intensity difference for determination of S .

It was already determined from Figure 25 that the P3HT and T1SL Ω solar cells suffer significantly from leakage current. The measurement points (omitted from Figure 28) where V_{OC} is affected by leakage are included in the logarithmic plot of Figure 29(a). Now the intensity regime that is affected by leakage is predicted to have a slope β^{-1} according to Eq. (3.21). For the P3HT and T1SL Ω solar cells the values of the slope of the red lines were estimated to be 0.87 and 0.95 respectively. Apparently, determining S from differentiation is not accurate enough to reproduce the β^{-1} -values from Figure 25. The characteristic peaking of S for the intensity regime where V_{OC} is affected by leakage, is caused by the large drop of V_{OC} for decreasing intensity in Figure 29(b), which is the semi-logarithmic plot of Figure 25.

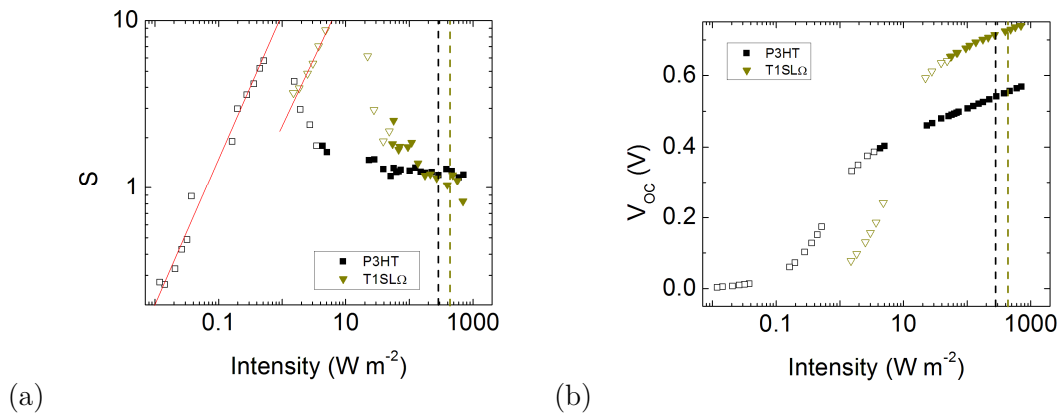


Figure 29: Measurement results for the P3HT and T1SL Ω solar cells. The open symbols represent the measurement results where V_{OC} is clearly affected by leakage current. The dashed lines correspond to light conditions that yield similar photocurrent as AM1.5G light (Table 8). (a) S on logarithmic scale determined from Eq. (3.5) applied to Figure 26. The slopes of the red lines were estimated to be 0.87 and 0.95 for P3HT and T1SL Ω respectively. (b) V_{OC} as a function of intensity on semi-logarithmic scale, from which the values of S are determined. The solar cell structures are abbreviated according to Table 1 and Chapter 4.1.

5.2.3 Method III: Selection via $\Delta I/I > 1$

In this method S is determined according to Eq. (3.8) where several pairs of measurement points are selected from Figure 26, where each pair of measurement points satisfies $1 < \Delta I/I < 2$. Using this method, Figure 30 is obtained where S is plotted as a function of intensity on semi-logarithmic scale. The measurement points are found to be less scattered compared to Figure 28. The trend of decreasing S for increasing intensity has become even more clear, except for the case of the P3HT solar cell. The results of Figure 30 will be compared to other methods in Chapter 6.

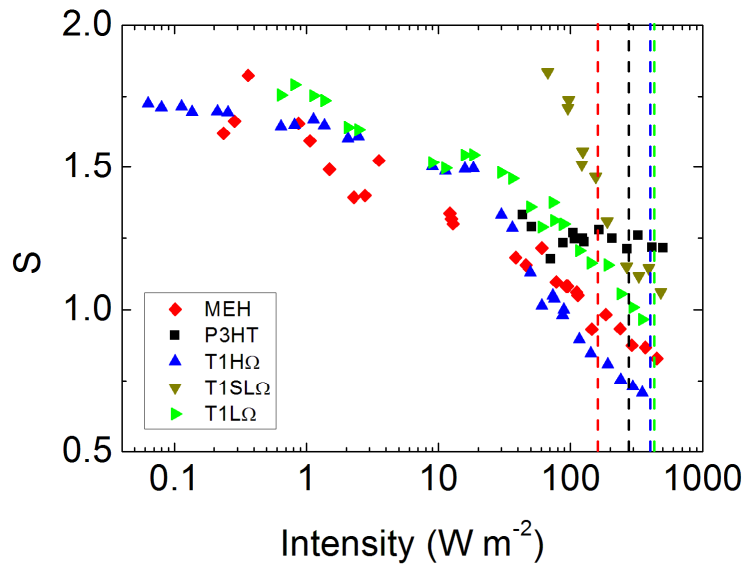


Figure 30: Results for Method III. S as a function of intensity on semi-logarithmic scale. The dashed lines correspond to light conditions that yield similar photocurrent as AM1.5G light (Table 8). The solar cell structures are abbreviated according to Table 1 and Chapter 4.1.

5.2.4 Method IV: Polynomial fits

The results of this method are given in Chapter 6 where the method is compared to the others. When the method is applied to the T1H Ω solar cell, one obtains Figure 31 from Eq. (3.12), where (a) shows the results when fitting all data points of Figure 26, and (b) when fitting only the intensity regime with $10 < I < 1000 \text{ W m}^{-2}$. For comparison the measurement results of Method III are displayed as well. In both cases a fourth order polynomial provided the best correlation for the results of S between Method III and IV.

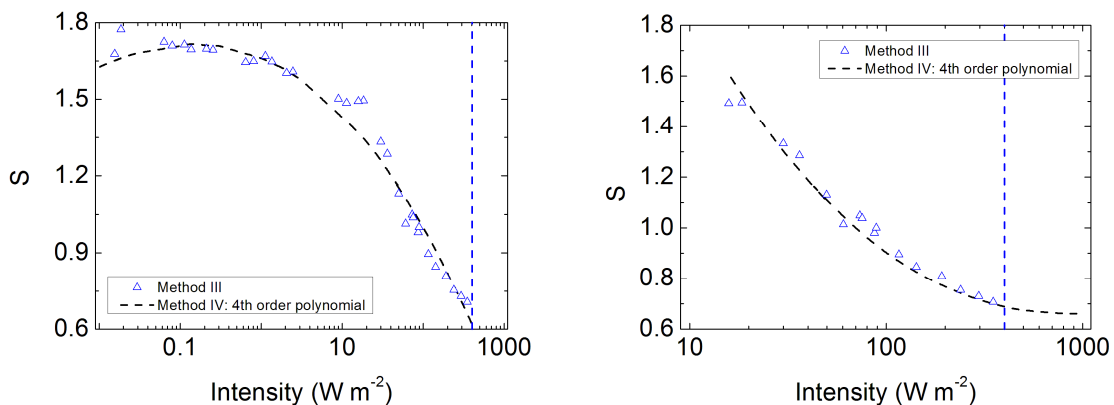


Figure 31: Results for Method IV applied to the measurement results in Figure 26 for the T1H Ω solar cell. (a) Results when fitting all data points. (b) Results when fitting only the intensity regime with $10 < I < 1000 \text{ W m}^{-2}$. The vertical dashed line corresponds to light conditions that yield similar photocurrent as AM1.5G light (Table 8).

5.2.5 Method V: Using a beam splitter

One way to obtain a more or less constant ratio of $\Delta I/I$ experimentally is displayed in Figure 32, which is an extension of the experimental setup in Chapter 5.1. The beam reflected from the beam splitter has intensity I , while the transmitted beam has intensity ΔI . When the beam stop is placed in position, the solar cell is illuminated with an intensity I . When the beam stop is removed, the solar cell is illuminated with an intensity $I+\Delta I$, where a mirror is used to focus the transmitted beam onto the solar cell. The value of $\Delta I/I$ is mainly determined by the transmittance of the beam splitter. However, the ratio $\Delta I/I$ was found not to be exactly constant for the different filter wheel combinations. Nevertheless, the ratio was found to be repeatable for each particular filter combination. This means that when using a particular combination of two ND-filters for measuring $V_{oc}(I)$ and $V_{oc}(I+\Delta I)$, the ratio of $\Delta I/I$ as determined with the silicon photodiode for these two ND-filters can be used for determination of S .

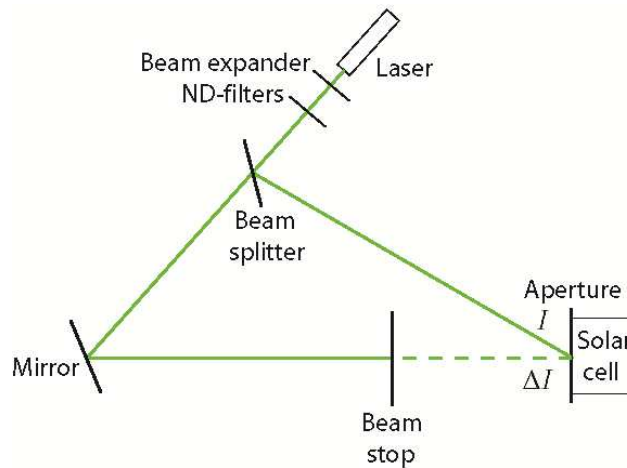


Figure 32: Experimental setup which provides a more or less constant ratio of $\Delta I/I$ regardless the size of I . When the beam stop is placed in position, the solar cell is illuminated with an intensity I . When the beam stop is removed, the solar cell is illuminated with an intensity $I+\Delta I$.

In method III, S was determined from taking two measurement points of Figure 26. Instead, each pair of intensities I and $I+\Delta I$ is now obtained from a single laser beam which splits into two separate beams due to the beam splitter. S is determined according to Eq. (3.8). This method is only applied to the T1H Ω solar cell. Plotting S as a function of $I+\Delta I/2$ provides Figure 33. This method will be compared to other methods in Chapter 6 from which it is concluded that this method is very accurate. If one is interested to determine S for low intensities, Method V might even be the preferable method, because ΔV_{oc} can be determined manually.

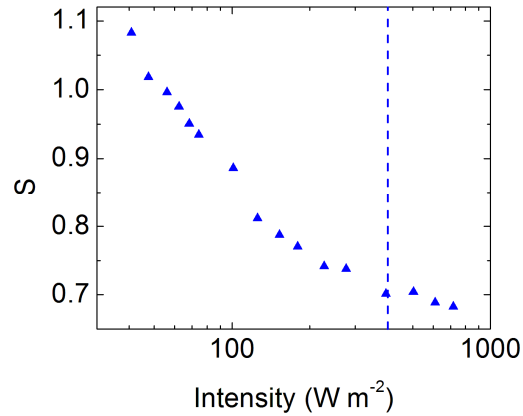


Figure 33: S as a function of intensity as determined according to Method IV for the T1H Ω solar cell. The dashed line corresponds to light conditions that yield similar photocurrent as AM1.5G light (Table 8).

5.3 The steady-state differential voltage technique

As mentioned in Chapter 3.2.7, the sixth method to determine S is a new measuring method defined as the steady-state differential voltage (SSDV) technique. This technique is in many ways analogous to the steady-state differential current (SSDC) technique,^[9] which is performed in Chapter 8.2.3. The SSDC technique studies the light intensity dependence of the short-circuit current density by measuring the differential short-circuit current density ΔJ_{SC} induced by a modulation in light intensity ΔI in the presence of a background light intensity I . This is all performed under short-circuit conditions. By contrast, the SSDV technique studies the light intensity dependence of the open-circuit voltage based on measuring the differential open-circuit voltage ΔV_{OC} induced by a modulation in light intensity ΔI in the presence of a background light intensity I . This is all performed under open-circuit conditions.

5.3.1 Experimental setup

The experimental setup of the SSDV technique (Figure 34) is an extension of the setup used in Chapter 5.2.5,⁹ which was an extension of the one introduced in Chapter 5.1. The same laser, ND-filters, beam expander, beam-splitter, mirror and aperture are used here. The light reflected from the beamsplitter (I) will be referred to as the background light. The transmitted light (ΔI) will be referred to as the superimposed light or the modulation. A chopper is used instead of the beam stop in Figure 32. Before reaching the solar cell, the superimposed light ΔI meets the chopper, which simply blocks the light half of the time with a to be set frequency. A lock-in amplifier, which is a phase-sensitive detector, picks up the differential voltage ΔV_{OC} induced by the superimposed light ΔI . The set of ND-filters is used to modify the light intensity.

⁹ See Chapter 8.3 for a detailed description about the SSDV technique.

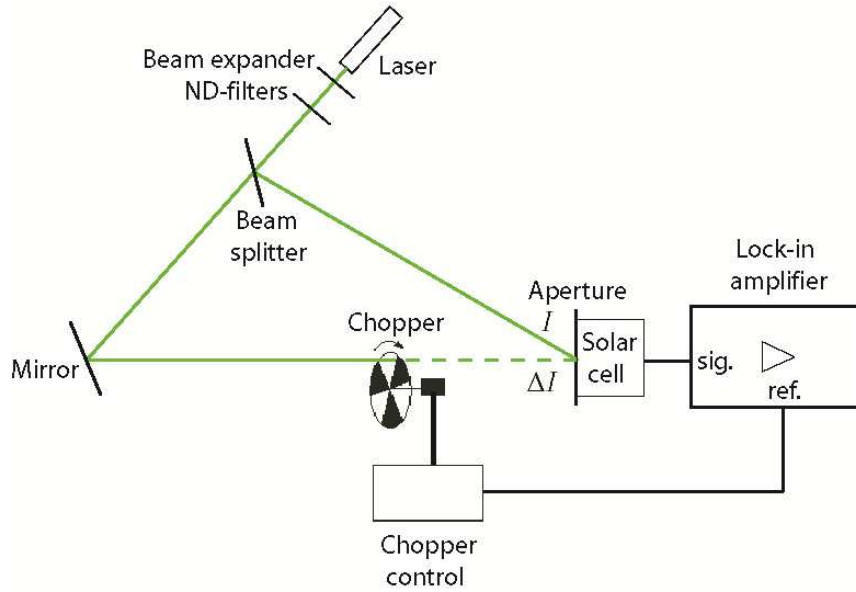


Figure 34: Experimental setup of the SSDV technique. The lock-in amplifier displays a value from which ΔV_{OC} is obtained according to Eq. (8.6). From measuring the induced short-circuit current in a silicon photodiode, the ratio $\Delta I/I$ is obtained. Substituting these values into Eq. (3.8) yields S . In reality the angle between beams I and ΔI is much smaller than depicted; the beam splitter and mirror are positioned close together, far from the aperture.

With the solar cell being alternately illuminated with a light intensity I either $I+\Delta I$, the difference in V_{OC} between these two signals (Eq. (3.13)) is described by Eq. (3.6), which allows to calculate S according to Eq. (3.8). Again the short-circuit current of the silicon photodiode was used to measure the intensities.

The beam splitter and mirror are placed such that the centers of the beams are a distance $D = 3$ cm apart at a distance $L = 1.8$ m from the aperture. The distance from the aperture to the solar cell is $l = 1.8 \pm 0.2$ cm, which yields $d = 0.3$ mm for the distance between the centers of the beams at the solar cell according to Eq. (8.19). With the diameter of the aperture being 1.77 ± 0.03 mm, Eq. (8.18) yields a beam overlap of 85%. It is assumed that the measurement results will not deviate much from a situation with 100% beam overlap. This assumption is supported by the measurement results in chapter 5.6.2. There, almost the same results are obtained for 85% and 100% beam overlap when S is determined for a silicon photodiode.

To verify that the measured ΔV_{OC} corresponds to steady-state conditions, the chopper frequency is varied from 20 to 200 Hz. In line with the predictions of Chapter 3.2.7, for too low intensities it was found that steady-state conditions were not satisfied as the display value of the lock-in amplifier was not constant for different frequencies. Accordingly, measuring the voltage oscillation with an oscilloscope shows that the oscillation, being subject to the charge carrier lifetime τ , ultimately results in a saw-tooth like behavior for extremely low intensities.

5.3.2 SSDV measurement results

The measurement results of the SSDV technique are shown in Figure 35. No change in signal was observed for these measurements when the chopper frequency was varied from 20 to 200 Hz. The chopper was set to 30 Hz afterwards. Clearly, for all solar cells the value of S decreases

with increasing intensity. The scatter of the data points is much less than for Method II and III, where S was determined from differentiation. In Chapter 6 the results are plotted together with the results of Method III-V, which will be discussed in Chapter 6.

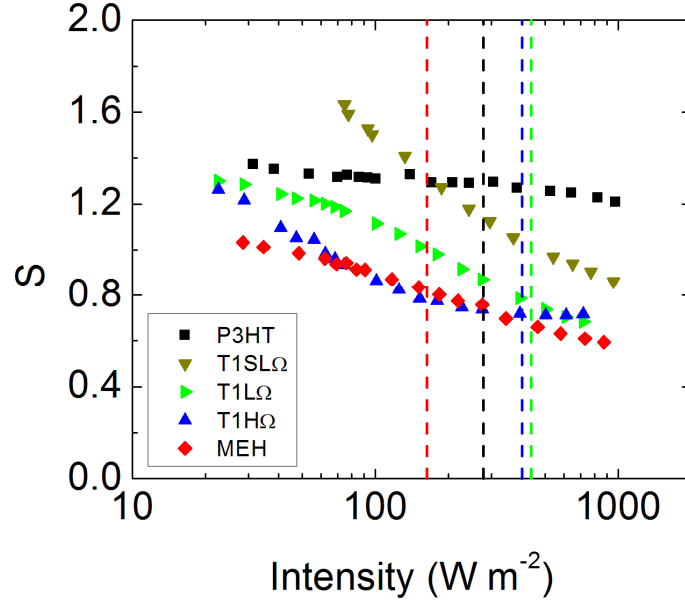


Figure 35: S as a function of intensity as determined with the SSDV technique. The dashed lines correspond to light conditions that yield similar photocurrent as AM1.5G light (Table 8). The solar cell structures are abbreviated according to Table 1 and Chapter 4.1.

5.4 The modified p - n junction based model

The main reason for using the modified p - n junction based model is to point out measurement artefacts. Two artefacts are studied with the model. The first is the influence of the leakage current, which was investigated in Chapter 3.4 by introducing the shunt resistance R_{SH} . Chapter 5.4.1 follows the same procedure for the solar cells introduced in Chapter 4 to understand the artefacts related to leakage current of the measurements in Chapter 5. The second artefact is the influence of the input impedance Z of the measuring device that measures the open-circuit voltage. In Chapter 5.4.2 the model is used to determine whether open-circuit conditions are satisfied depending on the value of Z .

5.4.1 Reproducing the experimental results

In order to verify whether the experimental results are reasonable, it is useful to compare it to the model results obtained with the modified p - n junction based model (Chapter 3.4). By obtaining R_{SH} from the dark current (similar to Figure 12) and fitting (similar to Figure 13) the i - V curves under illumination (Figure 24), Figure 36 is produced (similar to Figure 15(b)). The intensity is plotted in number of Sun-equivalents, determined from the ratio of i_{PH} with respect to the 1 Sun-equivalent case. Figure 36 shows the same trend as Figure 25.

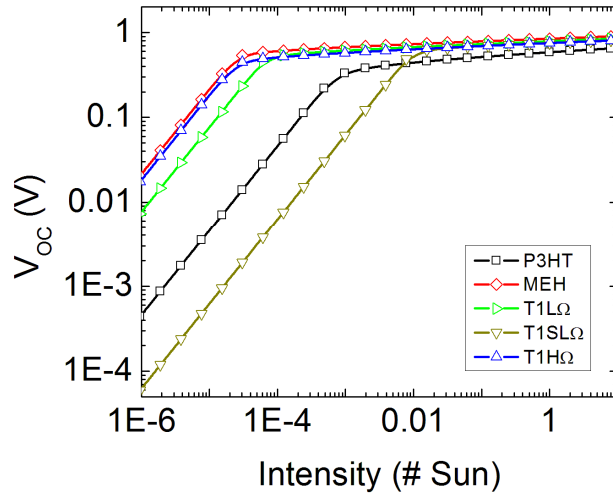


Figure 36: Model results for V_{oc} as a function of intensity for the solar cells used for the experiments of Chapter 5. The solar cell structures are abbreviated according to Table 1 and Chapter 4.1.

To compare the measurement results for S with the model, Eq. (3.5) has been used to obtain Figure 37, where S is plotted as a function of I on logarithmic scale. The value of S approaches the predefined value of n in Eq. (3.23) for the high intensities. Clearly, the model is not able to explain the behavior of S in Figure 35. For low intensities the model results are quite comparable to Figure 29(a), in the sense that a peak is obtained together with a constant slope for the regime where the leakage current affects the results.

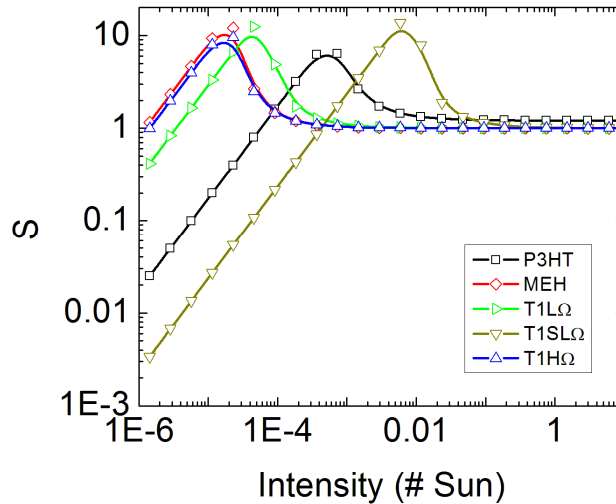


Figure 37: Model results for S as a function of intensity for the solar cells used for the experiments of Chapter 5. The solar cell structures are abbreviated according to Table 1 and Chapter 4.1.

Note that in order to compare these model results quantitatively to the experimental results, one should take into account Table 8. One should then calculate the laser light intensities to

number of Sun-equivalents by dividing it to the intensity which induced the same J_{SC} as obtained with AM1.5G light. However, the use of the Solar Simulator is not the only important difference compared to the experiments of Chapter 5. In the former case the whole area is illuminated, while in the latter only a part of it. Nevertheless, the trend of the graphs at low intensities is the same.

5.4.2 A criterion test for open circuit conditions

In order to measure V_{OC} , ideally there should be an infinite impedance in the electrical network, such that the current would be zero. Experimentally this cannot be obtained due to the fact that the input impedance Z of a measuring device is finite. This means that the measured “ V_{OC} ” is an approximation – quotation marks are used to indicate this – of the real V_{OC} . A Keithley 2410 SourceMeter has an input impedance of more than 10 G Ω . The lock-in amplifier has an input impedance of 10 M Ω . For both cases the current through the circuit will always be non-zero, which means that when measuring under open-circuit conditions the voltage on the solar cell becomes somewhat smaller than V_{OC} . Depending on the intensity of illumination, this deviation might be unacceptable for assuming open-circuit conditions. To illustrate how such a finite input impedance Z might affect V_{OC} and S , the model will first be applied to the P3HT-L Ω solar cell of Figure 4. The bias (V_a), current (i_L) and input impedance Z should satisfy both Ohm’s law and the i - V curve. Starting from the real V_{OC} , the ratio V_a/i_L at a series of points at the i - V curve is varied, until the ratio is close enough to Z , as performed in Chapter 8.7.2. For each Z a series of “ V_{OC} ”-values is obtained as a function of intensity, as plotted in Figure 38(a). Figure 38(b) shows the relative error, i.e. $|V_{OC} - \text{“}V_{OC}\text{”}|/V_{OC}$.

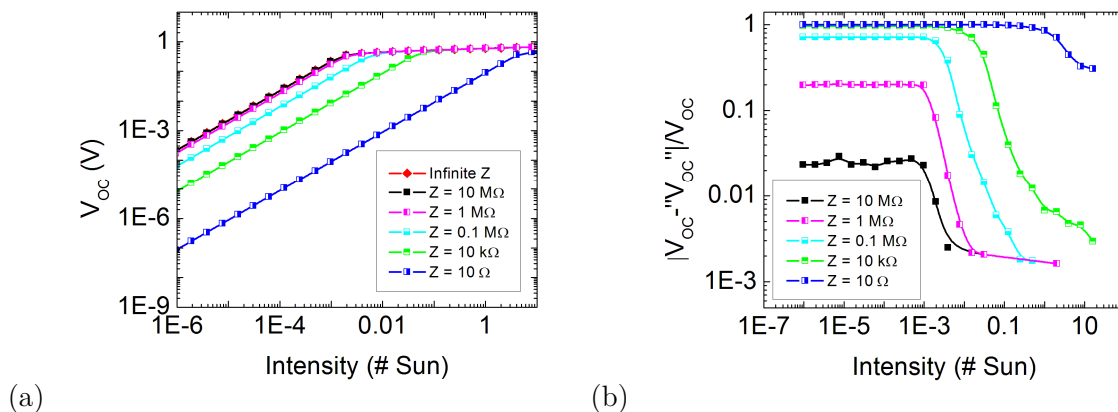


Figure 38: Model results with the i - V curve of Figure 4 as input. For different input impedances Z a logarithmic plot is obtained for (a) V_{OC} and (b) the relative error in V_{OC} as a function of intensity in number of Sun-equivalents.

A reasonable criterion for “ V_{OC} ” is at most 1% deviation from the real V_{OC} . This means that the relative error in V_{OC} should be at most 0.01. Intensities which induce a V_{OC} smaller than this criterion should thus be disregarded. What is displayed as intensity in Figure 38 is actually the ratio of i_{PH} with respect to the 1 Sun-equivalent case, similar to Figure 15. In the model it was also assumed that $i_{SC} = i_{PH}$, which means that the model directly supplies a criterion for

the short-circuit current. Therefore it is convenient to set up for each solar cell a criterion for the induced short-circuit current when measuring under short-conditions. A light intensity that induces a smaller short-circuit current in the solar cell than this criterion should then not be used for measuring under open-circuit conditions.

Using the i - V curves from Figure 24 as input for the model, Figure 39 has been obtained, showing the relative error in V_{OC} as a function of i_{SC} . For the input impedance the value of the lock-in amplifier has been used, i.e. $Z = 10 \text{ M}\Omega$.

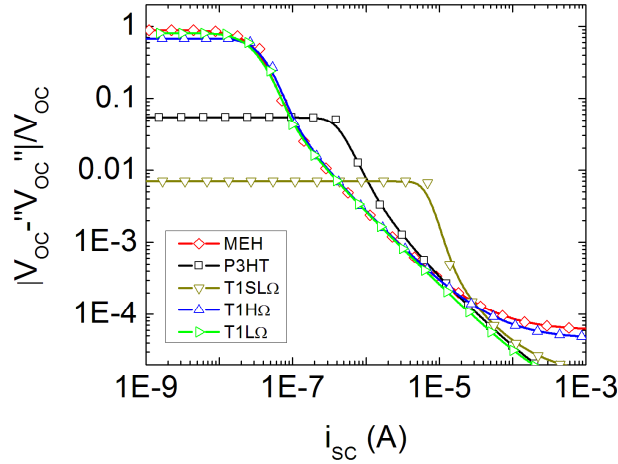


Figure 39: Model results for the relative error in V_{OC} as a function of the short-circuit current for the solar cells used for the experiments of Chapter 5. For the input impedance the value of the lock-in amplifier has been used, i.e. $Z = 10 \text{ M}\Omega$. The solar cell structures are abbreviated according to Table 1 and Chapter 4.1.

The criterion for the i_{SC} can be obtained from interpolation of these results at the criterion for the relative error in V_{OC} , i.e. 0.01.

To determine a similar criterion for S one should take into account that the SSDV-technique approximates both V_{OC} induced by I and $I + \Delta I$ in order to produce “ ΔV_{OC} ”, i.e.

$$\Delta V_{OC} = V_{OC}(I + \Delta I) - V_{OC}(I) . \quad (5.1)$$

Consequently, what is assumed to represent the real S is also an approximation:

$$S = \frac{\Delta V_{OC}}{V_T \ln\left(1 + \frac{\Delta I}{I}\right)} , \quad (5.2)$$

The relative error in S , i.e. $|S - S^0|/S$, is plotted in Figure 40, where again the i - V curves from Figure 24 are used as input for the model together with $Z = 10 \text{ M}\Omega$. The criterion for the i_{SC} can be obtained from interpolation of these results at the criterion for the relative error in S , i.e. 0.01.

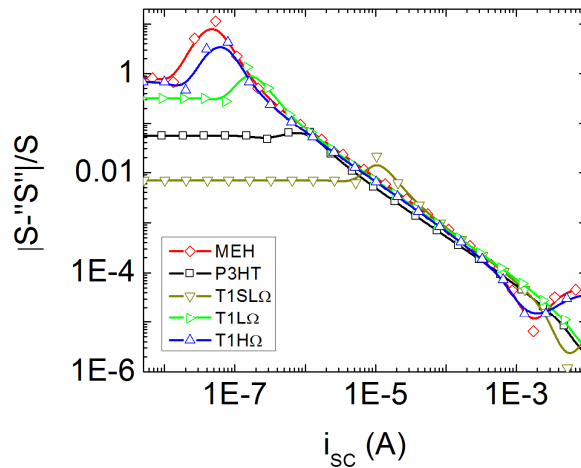


Figure 40: Model results for the relative error in S as a function of the short-circuit current for the solar cells used for the experiments of Chapter 5. For the input impedance the value of the lock-in amplifier has been used, i.e. $Z = 10 \text{ M}\Omega$. The solar cell structures are abbreviated according to Table 1 and Chapter 4.1.

In order to verify whether the measurement results of S satisfy the criterion for measuring under open-circuit conditions, for all solar cells i_{sc} has to be measured as a function of intensity. By interpolating these results (Chapter 8.2.2),¹⁰ one obtains a criterion for the intensity of the light source. It is therefore recommended to measure both V_{OC} and i_{sc} as a function of intensity. The results are tabulated in Table 10 where I applies to the laser. It can be seen that all measurements of Figure 35 satisfy the criterion for measuring under open circuit conditions.

Table 10: Criteria for measuring under open-circuit conditions in case of the SSDV-measurement. The solar cell structures are abbreviated according to Table 1 and Chapter 4.1.

Solar cell	Criterion for i_{sc} (μA)	Criterion for I (W m^{-2})
P3HT	3.55	5.46
MEH	5.81	17.8
T1H Ω	4.91	7.78
T1L Ω	5.19	8.24
T1SL Ω	12.1	19.6

5.5 Measurement of V_{OC} with Solar Simulator

Figure 41 shows the V_{OC} as a function of intensity as measured for the (a) MEH and (b) T1H Ω solar cells. The black data points are obtained with the Solar Simulator. The colored data points are obtained with the laser (Figure 26). The decrease of S for increasing intensity is not visible for the data obtained with the Solar Simulator. The fact that the data do not match has different reasons.

¹⁰ It is assumed that the measurement results for T1H Ω are also applicable to T1L Ω and T1SL Ω .

One reason is that the Solar Simulator produces a spectrum of light which induces a difference compared to the laser measurements, because the amount of absorption depends on the wavelength of the light (Chapter 8.1). For this one should take into account the vertical lines which correspond to light conditions that yield similar photocurrent as AM1.5G light (Table 8). For comparison, all data obtained with the laser should be shifted towards the right with the distance between the vertical line and the value 1000 W m^{-2} .

However, the fact that the laser only partially illuminates the solar cell due to the aperture affects the V_{OC} as well. The data from the Solar Simulator are obtained with the whole area (16 mm^2) being illuminated, while for the case of the laser an aperture with diameter 1.77 mm was used (2.5 mm^2). In the case of the laser the illuminated area is thus about 6.4 times as small as the total area. In Chapter 6.2 it is argued that the data obtained with the laser should therefore be shifted towards the left with 0.8 units.

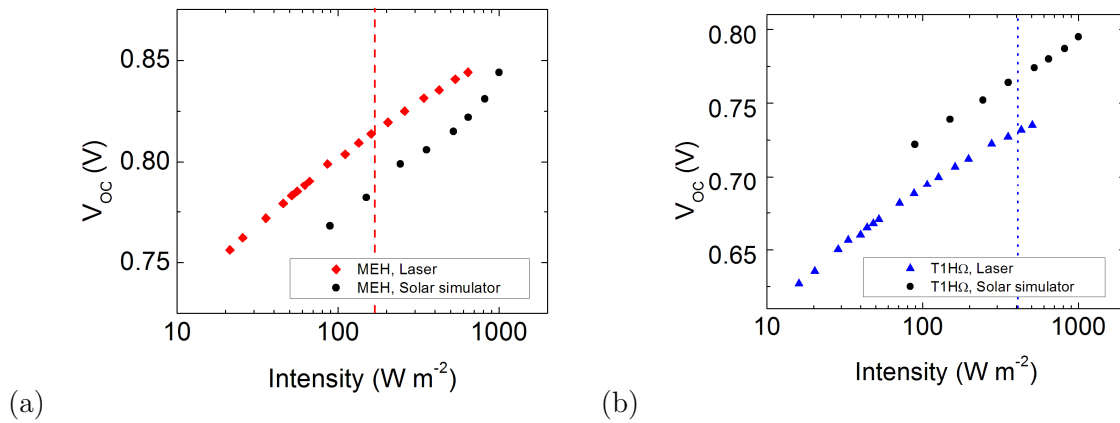


Figure 41: V_{OC} as a function of intensity as measured for the (a) MEH and (b) T1H Ω solar cells. The vertical lines correspond to light conditions that yield similar photocurrent as AM1.5G light (Table 8). The solar cell structures are abbreviated according to Table 1 and Chapter 4.1.

5.6 Silicon photodiode

5.6.1 Intensity dependence of V_{OC}

Although this research is focused on organic BHJ solar cells, it has been discovered that the non-linearity of the V_{OC} plotted as a function of the natural logarithm of intensity does not only play a role for organic solar cells. Measurements with a silicon photodiode induced similar results. A silicon photodiode (Model No: 818-SL; Serial No: 14906) different to the original one was used to determine the intensity dependence of V_{OC} .¹¹ Figure 42(a) shows the measurement

¹¹ At the final stage of this research project the original silicon photodiode (Model No: 818-SL; Serial No: 15680) got damaged. The SSDV technique was applied to that photodiode beforehand as well, but the results, which were similar to Figure 42, are omitted. Note that it was assumed that the same responsivity was applicable to the other photodiode.

results of V_{OC} as a function of intensity, for which the measurement setup of Chapter 5.1 has been used. For the intensities below 0.1 W m^{-2} , the V_{OC} is affected by leakage current. For large intensities, S , i.e. the slope in units of V_T , is found to decrease as a function of intensity, as can be seen in Figure 42(b). The red data points are obtained from the SSDV technique (Chapter 5.3). The blue data points are obtained from applying Eq. (3.5) to Figure 42(a) according to Method II (Chapter 3.2.2).

It is also determined in Chapter 5.6.2 that S strongly depends on the extent of overlap of the two laser beams in case of an SSDV measurement. However, the fact that the decrease of S for increasing intensity is also measured with Method II – which requires only the use of one laser beam – confirms that the extent of beam overlap is not the origin of the decrease of S .

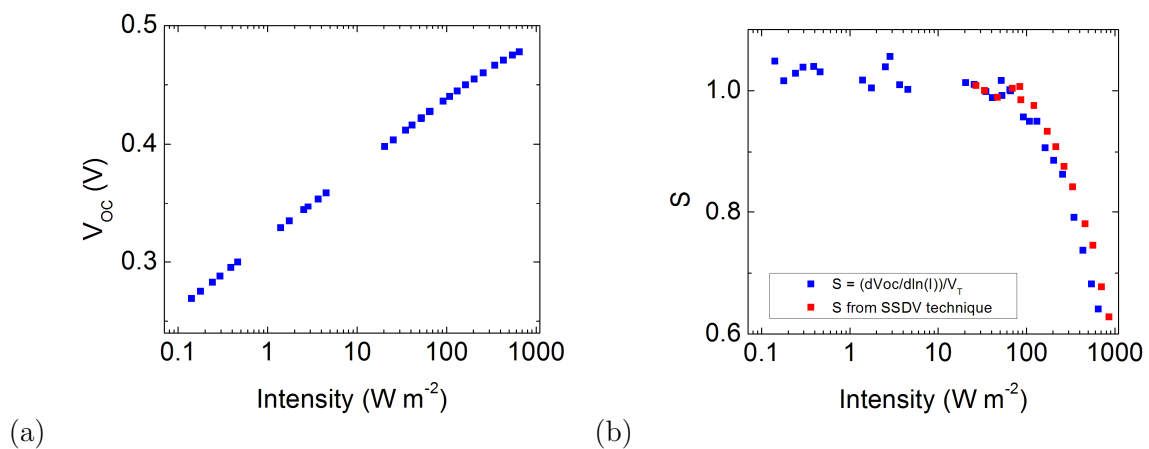


Figure 42: Measurement results for the silicon photodiode (Newport 818-SL, Serial No: 14906). (a) V_{OC} as a function of intensity. (b) S as a function of intensity, as determined from the SSDV technique and from differentiation of the results of (a) according to Eq. (3.5).

5.6.2 Dependence on beam overlap

Because solar cells with an area larger than the aperture size have been used, the two laser beams (I and ΔI in Figure 34) do not fully overlap for an SSDV experiment. This dependence of S on the extent of beam overlap is investigated here experimentally. The distance l from the aperture to the test cell, which is the silicon photodiode in this case, is varied which causes the extent of beam overlap to vary as described in Chapter 8.5. The beam splitter and mirror are placed such that the centers of the beams are a distance $D = 3 \text{ cm}$ apart at a distance $L = 1.8 \text{ m}$ from the aperture. The diameter of the circular aperture has been changed to $2.59 \pm 0.03 \text{ mm}$.

Note that for 0% overlap the illuminated area on the solar cell is twice as large as compared to 100% overlap. Therefore, the intensity becomes in principle twice as small. However, intensity is defined here as the total power on the solar cell divided by the area of the aperture, which makes the intensity independent of the extent of beam overlap. To verify that no light falls outside the solar cell, the current induced under short-circuit conditions has been measured as

well. This current was constant when the extent of beam overlap was varied, confirming that the light intensity stayed constant.

Figure 43 shows two series of SSDV measurements where S is plotted as a function of intensity. In one series (red data points) the laser beams have no overlap at all, while in the other case (blue data points) they have 76% overlap, as was determined from Eq. (8.18). The effect of decreasing S for increasing intensity is much stronger in the latter case.

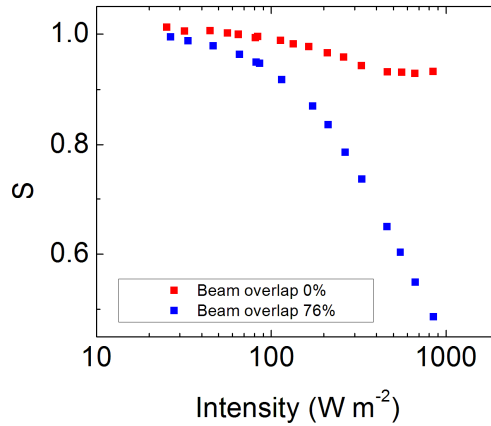


Figure 43: Two series of SSDV measurements performed with the silicon photodiode (Newport 818-SL, Serial No: 14906). For the red data points the laser beams have no overlap at all, while for the blue data points there is 76% overlap, as determined from Eq. (8.18).

Figure 44 shows for the SSDV technique how S changes when the extent of beam overlap is varied, while the intensity is kept constant at 850 W m^{-2} . It is found that the smaller the extent of beam overlap, the larger S becomes. For a beam overlap of more than 80% the value of S is more or less constant. Therefore it is assumed that the measurements of Chapter 5.3, where the extent of beam overlap was 85%, are a good representation of the case where the beams would fully overlap.

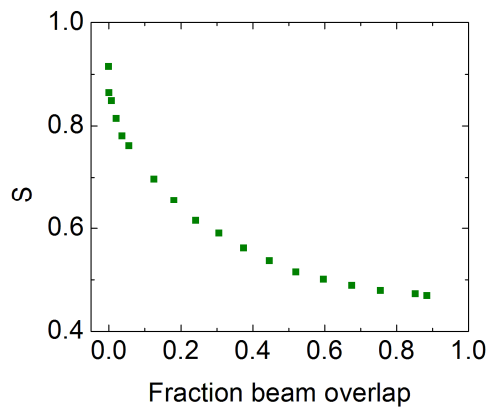


Figure 44: The dependence of S on the extent of overlap of the two beams in a SSDV measurement as performed for the silicon photodiode (Newport 818-SL, Serial No: 14906). The intensity is 850 W m^{-2} for all data points.

5.7 Error analysis

In general, for a function $f(x,y,\dots)$ the standard deviation is given by

$$\sigma_f^2 = \left(\frac{df}{dx}\right)^2 \sigma_x^2 + \left(\frac{df}{dy}\right)^2 \sigma_y^2 + \dots \quad (5.3)$$

Applied to Eq. (3.8) this yields for the standard deviation in S

$$\sigma_s^2 = \left(\frac{dS}{d\Delta V_{OC}}\right)^2 \sigma_{\Delta V_{OC}}^2 + \left(\frac{dS}{dV_T}\right)^2 \sigma_{V_T}^2 + \left(\frac{dS}{d\frac{\Delta I}{I}}\right)^2 \sigma_{\frac{\Delta I}{I}}^2. \quad (5.4)$$

The measurement results of the SSDV technique (Chapter 5.3.2) showed the least scatter of the six methods. Therefore an estimate for σ_s is first determined for this ideal case.

The accuracy for measuring V_{OC} is found to be limited by a standard deviation of $\sigma_{V_{OC}} = \pm 0.2$ mV. For the SSDV measurement ΔV_{OC} is defined in Eq. (3.13), which yields for its standard deviation $\sigma_{\Delta V_{OC}} = \pm 0.4$ mV. According to Eq. (3.6), ΔV_{OC} depends linearly on the natural logarithm of $1+\Delta I/I$. For small values of $\Delta I/I$, ΔV_{OC} might become so small that it gets in the order of $\sigma_{\Delta V_{OC}}$.

To determine the accuracy of $\Delta I/I$ for the case of the SSDV measurement, several series have been performed of measuring the short-circuit current in the silicon photodiode induced by both intensity I and $I+\Delta I$. Taking different ratios of $\Delta I/I$, the largest relative standard deviation, i.e. $\sigma_{\Delta I/I}$ relative to $\Delta I/I$, was 2% which is used as an upper limit.

A thermo couple (Kane-May KM330) was used to estimate that the temperature increase of the solar cells due to laser light illumination is at most about 3 K (Chapter 8.6). With the measurements of S being performed at room temperature, the relative standard deviation of V_T , i.e. σ_{V_T} relative to V_T , therefore amounts about 1%.

Substituting these values into Eq. (5.4) yields Figure 45. The three terms of Eq. (5.4) are labelled as T₁, T₂ and T₃ respectively in Figure 45(a), which shows that the first term becomes very large for small values of $\Delta I/I$. This induces the value of σ_s to strongly increase with a decreasing ratio of $\Delta I/I$, as plotted in Figure 45(b). Hence, the value of $\Delta I/I$ should not be much smaller than 1. In the SSDV measurements of Chapter 5.3 the ratio $\Delta I/I$ was about 0.6. From Figure 45(b) it can be seen that this corresponds to $\sigma_s \approx 0.025$. This corresponds to a relative error of 2.5% if S equals unity.

Figure 45 also explains the large scatter for the results of Method II (Chapter 5.2.2). In this method S is determined according to Eq. (3.5) from the measurement results of V_{OC} as a function of intensity (Figure 26). Many data points have their intensity difference ΔI being small compared to their intensity I . Such small values of $\Delta I/I$ induce a large standard deviation σ_s according to Figure 45(b).

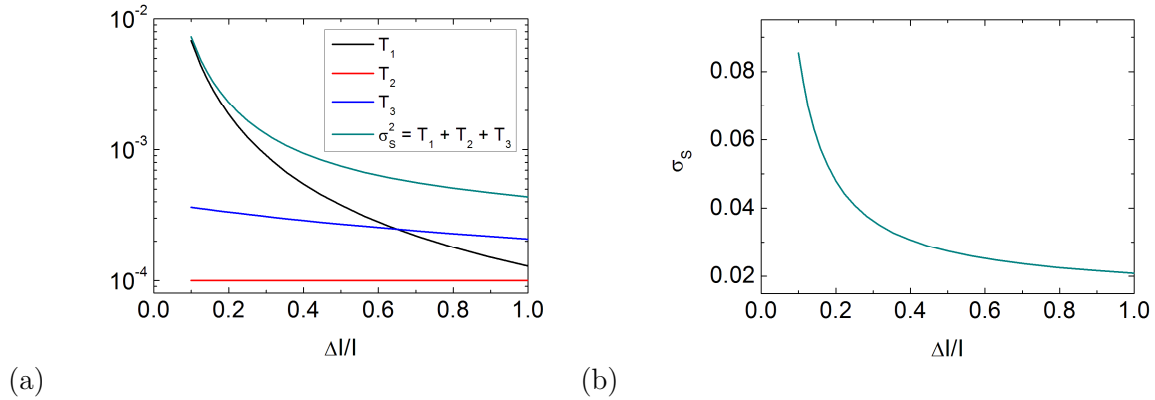


Figure 45: Plot of σ_S^2 as defined in Eq. (5.4) together with its individual terms (a) and σ_S (b). The input parameters are described in the text as estimated for an SSDV measurement.

This observation was the reason to introduce Method III, where pairs of data points of Figure 26 were selected such that $\Delta I/I > 1$. The fact that there is still a quite large amount of scatter in the data points of Method III (Chapter 5.2.3) must thus have another origin. A possible explanation might be the fact that $\Delta I/I$ was not constant. If the ratio $\Delta I/I$ is taken constant instead, the value of $\Delta \ln(I)$ which is defined in Eq. (3.7) becomes constant as well. Any I and its associated $I + \Delta I$ are then equidistant, when plotted on logarithmic scale. In Method V (Chapter 5.2.5) and VI (Chapter 5.3) S is determined from a more or less constant ratio $\Delta I/I$ providing more accurate results.

Perhaps a better explanation of the scatter in Method III is the fact that the laser intensity is not fully constant as a function of time. It even takes about an hour for the laser to heat up. Especially when the measurements are performed within this first hour, the intensities as determined with the silicon photodiode do not accurately represent the intensities during the measurement of the V_{OC} for the organic solar cells. This induces an error in S – as determined from Eq. (3.8), – because the ratio $\Delta I/I$ which is determined with the photodiode, might not accurately represent the ratio of the intensities that have caused ΔV_{OC} in the organic solar cell. Instead, in the case of Method V and VI, the ratio of $\Delta I/I$ is not affected because of the use of one beam passing a beam splitter.

Another advantage of Method V and VI which is expected to improve the accuracy is the fact that the optical elements are not touched for the determination of ΔV_{OC} , while for the other methods the filter wheels are rotated.

6 Discussion

6.1 Comparison of methods to determine S

Six methods have been performed to study the light intensity dependence of the V_{oc} . The results of the methods are compared here where only the intensity regime where V_{oc} is not affected by leakage is taken into account. In order to compare the different methods, the results for Method III and beyond are plotted for each solar cell separately in Figure 46.

Method I assumes a constant S over the entire regime, with S being determined from Eq. (3.2). The results are tabulated in Table 9. From the calculation of the relative residues it could be concluded that S decreases for increasing intensity. This conclusion was drawn for all other conclusions as well.

In Method II, S is determined according to Eq. (3.5). These results (Figure 28) are found not to be very accurate, which could be attributed to ΔI often being too small compared to I .

Selection of data points, as performed in Method III, according to $1 < \Delta I/I < 2$ improved the results for S , – now being determined from Eq. (3.8), – but still quite some scatter remained.

Method IV is based on fitting an n^{th} order polynomial to the experimental results of V_{oc} as a function of the natural logarithm of intensity, with S calculated from Eq. (3.12). The values of n giving the best correlation with Method III is used for the plots of Method IV.

Method V uses a beam splitter to illuminate the solar cells with two laser beams having intensity I and ΔI . The solar cell is alternately illuminated with an intensity I either $I+\Delta I$, inducing open-circuit voltages of $V_{oc}(I)$ and $V_{oc}(I+\Delta I)$ respectively. The difference between these two values, i.e. ΔV_{oc} , is determined manually, from which S is determined according to Eq. (3.8).

By contrast, in Method VI – which is the newly introduced SSDV technique – ΔV_{oc} is obtained from a lock-in amplifier which is used in conjunction with a chopper.

As illustrated in Figure 46, S decreases for increasing intensity consistently for all methods. This disproves the prevailing opinion in literature that the value of S is constant. The value of S becomes even smaller than unity for large intensities (except for P3HT). Method V was found to have an accuracy as good as the SSDV technique. If such accurate results can be obtained for low intensities as well, it might even be the preferable method because Method VI has the disadvantage that steady-state conditions are not always satisfied.

For all solar cells the accuracy of the results of the SSDV technique was better than for Method III. For the T1H Ω (a) and T1SL Ω (c) solar cells the correlation between Methods III-VI is good as well. However, for the T1L Ω (b), P3HT (d) and MEH (e) solar cells the results between Method III and IV on the one hand, and Method VI on the other hand differ quite a lot. Remarkably, for the T1L Ω and MEH measurement the SSDV results lie below while for P3HT those lie above. The reason for this effect is unclear.

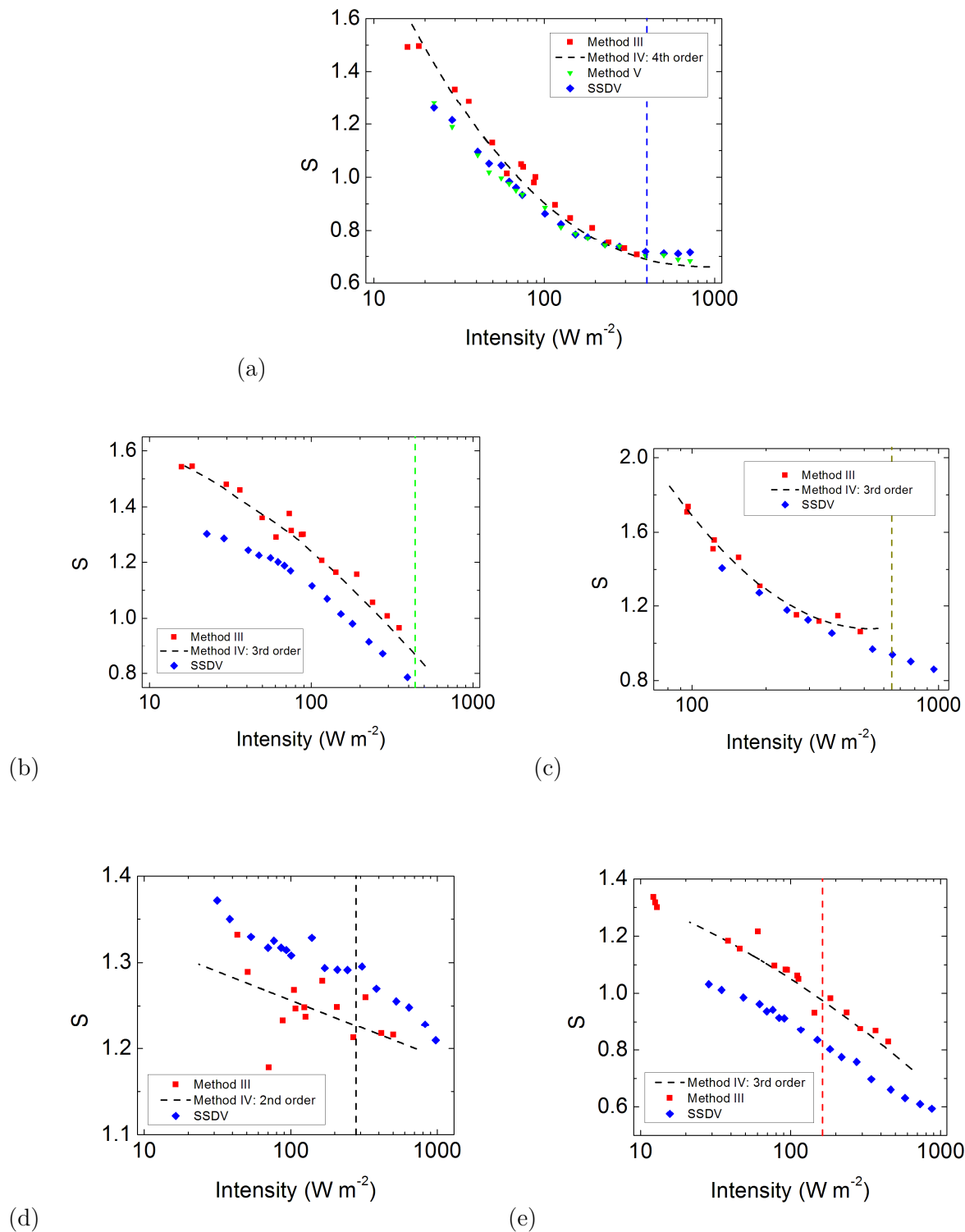


Figure 46: The vertical dashed lines correspond to light conditions that yield similar photocurrent as AM1.5G light (Table 8). The solar cell structures are abbreviated according to Table 1 and Chapter 4.1. (a) Comparison of Methods III, IV, V and VI for determination of S for the T1H Ω solar cell. These results have been displayed before in Figure 30, Figure 31(b), Figure 33 and Figure 35 respectively. (b-e) Comparison of Methods III, IV and VI for determination of S for the (b) T1L Ω , (c) T1SL Ω , (d) P3HT and (e) MEH solar cells. The results for Methods III and VI were displayed before in Figure 30 and Figure 35 respectively.

6.2 Influence of partial illumination

The reasons for using an aperture are described in Chapter 5.1. To reason what the effect is of a partial illumination consider a solar cell being partially illuminated for $1/x$ of its area. The amount of free charges Q will be x times as small with respect to the case of entire illumination. This is analogous to an entire illumination with an x times as small intensity, which corresponds to a reduction of the V_{OC} with $SV_T \ln(x)$, which equals about 60 mV when $x = 10$ and $S = 1$. One might thus conclude that the intensity as determined with the silicon photodiode is overestimated with a factor x , which means that all data points for V_{OC} measured as a function of intensity should be shifted to lower intensities with a factor x . Figure 41 shows the V_{OC} as measured as a function of intensity both with a laser and the Solar Simulator. In the case of the laser the illuminated area is 6.4 times as small as the total area. Hence, the intensities should be divided by 6.4. On logarithmic scale this corresponds to a displacement to the left of $^{10}\log(6.4) \approx 0.8$ units. This might be one of the reasons that the V_{OC} measurements of the laser and the Solar Simulator do not match (Figure 41).

For the case of two beams (Method V and VI) the use of an aperture smaller than the area of the solar cell induces an overlap of less than 100%. To reason what the effect is of such a change of the amount of beam overlap, consider a solar cell illuminated by two laser beams both with intensity I . Both beams will generate an amount of free charge Q , regardless the extent of overlap. From this one might naively conclude that the V_{OC} does not depend on the extent of overlap. However, the degree of bimolecular recombination depends on the meeting of two charge carriers. The chance for recombination of free charge carriers induced by the intensity ΔI at a specific spot on the solar cell thus depends on whether this spot is also illuminated by the (background) intensity I . For the case of partial overlap of the laser beams, more free charges will thus survive compared to the case with full overlap. It was already suggested that the increase of S from (up to) 2 to 1 is induced by a take-over of the Langevin-type bimolecular recombination. A decrease of bimolecular recombination yields a larger value of S , i.e. the V_{OC} decreases less for increasing intensity. Hence, it is important to have good overlap of the beams. Perhaps a similar reasoning can be applied to inorganic solar cells, as it was experimentally verified that the V_{OC} decreases less for increasing intensity in the case of partial overlap (Chapter 5.6.2).

6.3 Suggestions for future research

6.3.1 Origin of $S < 1$

Several methods have shown that the slope of the V_{OC} as a function of the logarithm of intensity decreases for increasing intensity. For organic solar cells a decrease for S from large values (up to 2) to 1 might be attributed to the Langevin recombination taking over SRH-recombination or to an increasing occupancy of trap states for increasing intensity.^{[32],[33]} However, there must be another origin for the effect that S becomes even smaller than unity, an

effect that was obtained for silicon solar cells as well. The origin of these losses remains obscure. Perhaps the amount of generated free charges is not linear with intensity anymore for large intensities. One way to project non-linearity is assuming a power law. Let's assume for the generation rate G :

$$G \propto I^\gamma. \quad (6.1)$$

with γ some constant value smaller than unity. Substituting Eq. (6.1) into Koster's equation (2.25) yields

$$V_{OC} = C + \mathcal{W}_T \ln(I). \quad (6.2)$$

This illustrates that S , the slope in units of V_T of V_{OC} as a function of the natural logarithm of intensity, can become smaller than unity. Such effects are unwanted because of the detrimental effect on the power conversion efficiency. Investigating this effect should hence be the subject of future research. As a first step one could determine experimentally how the decrease of S levels off for even larger intensities than used in this thesis.

6.3.2 Alternative measuring methods

An interesting measurement would be to investigate the intensity dependence of the V_{OC} with a light source of another wavelength. If another laser is not available the use of a quartz tungsten halogen lamp might suffice as well, where the beam is monochromatized by means of a series of band-pass interference filters (Chapter 8.1). This measurement is particularly interesting because the absorption of the solar cells is wavelength dependent (Figure 49). It remains to be seen whether similar effects are obtained regarding the decrease of S . It is to be expected that this measurement also sheds light on the wavelength dependence of the occupation of traps. This experiment might as well explain the mismatch between the V_{OC} measurements of the laser and the Solar Simulator (Figure 41).

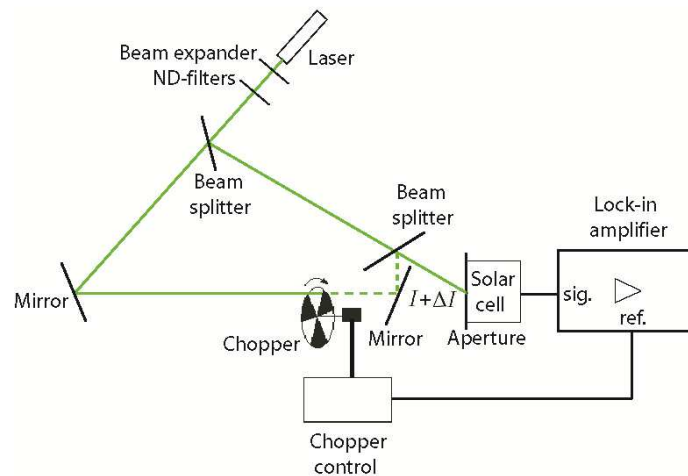


Figure 47: Modified experimental setup of the SSDV technique to achieve 100% beam overlap. An additional beam splitter and mirror are used with respect to Figure 34.

With the current SSDV setup 85% beam overlap could be achieved. Based on the measurements of Figure 44 it was assumed that this is comparable to conditions with 100% beam overlap. However, it is recommended to perform a similar experiment with organic solar cells. If one would prefer to achieve conditions with 100% overlap one should consider using an additional beam splitter and mirror according to Figure 47. The disadvantage of this setup is that the intensities I and ΔI both decrease due to the second beam splitter.

Furthermore, it would be worthwhile to perform also with an aperture the V_{OC} measurement as a function of intensity performed with the Solar Simulator as light source. This might improve the matching of the V_{OC} measurements of the laser and the Solar Simulator (Figure 41).

7 Conclusion

Six experimental methods have been used to study the light intensity dependence of the open-circuit voltage (V_{OC}). Measurements were performed on several organic bulk heterojunction solar cells. The donor materials used were P3HT, MEH and p-DTS(FBTTh₂)₂ (abbreviated as T1). As acceptor material PCBM was used. The type of hole transport layer (PEDOT:PSS) was varied to study the effect of leakage current experimentally.

To model the effect of leakage current, a modified p - n junction model has been used. The shunt resistance parameter R_{SH} was used to vary the size of the leakage current in the model. This model was also useful to determine whether open-circuit conditions are satisfied depending on the input impedance Z of a measuring device.

All methods consistently demonstrated for increasing intensity a decrease of S , i.e. the slope in units of V_T of V_{OC} plotted as a function of the natural logarithm of intensity. The main reason that S could be measured accurately is the use of a monochromatic laser instead of a spectrally broad lamp. The finding disproves the prevailing opinion in literature that the value of S is constant. Consequently, Method I is inappropriate as it assumes a constant value for S .

Method VI, the newly introduced steady-state differential voltage (SSDV) technique, seems to be the preferable method. The SSDV technique is based on measuring under open-circuit conditions the differential open-circuit voltage ΔV_{OC} induced by a laser beam with intensity ΔI superimposed on a laser beam with intensity I . This technique has the advantage that the measurement results for S show much less scatter than the methods that use the measurement of V_{OC} as a function of intensity for determination of S (Method II and III). However, a disadvantage of the SSDV technique is that the requirement to satisfy steady-state conditions gives a lower bound for the intensity. If one is interested to measure S for very low intensities one might prefer to determine ΔV_{OC} manually (Method V). Fitting a polynomial to the measurements of V_{OC} has proven to be a successful method for determination of S as well (Method IV).

For relatively low light intensities the value of S was found to be larger than unity for all organic solar cells which might be the fingerprint for trap states. The drop of S towards unity for high light intensities might be an indication of the Langevin-type bimolecular recombination becoming more manifest. With the laser light intensity increasing from 10 to 1000 W m⁻² the value of S was found to decrease from about 1.4 to 1.2 for the P3HT:PCBM solar cell. For the other solar cells it was determined that the value of S might even become smaller than unity for large intensities. For the MEH:PCBM and T1:PCBM solar cells the value of S was found to decrease from roughly 1.5 to 0.7 for the mentioned intensity regime. The physical origin of such low values of S remains unknown.

Remarkably, the effect of S becoming smaller than unity has been demonstrated for silicon solar cells as well, where S -values were obtained even as low as 0.45. When two beams are used, it was found that the light intensity dependence of the V_{OC} also depends on the extent of

beam overlap. For silicon solar cells it was demonstrated that the larger the extent of overlap, the smaller becomes S .

8 Appendices

8.1 External quantum efficiency

The external quantum efficiency (EQE) or incident photon to electron conversion efficiency ($IPCE$) is the amount of electrons extracted from a solar cell per incident photon. The test cell, which is placed in a portable airtight sample holder, is subjected to a background illumination (I) of approximately one sun, by means of two 50 W tungsten halogen lamps (Philips Brilliantline Pro). This background illumination (I) is superimposed by chopped monochromatic light (ΔI),¹² generated by a 50 W quartz tungsten halogen lamp (Newport Research Series). The light from this lamp is monochromatized by means of a series of band-pass interference filters (CVI laser) with wavelengths ranging from 400 to 980 nm.¹³ As the device is alternately illuminated with a light intensity I either $I+\Delta I$, a square wave with a wave height Δi_{sc} is produced; the differential current induced by the chopped light. Using the chopper in conjunction with a lock-in amplifier (Stanford Research Systems SR830), this response to the monochromatic light can be measured, while the contribution from the white background illumination is eliminated. As the solar cell has to operate under short-circuit conditions, a trans impedance amplifier is placed between the solar cell and the lock-in amplifier. Usually the trans impedance amplifier is set to a gain of 10 k Ω , which transforms the square wave with wave height Δi_{sc} to a square wave with (a 10^4 times larger) wave height ΔV . The lock-in amplifier multiplies the square wave signal by a pure sine wave at the chopper frequency.¹⁴ It has a low pass filter in it which gives the average output of this product. Because sine waves of different frequencies are orthogonal (i.e. the average of the product of two sine waves is zero unless the frequencies are exactly the same), the lock-in amplifier removes all signals with another frequency than the chopper frequency.¹⁵ It singles out the first harmonic ($k = 1$) which has an amplitude of $4/\pi$ times the amplitude of the square wave. The lock-in amplifier now gives the root mean square value (displayed as R) of the first harmonic. The original wave height ΔV is obtained from

$$\Delta V = 2 \cdot \sqrt{2} \cdot \frac{\pi}{4} \cdot R = \frac{\pi}{\sqrt{2}} R, \quad (8.1)$$

¹² To obtain a well-defined spot smaller than the area to be measured, a series of lenses is used. The sample holder is adjusted until the short-circuit current (measured with a Keithley 2410 SourceMeter) induced by only this light is maximized, to ensure that the full spot is located in the area.

¹³ Actually band-pass filters up to 1400 nm were available, but these were not used.

¹⁴ By using Fourier expansion an ideal square wave can be written as an infinite series of the form

$$x_{square}(t) = \frac{4}{\pi} \sum_{k=1}^{\infty} \frac{\sin((2k-1)\omega t)}{2k-1},$$

with $\omega = 2\pi f$, with f the cycle frequency over time t .

¹⁵ For that reason it is recommended not to use a multiple of 50 Hz, the frequency of the grid.

In order to determine the intensity of the monochromatic light, the light is first calibrated by means of a silicon photodiode (Newport 818-SL, Serial No: 15680).¹⁶ As the short-circuit current of the silicon photodiode is linearly dependent upon intensity, the calibration can be performed without back-ground illumination I .¹⁷ The current response in the silicon photodiode induced by the monochromatic light ΔI , is determined with the lock-in amplifier. From the tabulated spectral responsivity $S(\lambda)$ of the silicon photodiode (plotted in Figure 48), the intensity ΔI is determined for each band-pass filter.

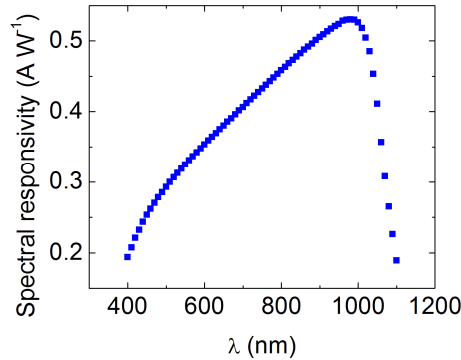


Figure 48: Spectral response curve of the silicon photodiode (Newport 818-SL, Serial No: 15680).

Afterwards measuring the current Δi_{SC} in the organic solar cell, induced by the same series of ΔI , yields the spectral responsivity of the organic solar cell. The EQE is related to the spectral responsivity according to

$$EQE(\lambda) = \frac{hc}{q\lambda} S(\lambda), \quad (8.2)$$

with h Planck's constant, C the speed of light and q the elementary charge. This results in the EQE -spectrum plotted in Figure 49.

From the EQE -measurement one can determine the J_{SC} under AM1.5G conditions from

$$J_{SC} = \frac{hc}{q} \int_{\lambda_1}^{\lambda_2} \frac{I_{AM1.5G}(\lambda) \cdot EQE(\lambda)}{\lambda} d\lambda, \quad (8.3)$$

with λ_1 and λ_2 the limits of the active spectrum of the solar cell, and $I_{AM1.5G}(\lambda)$ the intensity of the AM1.5G spectrum at the wavelength λ . According to Eq. (2.4) the efficiency is obtained from J_{SC} together with V_{OC} and FF . These performance characteristics are tabulated in Table 7.

¹⁶ In case of measuring with $\lambda > 980$ nm a Germanium (Oriel 71653) photodiode has to be used for calibration.

¹⁷ Moreover, it is recommended to omit the back-ground illumination in case of the silicon photodiode because it was found that in case of a large amount of irradiance the current was not linear with intensity.

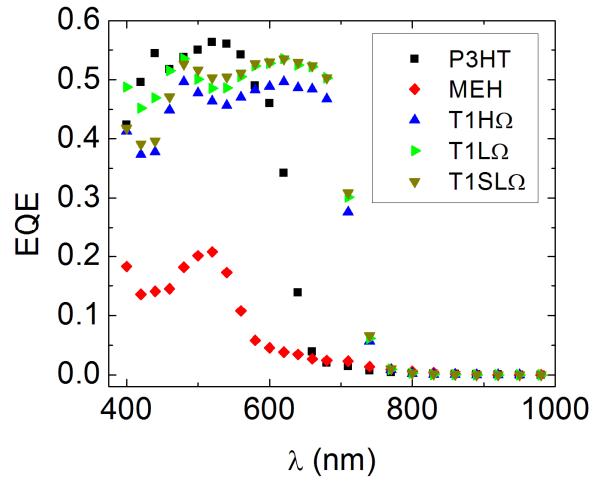


Figure 49: *EQE* as a function of wavelength for the five solar cells introduced in Chapter 4.

8.2 Intensity dependence of the short-circuit current

8.2.1 Introduction

In literature, one has often described the intensity dependence of the short-circuit current density (J_{sc}) as a power law relationship given by

$$J_{sc} \propto I^\alpha, \quad (8.4)$$

with α usually ranging between 0.85 and 1. Anyhow, it was found by Koster e.a. that α itself depends on intensity as well.^[9] Using the steady-state differential current (SSDC) technique, it was found that α can amount up to 17% for P3HT:PCBM devices annealed at 100 °C. These losses were analytically attributed to bimolecular recombination. Because such SSDC measurements were not yet performed at the University of Groningen, the aim was to realize the required experimental setup.

8.2.2 Measuring J_{sc} as a function of intensity

To measure the J_{sc} as a function of intensity, a laser (B&W TEK INC., Model BW1-532-50-E, Class IIIb) producing light with a wavelength of 532 nm and a maximum power of 80 mW is used in conjunction with a 5X Galilean Beam Expander (Thorlabs, BE05M-A), a beam splitter, two neutral density filter wheels and an aperture. The intensities are determined by means of measuring the induced short-circuit current in a silicon photodiode (Newport 818-SL). Measuring the short-circuit current with a Keithley 2410 SourceMeter for the P3HT, MEH and T1HΩ solar cells introduced in Chapter 4, yields the intensity dependence of J_{sc} as plotted in Figure 50.

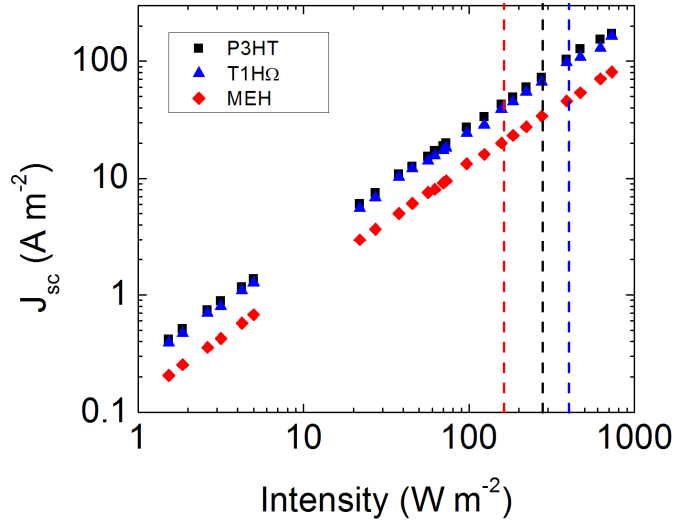


Figure 50: J_{sc} as a function of intensity on logarithmic scale. The vertical dashed lines correspond to light conditions that yield similar photocurrent as AM1.5G light (Table 8).

Fitting the power law of Eq. (8.5) to these measurements yields the α -values as tabulated in Table 11.

Table 11: The α -values obtained from applying the power law of Eq. (8.5) to the measurements of Figure 50.

Solar cell	α
P3HT	0.974
MEH	0.981
T1H Ω	1

8.2.3 Steady-state differential current technique

The SSDC technique is in many ways analogous to the *EQE* (Chapter 8.1) and the SSDV (Chapter 5.3) measuring techniques. This technique developed to study the light intensity dependence of the photocurrent is based on measuring under short-circuit conditions the differential current density ΔJ induced by a small modulation in light intensity (ΔI) in the presence of a background light intensity I . While Koster e.a. only used a laser for the background illumination and a monochromatic light source for the superimposed light,^[9] here a continuous wave laser (532 nm, 80 mW) will be used for both cases. The experimental setup is similar to the SSDV setup of Figure 34 with the addition of a continuous neutral density filter and a trans impedance amplifier. After passing a beam expander, the laser beam is split by a beam splitter from which the reflected beam (intensity I) is directly focused onto the solar cell, while the passing beam (intensity ΔI) is focused with a mirror and chopped beforehand. The two wheels with neutral density filters are used to modify the background light intensity I , while the

chopped light ΔI is kept constant during the measurements.¹⁸ However, a continuous neutral density filter was placed to attenuate ΔI to about 1 W m^{-2} . The light intensities are calibrated by means of measuring the short-circuit current with the silicon photodiode, using the same aperture. Again, the chopper is connected in conjunction with a lock-in amplifier with the trans impedance amplifier in between, set to a gain of $10 \text{ k}\Omega$. The lock-in amplifier measures the response Δi_{sc} induced by the light ΔI . By varying the background intensity I and dividing by the area of the aperture, the differential current density ΔJ is obtained as a function of intensity. The SSDC measurements are carried out with all intensities $I > \Delta I$. To ensure that the measured ΔJ corresponds to steady-state conditions, the chopper frequency was varied from 25 to 200 Hz. At all intensities the displayed value at the lock-in amplifier changed negligibly between these frequencies. During the experiments, the chopper wheel was set to 170 Hz. Applying the SSDC measurement to the MEH, P3HT and T1H Ω solar cells results in Figure 51(a). Normalizing these values to the plateau value at low intensity yields Figure 51(b). For α close to 1, these results should already be a good indication for α .

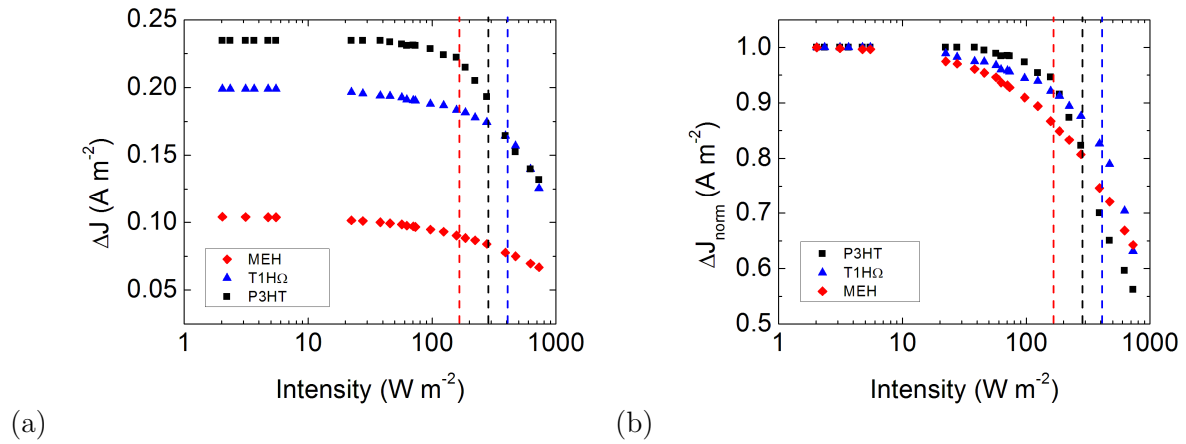


Figure 51: Results from applying the SSDC measurement to the MEH, P3HT and T1H Ω solar cells. The vertical dashed lines correspond to light conditions that yield similar photocurrent as AM1.5G light (Table 8). (a) The differential current density ΔJ as a function of intensity. (b) The result of normalizing the values of (a) to the plateau value at low intensity.

By taking the second derivative with respect to I from Eq. (8.4), and neglecting terms containing its derivatives, one obtains

$$\alpha = 1 + I \frac{d^2 J}{dI^2} \left(\frac{dJ}{dI} \right)^{-1}, \quad (8.5)$$

which results in Figure 52 when applying it to Figure 51(a) and assuming $dJ/dI = \Delta J/\Delta I$.

¹⁸ Initially the experiment was carried out without the continuous filter and the filter wheel in front of the beam splitter in order to have an as good as constant ratio $I/\Delta I$. But these results were found to be much less accurate, even if both I and ΔI were determined directly after each other.

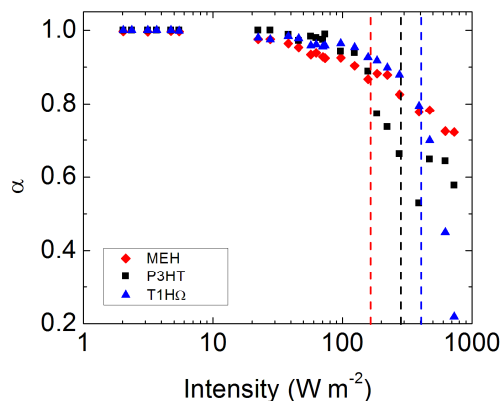


Figure 52: Results for α when applying Eq. (8.5) to Figure 51(a) and assuming $dJ/dI = \Delta J/\Delta I$. The vertical dashed lines correspond to light conditions that yield similar photocurrent as AM1.5G light (Table 8).

8.3 Manual for the Steady-State Differential Voltage (SSDV) technique

Usually the laser, beam expander, beam splitter and mirror do not have to be moved. Nevertheless it is recommended to align the set up every new day. The alignment of the laser beam is performed by first adjusting the silicon photodiode behind the aperture, and afterwards adjusting the beam splitter and mirror, while in both cases maximizing the short-circuit current (measured with a Keithley 2410 SourceMeter) induced by the beams ($I+\Delta I$). Be always sure that the aperture is not too far from the test cell as it is important that the light that is calibrated with the silicon photodiode completely “falls into” the area of the test cell. In order to avoid stray light, the sample holder and iris are covered with a box having a small opening.

Calibrate the intensities I and ΔI for each filter wheel position by measuring the i_{sc} with the silicon photodiode. The spectral responsivity of the diode at 532 nm is 0.314 A W^{-1} . By taking the area of the aperture under consideration this yields the intensity of the light in W m^{-2} . Measuring $i_{sc}(I)$ and $i_{sc}(I+\Delta I)$ directly after each other is important in order to keep the error in $\Delta I/I$ as small as possible. This measurement can be performed most easily by using a beam stop.

Place the sample holder with the test cell in it. Measure with the Keithley the short-circuit current induced by the light ($I+\Delta I$) and maximize it by adjusting the sample holder behind the aperture. This procedure should be performed again for every device to be measured. Now it is recommended to place a beam stop in front of ΔI . Use the Keithley to measure V_{oc} induced in the test cell by the intensity I for a series of filter wheel combinations,¹⁹ in order to determine the intensity regime that is not affected by leakage.

¹⁹ When measuring under open-circuit conditions, it is recommended to reduce the compliance of the Keithley 2410 SourceMeter to e.g. 2V, as it might otherwise destroy your sample (in case of a very low intensity of illumination).

Determine the criterion for measuring under open-circuit conditions, by modelling with an equivalent circuit. The value of R_{SH} is determined from the slope of the dark current at $V = 0$. For the value of the ideality factor n one might use the slope in the i - V curve of the diffusion regime under illumination or the slope S obtained from the $V_{oc}(I)$ measurement. The values of i_0 and R_s should be varied until the simulated i - V curve fits the best at V_{oc} . Determining the ratio “ S ”/ S as a function of i_{sc} gives a criterion for measuring under open-circuit conditions during the SSDV measurement.

Ensure again that the beam stop is placed to block the light with intensity ΔI . Use the Keithley to measure i_{sc} induced in the test cell by the intensity I for a series of filter wheel combinations. Dividing by the area of the aperture yields J_{sc} in $A\ m^{-2}$. The intensity of the laser where $J_{sc}(\text{laser}) = J_{sc}(EQE)$ can be used as an approximation for 1 Sun conditions. This measurement also determines the intensity that corresponds to the criterion in i_{sc} for measuring under open-circuit conditions.

The SSDV experiment is carried out with a chopper wheel in conjunction with a lock-in amplifier. Connect the chopper to the ‘Ref’ input of the lock-in amplifier. Place the chopper between the mirror and the test cell. Connect the test cell with the lock-in amplifier (input ‘A/I’). Set the orange box to the required area of the test cell, and set it to “current ground”, and “test cell”. Set the lock-in amplifier to “ R ” to display the root mean square value of the first harmonic of the wave height ΔV_{oc} , which is related to R according to

$$\Delta V_{oc} = \frac{\pi}{\sqrt{2}} R. \quad (8.6)$$

Vary the chopper frequency from e.g. 20 to 200 Hz and verify whether the displayed value R does not change more than e.g. 5%, in order to ensure steady-state conditions. Do this at every filter wheel combination and determine the lowest allowed intensity. Put it for every measurement at the same (low) frequency, e.g. 30 Hz. Too low frequencies (< 10 Hz) were found to be inaccurate. Also multiples of 50 Hz must be avoided because of the grid frequency. In order to prevent the lock-in amplifier from getting overloaded (OLD), it might be required to adjust the sensitivity.

Now the slope S can be measured as a function of intensity, according to Eq. (3.8). S should always be plotted as a function of $I + \Delta I/2$.

8.4 Variation of ratio $\Delta I/I$

Figure 53 shows the results of the modified p - n junction model as performed with several values of $\Delta I/I$, with S plotted as a function of I (a) and as a function of $I + \Delta I/2$ (b). The results overlap better in the latter case from which it is concluded that one should always plot S as a function of $I + \Delta I/2$.

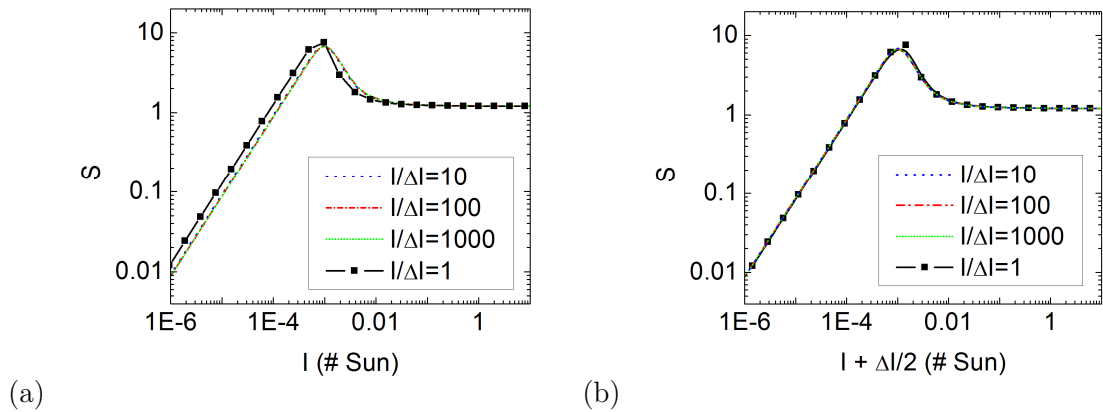


Figure 53: Results for the modified p - n junction model with S plotted as a function of I (a) and as a function of $I + \Delta I/2$ (b).

8.5 Extent of overlap of laser beams behind the aperture

When a line cuts a circle a chord c is formed. The two lines from the center of the circle to the ends of the chord have length R , the radius of the circle. The area within these three lines forms a triangle with area A_B , shaded in blue in Figure 54. The angle opposite to the chord is the central angle θ . The perpendicular distance from the central angle to the chord is denoted as $d_{1/2}$. The area between the triangle and the shortest arc is called the segment, which is shaded in yellow having area A_Y and height h . The triangle (blue) and the segment (yellow) form together the minor circular sector with area A_{B+Y} and arc length s .

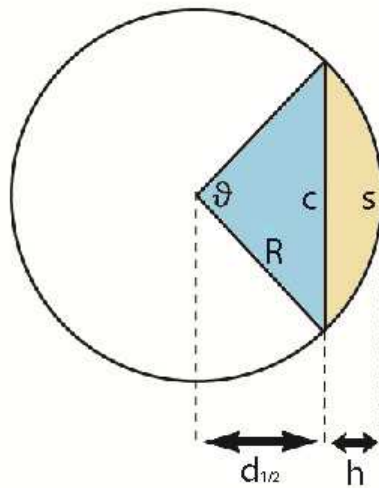


Figure 54: A chord with length c cutting a circle with radius R creates a segment (yellow) having area A_Y , arc length s , and height h . The triangular area (blue) with area A_B has as its central angle θ and height $d_{1/2}$. Together, these two areas form the minor circular sector with area A_{B+Y} .

With these definitions the radius R satisfies

$$R = h + d_{1/2}. \quad (8.7)$$

The arc length s is

$$s = R\theta. \quad (8.8)$$

The height $d_{1/2}$ can be calculated from

$$d_{1/2} = R \cos\left(\frac{1}{2}\theta\right). \quad (8.9)$$

Rewriting Eq. (8.9) yields

$$\theta = 2 \cos^{-1}\left(\frac{d_{1/2}}{R}\right). \quad (8.10)$$

The chord length c can be expressed as

$$c = 2R \sin\left(\frac{1}{2}\theta\right). \quad (8.11)$$

The area of the minor circular sector is obtained from multiplying the total area of the circle with the ratio of the arc s (Eq. (8.8)) to the circle's perimeter, i.e.

$$A_{B+Y} = \frac{s}{2\pi R} \pi R^2 = \frac{1}{2} R s = \frac{1}{2} R^2 \theta. \quad (8.12)$$

The triangular (blue) area A_B is

$$A_B = \frac{1}{2} c d_{1/2} = \frac{1}{2} R^2 \sin(\theta), \quad (8.13)$$

as obtained from Eq. (8.9), Eq. (8.11), and the trigonometric identity

$$\sin(\alpha) \cos(\alpha) = \frac{1}{2} \sin(2\alpha). \quad (8.14)$$

The area of the (yellow) segment A_Y is obtained from subtracting the area of the triangle A_B from the area of the sector A_{B+Y} according to

$$A_Y = A_{B+Y} - A_B = \frac{1}{2} R^2 (\theta - \sin(\theta)). \quad (8.15)$$

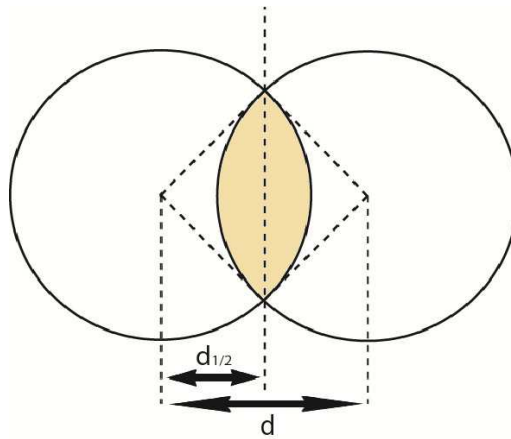


Figure 55: The overlapping area of two beams equals the two circle segments shaded in yellow. The area of a single segment is defined by Eq. (8.15).

Consider now two laser beams passing a circular aperture with radius R as is the case for the SSDV (Chapter 5.3) and SSDC (Chapter 8.2.3) techniques. Once they arrive at the solar cell their centers are separated a distance d , as illustrated in Figure 55, where

$$d = 2 \cdot d_{1/2}. \quad (8.16)$$

The overlapping area of the beams is built up from the two circular segments shaded in yellow, which yields from Eq. (8.15)

$$A_{\text{overlap}} = R^2(\theta - \sin(\theta)). \quad (8.17)$$

Consequently, the fraction of beam overlap is determined from

$$\frac{A_{\text{overlap}}}{\pi R^2} = \frac{1}{\pi}(\theta - \sin(\theta)), \quad (8.18)$$

with θ defined in Eq. (8.10). For $d = 0$, one obtains $\theta = \pi$, which corresponds to a fraction of beam overlap of 1, as obtained from Eq. (8.18). For $d = 2 \cdot R$, one obtains $\theta = 0$, corresponding to a fraction of beam overlap of 0. This means that the overlap is zero when the two beams are separated a distance more than their diameter.

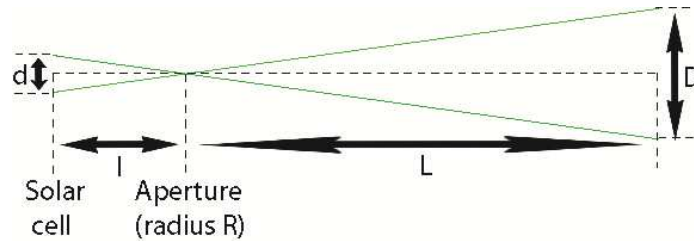


Figure 56: Two laser beams (green) are separated a distance D at a distance L from the aperture having radius R . At the solar cell, which is located a distance l from the aperture, they are separated a distance d according to Eq. (8.19).

From Figure 56 one can easily see that the distance d between the centers of two laser beams when arriving at the solar cell is related to the distances l , L and D according to

$$d = \frac{l}{L} D. \quad (8.19)$$

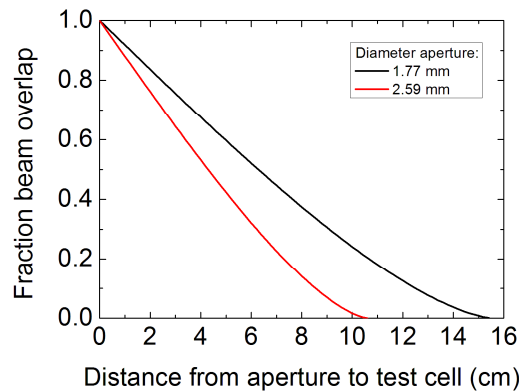


Figure 57: The fraction of beam overlap as a function of the distance from the aperture to the test cell as obtained from Eq. (8.18) using $D = 3$ cm, $L = 1.8$ m and for the diameter of the aperture ($2 \cdot R$) 1.77 mm (black) and 2.59 mm (red).

Plotting the fraction beam overlap from Eq. (8.18) as a function of l , i.e. the distance from the aperture to the test cell, one obtains Figure 57. For the input parameters the experimental values are used: $D = 3$ cm, $L = 1.8$ m, and for the diameter of the aperture ($2 \cdot R$) 1.77 mm (as used in Chapter 5.1-5.3) and 2.59 mm (as used in Chapter 5.5) respectively.

8.6 Temperature measurements

A thermo couple (Kane-May KM330) has been used to perform a series of measurements shown in Figure 58. The measurement referred to as ‘No solar cell’ has been performed by directly illuminating the thermo couple with a laser. The measurement referred to as ‘Active layer + Aluminium’ has been performed by putting the thermo couple directly to the aluminium electrode of the P3HT:PCBM solar cell introduced in Chapter 4.1.1, while illuminating the active layer. Instead, when the thermo couple was placed directly on the active layer while illuminating there, even larger temperature values are obtained, as shown by the measurement referred to as ‘Active layer’. From these measurements one concludes that the temperature of the solar cells might increase up to about 3 °C.

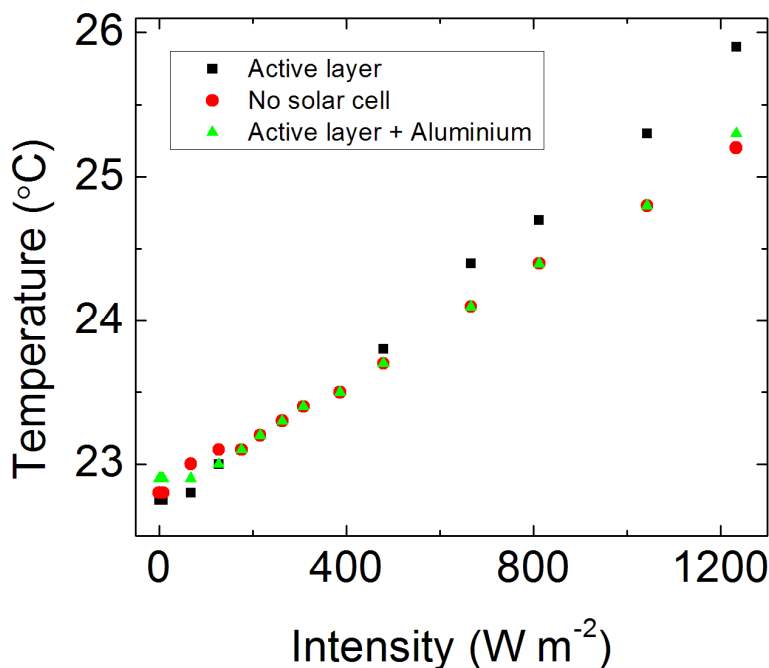


Figure 58: Temperature measurement with the P3HT:PCBM solar cell introduced in Chapter 4.1.1.

8.7 The p - n junction based model in Matlab

8.7.1 Modified p - n junction based model

```
function [I] = nest(Rp, Rs, I0, Iph, Vt, n, V, x0)
[I] = fzero(@nestedfun, x0);
function y = nestedfun(x)
y = (-x - Iph + I0 * (exp((V - x * Rs) / (n * Vt)) - 1) + (V - x * Rs) / Rp);
```

```

end
end

function [] = IVcurve
% Shunt resistance:
Rp=250000;
% Series resistance:
Rs=42;
% Reverse bias saturation current:
I0=3.82E-12;
% Short-circuit current @ 1 Sun
Iph=8.94E-04;
% Thermal voltage:
Vt=0.0254;
% Ideality factor:
n=1.21;

h=0.001;
Vend=1;
Voltage=0:h:Vend;
Current=Voltage*0;
number=1+Vend/h;
x0=0;
for i=1:size(Voltage,2)
    V=Voltage(i);
    [I] = nest(Rp,Rs,I0,Iph,Vt,n,V,x0);
    Current(i)=I;
end
table(1:number,1) = Voltage';
table(1:number,2) = Current';
plot (Voltage,Current)
save('C:\Name','table','-ascii')
end

```

8.7.2 The model as a criterion test for open circuit conditions

```

function [I] = nest(Rp,Rs,I0,Iph,Vt,n,V,x0)
[I] = fzero(@nestedfun,x0);
function y = nestedfun(x)
    y = (-x-Iph+I0*(exp((V-x*Rs)/(n*Vt))-1)+(V-x*Rs)/Rp);
end
end

```

```

function [] = SSDV()
tic
format long

Rp=250000;
Rs=42;
I0=3.82E-12;
Iph=8.94E-04;
n=1.21;

Vt=0.0254;
Imp=10E6;
Iphj1=(2^4)*Iph;
ratio=1;
deltaIphj1=Iphj1/ratio;

```

```

amount=25;
start=1;

% Tabulation in advance strongly speeds up the model.
j_ = ones(amount,1);
sun = ones(amount,1);
sun_IplushalfdI = ones(amount,1);
I_ph = ones(amount,1);
deltaI_ph = ones(amount,1);
Voc = ones(amount,1);
Voc_IplusdI = ones(amount,1);
deltaVoc = ones(amount,1);
s = ones(amount,1);
lockinVoc = ones(amount,1);
errorVoc = ones(amount,1);
fractionVoc = ones(amount,1);
lockinVoc_IplusdI = ones(amount,1);
errorVoc_IplusdI = ones(amount,1);
fractionVoc_IplusdI = ones(amount,1);
lockindeltaVoc = ones(amount,1);
errordeltaVoc = ones(amount,1);
fractiondeltaVoc = ones(amount,1);
lockin_s = ones(amount,1);
ratio_s = ones(amount,1);

for j=start:start+amount-1
    j_(j)=j;
    sun(j)=2^(5-j);
    sun_IplushalfdI(j)=sun(j)+0.5*sun(j)/ratio;
    x0=0;
    Iph=(1/(2^(j-1)))*Iphj1;
    I_ph(j)=Iph;
    deltaIph =(1/(2^(j-1)))*deltaIphj1;
    deltaI_ph(j)=deltaIph;
    Isum = Iph + deltaIph;
if j==start
    Vb = 1;
    Va = 0;
else
    Vb = Voc(j-1);
    Va = 0;
end
    for i=1:10000
        V = (Vb + Va)/2;
        [I] = nest(Rp,Rs,I0,Iph,Vt,n,V,x0);
        if I < 0
            Va = V;
        else
            Vb = V;
        end
        if I > -1E-15 && I < 0
            Voc(j)=V;
            break
        end
        x0=I;
    end
end
% Now we know the exact Voc(I) until j-th curve
if j==start
    Vb = 1;
    Va = 0;
else

```

```

    Vb = Voc_IplusdI(j-1);
    Va = 0;
end
for i=1:10000
    V = (Vb + Va)/2;
    [I] = nest(Rp,Rs,I0,Isum,Vt,n,V,x0);
    if I < 0
        Va = V;
    else
        Vb = V;
    end
    if I > -1E-15 && I < 0
        Voc_IplusdI(j)=V;
        deltaVoc(j)=Voc_IplusdI(j)-Voc(j);
% Now we know the exact Voc(I+dI) and "deltaVoc = Voc(I+dI)-Voc(I)" until
% j-th curve. From this we calculate the exact S:
        s(j)=(deltaVoc(j)/Vt)*(1/log(1+(deltaI_ph(j)/I_ph(j))));
        break
    end
    x0=I;
end
Vb = Voc(j);
Va = 0;
for i=1:10000
    V = (Vb + Va)/2;
    [I] = nest(Rp,Rs,I0,Iph,Vt,n,V,x0);
    if V/(-I) < Imp && I < 0
        Va = V;
    else
        Vb = V;
    end
    if V/(-I) < Imp && V/(-I) > (Imp-(Imp/100000))
        lockinVoc(j)=V;
% Now we know Voc(I) due to the lock-in until j-th curve
        errorVoc(j)=Voc(j)-V;
        fractionVoc(j)=errorVoc(j)/Voc(j);
        break
    end
    x0=I;
end
Vb = Voc_IplusdI(j);
Va = 0;
for i=1:10000
    V = (Vb + Va)/2;
    [I] = nest(Rp,Rs,I0,Isum,Vt,n,V,x0);
    if V/(-I) < Imp && I < 0
        Va = V;
    else
        Vb = V;
    end
    if V/(-I) < Imp && V/(-I) > (Imp-(Imp/100000))
        lockinVoc_IplusdI(j)=V;
% Now we know Voc(I+dI) due to the lock-in until j-th curve
        errorVoc_IplusdI(j)=Voc_IplusdI(j)-V;
        fractionVoc_IplusdI(j)=errorVoc_IplusdI(j)/Voc_IplusdI(j);
        lockindeltaVoc(j)=lockinVoc_IplusdI(j)-lockinVoc(j);
% Now we know the approximation of deltaVoc of the lock-in until j-th
% curve. The induced error is:
        errordeltaVoc(j)= deltaVoc(j) - lockindeltaVoc(j);
        fractiondeltaVoc(j) = errordeltaVoc(j)/deltaVoc(j);
% The approximation of S due to the lock-in is:

```

```

    lockin_s(j) = (lockindeltaVoc(j)/Vt)*(1/log(1+(deltaI_ph(j)/I_ph(j))));
% The ratio between this "s" and the exact S is:
    ratio_s(j) = (lockin_s(j))/(s(j));
    break
end
    x0=I;
end
end
table(1:amount,1) = j_';
table(1:amount,2) = sun';
table(1:amount,3) = sun_IplushalfdI';
table(1:amount,4) = I_ph';
table(1:amount,5) = deltaI_ph';
table(1:amount,6) = Voc';
table(1:amount,7) = Voc_IplusdI';
table(1:amount,8) = deltaVoc';
table(1:amount,9) = s';
table(1:amount,10) = lockinVoc';
table(1:amount,11) = errorVoc';
table(1:amount,12) = fractionVoc';
table(1:amount,13) = lockinVoc_IplusdI';
table(1:amount,14) = errorVoc_IplusdI';
table(1:amount,15) = fractionVoc_IplusdI';
table(1:amount,16) = lockindeltaVoc';
table(1:amount,17) = errordeltaVoc';
table(1:amount,18) = fractiondeltaVoc';
table(1:amount,19) = lockin_s';
table(1:amount,20) = ratio_s';

save('C:\Name','table','-ascii')
toc
end

```

References

- [1] “Third assessment report - climate changes,” (*IPCC*), *Intergovernmental Panel on Climate Changes 2001*, Web site: www.meto.gov.uk.
- [2] “Global environment outlook,” *United Nations Environment Programme (UNEP)*, *GEO year book 2004/5*, Web site: www.unep.org/geo/yearbook.
- [3] “International Energy Outlook 2009,” *U.S. Energy Information Administration*, Web site: www.eia.doe.gov/oiaf/ieo/index.html.
- [4] P. R. P. J. Chow, R. J. Knopp, “Energy Resources and Global Development,” *Science*, vol. 302, p. 1528, 2003.
- [5] T. J. K. Knapp, “Empirical Investigation of the Energy Payback Time for Photovoltaic Modules,” *Solar Energy*, vol. 71, no. 3, pp. 165–172, 2001.
- [6] W. W. M. A. Green, K. Emery, Y. Hishikawa, “Solar Cell Efficiency Tables,” *Prog. Photovolt: Res. Appl.*, vol. 19, pp. 84–92, 2011.
- [7] G. E. J. S. E. Shaheen, R. Radspinner, N. Peyghambarian, “Fabrication of bulk heterojunction plastic solar cells by screen printing,” *Applied Physics Letters*, vol. 79, p. 2996, 2001.
- [8] A. J. H. G. Gustafsson, Y. Cao, G. M. Treacy, F. Klavetter, N. Colaneri, “Flexible light-emitting diodes made from soluble conducting polymers,” *Nature*, vol. 357, p. 477, 1992.
- [9] L. J. A. Koster, M. Kemerink, M. M. Wienk, K. Maturová, and R. A. J. Janssen, “Quantifying bimolecular recombination losses in organic bulk heterojunction solar cells,” *Advanced materials (Deerfield Beach, Fla.)*, vol. 23, no. 14, pp. 1670–4, Apr. 2011.
- [10] W. Shockley and H. J. Queisser, “Detailed Balance Limit of Efficiency of p-n Junction Solar Cells,” *Journal of Applied Physics*, vol. 32, no. 3, p. 510, 1961.
- [11] B. Gregg and M. Hannai, “Comparing Organic to Inorganic Photovoltaic Cells: Theory, Experiment, and Simulation,” *J. Appl. Phys.*, vol. 93, no. 6, p. 3606, 2003.
- [12] L. J. A. Koster, E. Smits, V. Mihailetschi, and P. Blom, “Device model for the operation of polymer/fullerene bulk heterojunction solar cells,” *Physical Review B*, vol. 72, no. 8, p. 085205, Aug. 2005.

References

- [13] L. J. A. Koster, S. E. Shaheen, and J. C. Hummelen, "Pathways to a New Efficiency Regime for Organic Solar Cells," *Advanced Energy Materials*, vol. 2, no. 10, pp. 1246–1253, Oct. 2012.
- [14] M. Gruber, J. Wagner, K. Klein, U. Hörmann, A. Opitz, M. Stutzmann, and W. Brütting, "Thermodynamic Efficiency Limit of Molecular Donor-Acceptor Solar Cells and its Application to Diindenoperylene/C60-Based Planar Heterojunction Devices," *Advanced Energy Materials*, vol. 2, no. 9, pp. 1100–1108, Sep. 2012.
- [15] K. Vandewal, K. Tvingstedt, A. Gadisa, O. Inganäs, and J. V Manca, "On the origin of the open-circuit voltage of polymer-fullerene solar cells.," *Nature materials*, vol. 8, no. 11, pp. 904–9, Nov. 2009.
- [16] N. C. Giebink, G. P. Wiederrecht, M. R. Wasielewski, and S. R. Forrest, "Thermodynamic efficiency limit of excitonic solar cells," *Physical Review B*, vol. 83, no. 19, p. 195326, May 2011.
- [17] L. Onsager, "Initial Recombination of Ions," *Phys. Rev.*, vol. 54, p. 554, 1938.
- [18] L. Onsager, "Deviations from Ohm's Law in Weak Electrolytes," *J. Phys. Chem.*, vol. 2, p. 599, 1934.
- [19] C. L. Braun, "Electric field assisted dissociation of charge transfer states as a mechanism of photocarrier production," *J. Chem. Phys.*, vol. 80, p. 4157, 1984.
- [20] V. Choong, Y. Park, Y. Gao, T. Wehrmeister, K. Müllen, B. R. Hsieh, and C. W. Tang, "Dramatic photoluminescence quenching of phenylene vinylene oligomer thin films upon submonolayer Ca deposition," *Applied Physics Letters*, vol. 69, no. 10, p. 1492, 1996.
- [21] D. E. Markov and P. W. M. Blom, "Exciton quenching in poly(phenylene vinylene) polymer light-emitting diodes," *Applied Physics Letters*, vol. 87, no. 2003, p. 233511, 2005.
- [22] P. Langevin, "Recombinaison et mobilités des ions dans les gaz," *Ann. Chim. Phys.*, vol. 28, pp. 433–530, 1903.
- [23] G. J. Adriaenssens and V. I. Arkhipov, "Non-Langevin recombination in disordered materials with random potential distributions," vol. 103, no. 9, pp. 541–543, 1997.
- [24] L. J. A. Koster, V. D. Mihailetschi, and P. W. M. Blom, "Bimolecular recombination in polymer/fullerene bulk heterojunction solar cells," *Applied Physics Letters*, vol. 88, no. 5, p. 052104, 2006.
- [25] G. Juška, K. Genevičius, N. Nekrašas, G. Sliaužys, and R. Österbacka, "Two dimensional Langevin recombination in regioregular poly(3-hexylthiophene)," *Applied Physics Letters*, vol. 95, no. 1, p. 013303, 2009.

References

- [26] D. P. McMahon, D. L. Cheung, and A. Troisi, “Why Holes and Electrons Separate So Well in Polymer / Fullerene,” pp. 2737–2741, 2011.
- [27] T. Kirchartz, B. E. Pieters, J. Kirkpatrick, U. Rau, and J. Nelson, “Recombination via tail states in polythiophene:fullerene solar cells,” *Physical Review B*, vol. 83, no. 11, p. 115209, Mar. 2011.
- [28] A. Maurano, R. Hamilton, C. G. Shuttle, A. M. Ballantyne, J. Nelson, B. O’Regan, W. Zhang, I. McCulloch, H. Azimi, M. Morana, C. J. Brabec, and J. R. Durrant, “Recombination dynamics as a key determinant of open circuit voltage in organic bulk heterojunction solar cells: a comparison of four different donor polymers,” *Advanced materials (Deerfield Beach, Fla.)*, vol. 22, no. 44, pp. 4987–92, Nov. 2010.
- [29] W. Shockley and W. T. Read, “Statistics of the Recombinations of Holes and Electrons,” *Phys. Rev.*, vol. 87, pp. 835–842, 1952.
- [30] R. N. Hall, “Electron-Hole Recombination in Germanium,” *Phys. Rev.*, vol. 87, p. 387, 1952.
- [31] L. J. A. Koster, V. D. Mihailetschi, R. Ramaker, and P. W. M. Blom, “Light intensity dependence of open-circuit voltage of polymer:fullerene solar cells,” *Applied Physics Letters*, vol. 86, no. 12, p. 123509, 2005.
- [32] G. A. H. Wetzelaer, M. Kuik, and P. W. M. Blom, “Identifying the Nature of Charge Recombination in Organic Solar Cells from Charge-Transfer State Electroluminescence,” *Advanced Energy Materials*, vol. 2, no. 10, pp. 1232–1237, Oct. 2012.
- [33] M. M. Mandoc, F. B. Kooistra, J. C. Hummelen, B. de Boer, and P. W. M. Blom, “Effect of traps on the performance of bulk heterojunction organic solar cells,” *Applied Physics Letters*, vol. 91, no. 26, p. 263505, 2007.
- [34] M. Kuik, L. J. a. Koster, G. a. H. Wetzelaer, and P. W. M. Blom, “Trap-Assisted Recombination in Disordered Organic Semiconductors,” *Physical Review Letters*, vol. 107, no. 25, p. 256805, Dec. 2011.
- [35] W. S. C. T. Sah, R. N. Noyce, “Carrier generation and recombination in p-n junctions and p-n junction characteristics,” *Proc. IRE*, vol. 45, pp. 1228–1243, 1957.
- [36] T. Dekorsy, T. Pfeifer, W. Kütt, and H. Kurz, “Subpicosecond carrier transport in GaAs surface-space-charge fields,” *Physical review. B, Condensed matter*, vol. 47, no. 7, pp. 3842–3849, Feb. 1993.
- [37] S. M. Sze and K. N. Kwok, *Physics of Semiconductor Devices*. 2007, p. 64.
- [38] C. J. Neef and J. P. Ferraris, “MEH-PPV: Improved Synthetic Procedure and Molecular Weight Control,” *Macromolecules*, vol. 33, no. 7, pp. 2311–2314, Apr. 2000.

References

- [39] T. S. van der Poll, J. A. Love, T.-Q. Nguyen, and G. C. Bazan, “Non-basic high-performance molecules for solution-processed organic solar cells,” *Advanced materials (Deerfield Beach, Fla.)*, vol. 24, no. 27, pp. 3646–9, Jul. 2012.